UC San Diego
UC San Diego Electronic Theses and Dissertations

Title
Novel Optical Signal Amplification Mechanisms in Semiconductor Photodetectors

Permalink
https://escholarship.org/uc/item/57s9f7vm

Author
Yu, Yugang

Publication Date
2020

Peer reviewed|Thesis/dissertation

UNIVERSITY OF CALIFORNIA SAN DIEGO

Novel Optical Signal Amplification Mechanisms in Semiconductor Photodetectors

A dissertation submitted in partial satisfaction of the requirements for the degree Doctor of Philosophy

in

Material Science and Engineering

by

Yugang Yu

Committee in charge:

Professor Yu-Hwa Lo, Chair
Professor Shadi Dayeh
Professor Andrew Kummel
Professor Tina Ng
Professor Sheng Xu

2020

SIGNATURE PAGE

The Dissertation of Yugang Yu is approved, and it is

acceptable in quality and form for publication on microfilm

and electronically:

_____

_____

_____

_____

_____

Chair

University of California San Diego

2020

DEDICATION

To Shangkun Yu and Xiaowen Dong

TABLE OF CONTENTS

LIST OF FIGURES

ACKNOWLEDGMENTS

First and foremost, I would like to express my great gratitude to my advisor, Professor Yu-Hwa Lo, for his guidance through my entire Ph.D. career. He is not only a researcher with tremendous knowledge and vast experience, but also an educator full of patience and enthusiasm. He would love to always provide useful suggestions and insightful comments to the problems that I encountered during my Ph.D. studies at UCSD, from which I have learnt a lot on both technical aspects and how to analyze and solve problems. Owing to his thorough training and thoughtful support, I have become an independent research with active problem-solving skill. He has been a role model in many aspects.

I would also like to thank my dissertation committee members, Prof. Shadi Dayeh, Prof. Andrew Kummel, Prof. Tina Ng and Prof. Sheng Xu, for their time, interest and continuous supports on my research. They provided me with many valuable suggestions on my projects and collaborated with me on some of my experiments that I will show in the dissertation. Besides my committee, I also need to thank Prof. Zhaowei Liu and Prof. Kenji Nomura for their selfless help and suggestions on some of my projects. I also want to thank Prof. William McEneaney from MAE department and Prof. Avi Yagil from Physics department for giving me the chances and experience working as their teaching assistant.

Moreover, I really appreciate the technical help and support on device fabrication from Nano3 cleanroom staff under San Diego Nanotechnology Infrastructure (SDNI), Dr. Bernd Fruhberger, Dr. Xuekun Lu, Larry Grimsson, Sean Parks, Shu Xiang and Patrick Driscoll.

Next, I want to thank the group members who have graduated. First, I thank Dr. Yu-Hsin Liu, Dr. David Hall and Dr. Lujiang Yan, who were my mentors when I first came to the group.

They taught me and trained me thoroughly on both device fabrication and characterization skills which I have been utilizing during my whole Ph.D. research. I thank Dr. Iftikhar Niaz, who worked on the theoretical calculation and simulation, and helped me a lot on some theoretical problems that I met. I also thank my labmate, Dr. Zihan Xu. We worked on many projects together and had two co-first author publications.

I would like to thank my "Mighty" colleagues in Lo Group: Jiayun Zhou, Mohammad Abu Raihan Miah, Alex Ce Zhang, Shaurya Arya, Samir Damle, Shih-Yun Chiu, Zijian Zeng and Yong Zhang from Photonics group. We worked together and had so many unforgettable memories. We supported and cheered up each other when we encountered difficulties and bottlenecks during our researches. We chatted with each other not only on the research but also our daily trivia. And we hanged out for dinner on some of the Friday nights. There are additional "Mighties" in Biomedical group that I would like to acknowledge here for their support and friendship: Dr. Roger Chiu, Dr. Tony Yen, Dr. Tiantian Zhang, Dr. Wei Cai, Dr. Yi Gu, Dr. Yuanyuan Han, Dr. Ping-wei Chen, Chi-Yang Tseng, Yi-Huan Tsai, Rui Tang, Zunming Zhang, Edward Wang, Xinyu Chen and Zhilin Guo.

In addition, I want to thank my friends in the United States and China for their constant friendship and support. When I first came to the US, my friends Shuai Zhang and Haowen Ren have become my roommates until now. We are all from Materials Science and Engineering program and support each other all the time. For my best friend in the high school, Ao Guo, who is now working at Microsoft, we frequently chat with each other and travel together. Also I appreciate my childhood best friends, Yuhao Zuo, Ying Su and Shijia Mao, for their frequent caring messages and being with me in spirit.

Finally, I would like to express my deepest gratitude to my parents, Shangkun Yu and Xiaowen Dong, who have been always there full of support, encouragement and love during my whole life. They are very open-minded parents and respect all the choices I have made even some of them were considered not good. Every time when I encountered difficulties and felt frustrated or discouraged, they would always provide me with strong mental support and cheer me up. I am so proud of being their son.

The material in this dissertation is based on the following publications.

Portion of Chapter 2 has been published in the following publication: Yan, L., **Yu, Y.**, Zhang, A.C., Hall, D., Niaz, I.A., Raihan Miah, M.A., Liu, Y.H. and Lo, Y.H., 2017. An Amorphous Silicon Photodiode with 2 THz Gain-bandwidth Product based on Cycling Excitation Process. Applied Physics Letters, 111(10), p.101104. The dissertation author is the primary investigator/secondary author of the paper.

Portion of Chapter 3 is unpublished work focusing on dark current reduction methods for amorphous silicon CEP detectors, with the efforts provided by **Yu, Y.**, Zhou, J., Raihan Miah, M.A., Chiu, S.Y., Nomura, K., and Lo, Y.H. The dissertation author is the primary investigator of the project.

Portion of Chapter 4 has been published in the following publication: **Yu, Y.**, Xu, Z., Li, S., Zhang, A.C., Yan, L., Liu, Z. and Lo, Y.H., 2019. Plasmonically Enhanced Amorphous Silicon Photodetector with Internal Gain. IEEE Photonics Technology Letters, 31(12), pp.959-962. The dissertation author is the primary investigator/first author of the paper.

Portion of Chapter 5 has been published in the following publication: Xu, Z. †, **Yu, Y.** †, Arya, S., Niaz, I.A., Chen, Y., Lei, Y., Miah, M.A.R., Zhou, J., Zhang, A.C., Yan, L., Xu, S., and Lo, Y.H. 2020. Frequency-and Power-Dependent Photoresponse of a Perovskite Photodetector

Down to the Single-Photon Level. Nano Letters, 20(3), pp.2144-2151 († These authors contributed equally). The dissertation author is the primary investigator/co-first author of the paper.

Yugang Yu

La Jolla, California

June 2020

VITA

EDUCATION

2010 – 2014   B.S. Materials Science and Engineering, Wuhan University, China

2014 – 2015   M.S. Materials Science and Engineering, University of California
                   San Diego, USA

2015 – 2020   Ph. D. Materials Science and Engineering Program, University
                   of California San Diego, USA

PUBLICATIONS

Xu, Z.*, **Yu, Y.***, Arya, S., Niaz, I. A., Chen, Y., & Lo, Y. H. (2020). Frequency and Power Dependent Photoresponse of Perovskite Photodetector Down to Single Photon Level. Nano Letters. (Co-first)

Chen, Y., Lei, Y., Li, Y., **Yu, Y.**, Cai, J., Chiu, M. H., ... & Hu, H. (2020). Strain engineering and epitaxial stabilization of halide perovskites. Nature, 577(7789), 209-215.

Zhou, J., Miah, M. A. R., **Yu, Y.**, Zhang, A. C., Zeng, Z., Damle, S., ... & Lo, Y. H. (2019). Room-temperature long-wave infrared detector with thin double layers of amorphous germanium and amorphous silicon. Optics Express, 27(25), 37056-37064.

Niaz, I. A., Miah, M. A. R., Yan, L., **Yu, Y.**, He, Z. Y., Zhang, Y., ... & Lo, Y. H. (2019). Modeling Gain Mechanisms in Amorphous Silicon Due to Efficient Carrier Multiplication and Trap-Induced Junction Modulation. Journal of Lightwave Technology, 37(19), 5056-5066.

Yu, Y., Xu, Z., Li, S., Zhang, A. C., Yan, L., Liu, Z., & Lo, Y. H. (2019). Plasmonically Enhanced Amorphous Silicon Photodetector with Internal Gain. IEEE Photonics Technology Letters, 31(12), 959-962.

Yan, L., **Yu, Y.**, Xu, Z., Niaz, I., Miah, M. A. R., Zhang, A. C., ... & Lo, Y. (2018, June). Low Noise, High Gain-Bandwidth Photodetectors Using Cycling Exciting Process (CEP) as Amplification Mechanism. In 2018 IEEE International Conference on Electron Devices and Solid State Circuits (EDSSC) (pp. 1-2). IEEE.

Yan, L., **Yu, Y.**, Zhang, A. C., Hall, D., Niaz, I. A., Raihan Miah, M. A., ... & Lo, Y. H. (2017). An amorphous silicon photodiode with 2 THz gain-bandwidth product based on cycling excitation process. Applied Physics Letters, 111(10), 101104.

Yu, Y., Yan, L., Zhang, A., Liu, Y. H., Hall, D., Zhou, J., ... & Lo, Y. (2017, October). Quantum detectors using cycling excitation process in disordered medium. In Photonics Conference (IPC), 2017 IEEE (pp. 563-564). IEEE.

ABSTRACT OF THE DISSERTATION

Novel Optical Signal Amplification Mechanisms in Semiconductor Photodetectors

by

Yugang Yu

Doctor of Philosophy in Materials Science and Engineering

University of California San Diego, 2020

Professor Yu-Hwa Lo, Chair

As quantum computing, communication, and sensing play increasingly important roles in the coming decades, and the demands for high sensitivity imaging grow rapidly, the sensitivity of photodetectors has become a main concern in several key technology sectors. This thesis reports two novel light detection and internal amplification mechanisms that enable photodiodes to achieve desired characteristics such as high detection efficiency, single photon sensitivity, low noise and high speed.

Cycling excitation process (CEP) is an intrinsic signal amplification mechanism that was firstly discovered in a heavily-doped compensated Si p/n junction device. By relaxing the k-selection rule (i.e. conservation of momentum), CEP detectors possess high gain, high efficiency, and ultralow noise. Above all, CEP detectors can be made from disordered materials such as amorphous silicon (a-Si), which allows low cost manufacturing and scalability to large array size for intended applications. An a-Si photodiode is demonstrated with ultra-high gain-bandwidth product of 2.25 THz and low noise, based on a very simple structure.

Dark current is a key challenge for photodiodes to detect extremely low power such as single photon as it can produce shot noise. A proper designed based on band gap engineering is shown to reduce the dark current of a-Si CEP detectors. The result of temperature dependent dark current measurement conveys the message that the dark current mechanism of a-Si CEP detectors is indirect tunneling followed by Poole-Frenkel effect. The key part is how to block the electron tunneling without affecting the device photo response. Cupric oxide (Cu_2O) is an intrinsic p-type semiconductor material, with electron affinity of -3.2 eV and band gap of 2.1 eV. By inserting a thin layer of Cu_2O between the a-Si and top electrode, the new structure has a much large electron tunneling barrier. On the other hand, the photogenerated holes can move as before without any additional hole blocking barrier. The measured results support that Cu_2O based dark current reduction CEP devices have at least 1-2 orders of magnitude lower dark current at reverse bias 5 V compared to the typical a-Si CEP detectors while the photo responsivity remain the same.

Realizing that CEP effect occurs in a thin layer of a-Si, we designed an a-Si CEP detector without any semiconductor substrate. The key challenges are to improve the absorption efficiency and frequency response. Utilizing the localized surface plasmon resonance (LSPR) effect incorporated with CEP effect, a plasmonically enhanced a-Si detector achieves high external

quantum efficiency with a record fast impulse response of 170 ps (FWHM). This approach raises the possibility of making detectors out of amorphous materials for high frame rate imaging and optical communications in spite of the low carrier mobilities in the materials.

The second optical signal amplification mechanism was observed in organometallic perovskite based detectors when the input power was down to a few or even single photon. It is a quasi-persistent photo response which takes tens of seconds for the current level to increase and reach to saturation after the absorption of a single photon. Based on the observation, we proposed an internal amplification mechanism, ionic impact ionization (I3), to elucidate the phenomenon, which involves a cascade process of ion migration.

Chapter 1. Introduction

1.1 Light detection in semiconductor

Light is electromagnetic radiation which carries energy and information. For any optoelectronic system such as sensing, imaging and communication, there are two key steps required for light detection. The first step is to convert the input optical signal into electric current signal, which is commonly known as OE conversion, and the second step is to amplify the electric signal to provide decent output signal. Generally, photodetector is used for OE conversion and signal amplification can be achieved in transistor amplifier. Therefore, there is a motivation to integrate the OE conversion and signal amplification into one device. And semiconductor based solid state photodetectors with internal gain greatly attract the attention and are widely used in photodetection applications.

The processes of carrier generation by photon absorption, carrier transportation and extraction of the carriers as terminal current to provide the output signal in photodetection are related to the noise generation, sensitivity, gain and quantum efficiency of the devices. Briefly, quantum efficiency and responsivity define the quality of the OE conversion at a particular wavelength; gain determines how strong the signal is amplified by the detector. In the following sessions, three types of devices: photoconductors, photodetectors and avalanche photodiodes will be introduced and discussed [1-5].

1.2 Photoconductors

A photoconductor consists simply of a slab of semiconductor, in bulk or thin-film form, with ohmic contacts affixed to the opposite ends (Fig. 1.1a). Material conductivity increases when incident light hits the surface of the device, resulting in carrier generation either by photoelectric

effect. These free carriers are generated either by intrinsic band-to-band transition or extrinsic transitions involving impurity states in the forbidden-gap (Fig. 1.1b).

Conductivity for photoconductor is given by $\sigma = q(\mu_n n + \mu_p p)$. Under illumination, the increase in carrier concentration results in the increase of conductivity. The detection wavelength cutoff of intrinsic photoconductor is determined by the semiconductor band gap E_g. Hence it is widely used in the detection of photons with larger energy than E_g. For extrinsic photoconductor, photoexcitation occurs between a band edge and an impurity energy level in the energy gap. In this case, the detection wavelength can be longer such as infrared light. One limitation of this device is the thermal ionization of impurity states, which can be avoided by cooling down the device to cryogenic temperature like 77 K.

Photoconductive gain is defined to evaluate the signal amplification of photoconductors which is the ratio of photo-generated carrier lifetime, τ, to the electron and hole transit times across the electrodes t, i.e, $G = \tau/t$. For high gain, the lifetime is supposed to be long, while the electrode spacing needs to be short and mobilities high. Nonetheless, high photoconductive gain impedes decent response time and speed of a photoconductor, which is also determined by the lifetime. Thus, photoconductors have limited use in high-frequency optical demodulators such as in optical mixing.
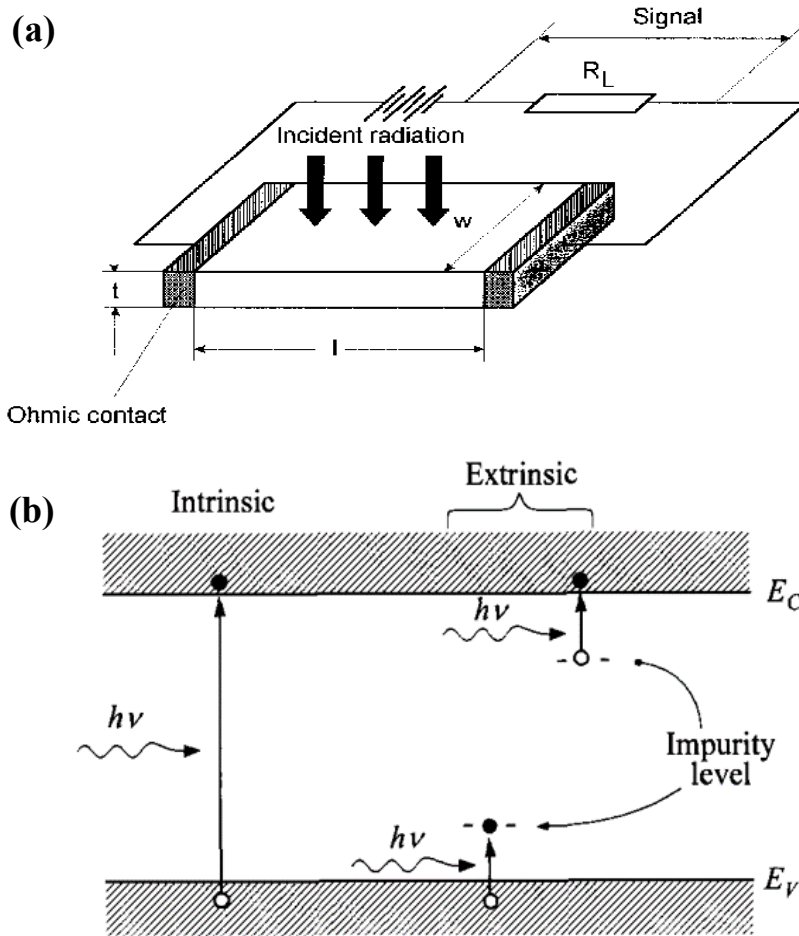
Figure 1.1 **(a)** Geometry and bias of a photoconductor. **(b)** Processes of intrinsic photoexcitation from band to band, and extrinsic photoexcitation between impurity level and band. [1-2]

1.3 Photodiodes

A photodiode is operated under reverse bias (Fig. 1.2a). In a reverse biased photodiode, most of the bias voltage drops in the depletion region. The existing high electric field serves to separate the photogenerated electron-hole pairs fast, while in a neutral n-type or p-type region, the carrier transport is dominated by diffusion process due to the lack of electric field (Fig. 1.2b). For high-speed operation, carrier transit time should be kept short by reducing the width of depletion region. On the other hand, depletion layer must be thick enough to guarantee decent quantum

efficiency as photo-generated carriers are excited within the depletion region. Therefore, there is a trade-off between the device speed response and quantum efficiency.

Quantum efficiency, defined as the number of electron-hole pairs generated per incident photon, is strongly dependent on the optical absorption. For a given semiconductor, the wavelength range in which appreciable photocurrent can be generated is limited. For most photodiodes which apply band-to-band photoexcitation, the long-wavelength cutoff λ_c is determined by the semiconductor band gap. There is also a short-wavelength cutoff of device photo response, which is due to the very large absorption coefficient α, resulting in the radiation absorption too near the surface where recombination is more likely. Hence, the photocarriers tend to recombine before they are drifted and collected by electrodes and form photocurrent.

The response speed of photodiode is limited by three factors: (1) drift time in depletion region, (2) diffusion of carriers, and (3) depletion capacitance. Diffusion is a slow process compared to drift. To minimize the diffusion effect, the junction should be formed close to the surface and sufficiently wide so that most of photocarriers are generated within the depletion region. However, the depletion layer should not be too wide as the transit-time effect will limit the frequency response. To reduce the carrier drift time, the junction needs to be reverse biased to sufficient level and ensure the carriers to be drifted at their saturation velocities. Capacitance of depletion layer, depending on the width of depletion layer, also affects the device speed as an excessive capacitance C will result in a large $R_L C$ time constant. The optimum compromise occurs when the depletion layer is chosen so that the transit time is of the order of one-half the modulation period.
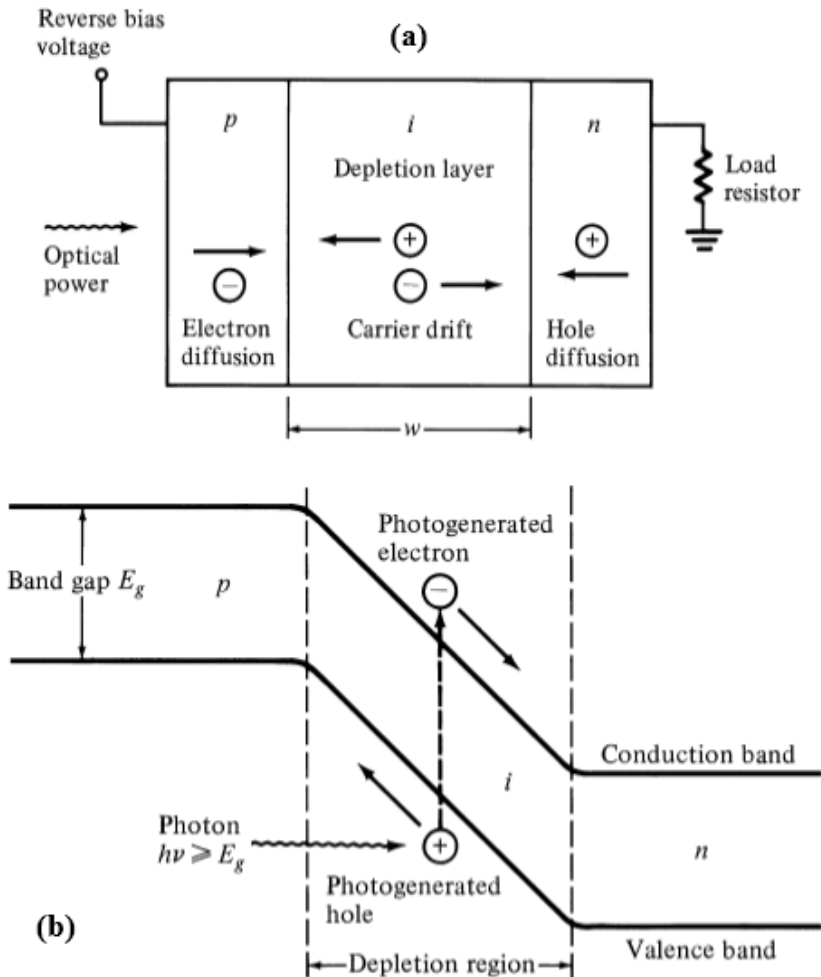
Figure 1.2 (a) Schematic diagram of a reverse biased pin junction and **(b)** corresponding energy band diagram, illustrating intrinsic photogeneration processes. [3]

1.4 Avalanche Photodiodes

To achieve high sensitivity, Avalanche photodiodes (APDs) are operated at high reverse-bias voltages where avalanche multiplication occurs [4]. APDs employ impact ionization which is a carrier multiplication mechanism to accelerate photocarriers to high energies. These accelerated primary carriers have certain probabilities to lose kinetic energy and excite secondary electron-hole pairs to the mobile bands. Secondary e-h pairs are produced and drift together with the primary carriers, these would lead to more new carriers generated on the way across the depletion region (Fig 1.3). The avalanche multiplication gain is given by,

$$M = \frac{\left(1 - \frac{\alpha_p}{\alpha_n}\right)\exp\left[\alpha_n W_D\left(1 - \frac{\alpha_p}{\alpha_n}\right)\right]}{1 - (\alpha_p/\alpha_n)\exp\left[\alpha_n W_D\left(1 - \frac{\alpha_p}{\alpha_n}\right)\right]} \tag{1.1}$$

where W_D is the depletion-layer width and α_n and α_p are the electron and hole ionization rates. Ionization rates of electron and hole are intrinsic properties for a given semiconductor. And they increase exponentially with the electric field across the junction.

In a practical device, the limitation of maximum achievable dc multiplication at high light intensities are the series resistance and the space-charge effect. When the dark current is higher than photocurrent, dark current becomes the limitation of maximum multiplication. Thus, it is important that the dark current is kept as low as possible.

Multiplication noise is an important figure of merit in APDs since the avalanche process is naturally statistical, and every photogenerated electron-hole pair is independent and experiences different multiplication, leading to avalanche gain fluctuation. The noise factor strongly depends on the ratio of the hole and electron ionization rates, α_p/α_n [5]. To minimize the gain fluctuation, it is more desirable to have one carrier dominate during impact ionization process.
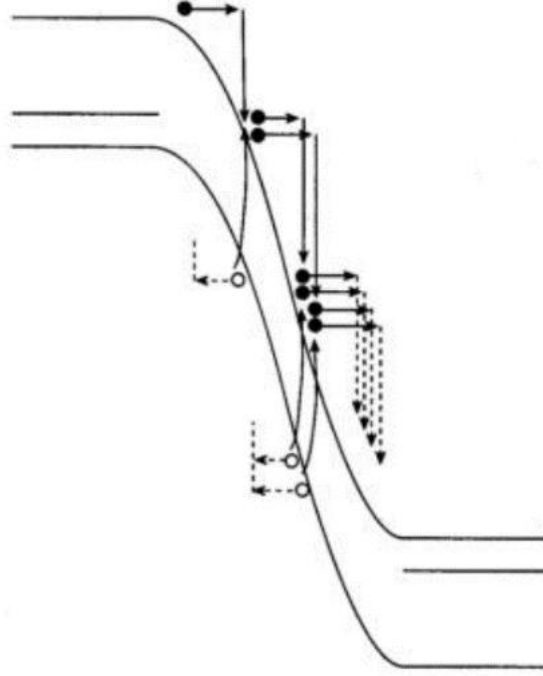
Figure 1.3 Schematic diagram illustration of the carrier multiplication in impact ionization.

1.5 Noise of the Devices

Due to the high dark current, the noise in photoconductor devices is widely known as Johnson or thermal noise, generated by the thermal agitation of the charge carriers [6]. The noise current i_j is modeled by,

$$\bar{i}_j^2 = \frac{4k_B T B}{R_c} \tag{1.2}$$

where B is the bandwidth of the device and R_c is the resistance of the photoconducting channel.

Another source of noise is called generation-recombination noise, which causes the fluctuations in the carrier concentrations. The noise current i_{GR} is given by,

$$\bar{i}_{GR}^2 = \frac{4q\Gamma_G I_0 B}{1+\omega^2\tau^2} \tag{1.3}$$

It's also called shot noise, which can be reduced by operating the devices at low temperature [7]. For photodiode devices, the shot noise is only generated in the depletion region because of the low dark current at reverse bias.

At low frequency range less than 1kHz, flicker noise arises from surface and interface defects and traps in the bulk of the semiconductor [8]. The spectral noise current is given by,

$$\overline{i_f^2} = \frac{i}{f} \tag{1.4}$$

1.6 Motivation

Impact ionization, the prevailing intrinsic mechanism for signal amplification, has been utilized for over 40 years in semiconductor. Despite its avalanche gain at very high reverse-bias voltages, the limitations in carrier excitation efficiency and excess noise impede a higher sensitivity and good SNR. Therefore, there is a motivation to develop new internal gain mechanisms of semiconductor photodetectors to achieve the goals of high sensitivity, high speed response, low excess noise and low operating voltage.

1.7 Synopsis of Dissertation

This dissertation aims to provide and demonstrate novel internal light detection amplification mechanisms. Cycling excitation process (CEP), is one of the new carrier multiplication mechanisms which is more efficient than traditional impact ionization [9]. By relaxing the k-selection rule (i.e. conservation of momentum), CEP detectors possess high gain, high efficiency, and ultralow noise. Above all, CEP detectors can be made from disordered materials such as amorphous silicon, which allows low cost manufacturing and scalability to large array size for intended applications [10]. Apart from CEP, Ionic impact ionization (I3), an avalanche-like process that was observed in organometallic halide perovskite photodetectors, greatly attract my attention. The absorption of a single photon level input power can generate a

persistent photoconductivity of the detector which contributes to its ability to detect single photon in perovskite photodetector device [11].

In chapter 2, a new carrier multiplication mechanism, cycling excitation process (CEP), is introduced. With abundant localized states and strong electron-phonon interactions as the two key physical insights, CEP effect can be achieved in disordered materials such as amorphous silicon (a-Si). And the DC characteristics and high-speed performance of a-Si based CEP detector are presented. Also, the process flow and fabrication of a graphene incorporated a-Si based CEP detector was demonstrated to extend the detection wavelength.

In chapter 3, the dark current mechanism of a-Si based CEP detector is discussed by characterizing the temperature dependent dark current. Corresponding methods involving band gap engineering to reduce dark current are introduced.

In chapter 4, an amorphous Si photodetector made on non-semiconductor platform is discussed. By adding gold nanoparticles into the a-Si layer, the absorption efficiency of the detector is significantly enhanced with the help of localized surface plasmon resonance (LSPR) effect. Improved performance on both the responsivity and the device speed are presented and 3D electromagnetic simulation is conducted to verify the enhancement from gold nanoparticle.

In chapter 5, a small-featured organometallic perovskite photodetector is demonstrated. From the characterization of the frequency and optical power dependent photo response, two different types of photodetection are observed. The first type is the conventional photodetection involving the photon absorption and electron-hole pair generation, while the second type is quasi-persistent photo response which has single photon detection ability. To better explain the quasi-persistent photo response, a photon-triggered ion migration mechanism, ionic impact ionization (I3), is proposed.

In chapter 6, two novel light detection mechanisms, CEP and I3 are summarized and concluded. In addition, a very brief outlook for future projects is discussed.

Reference

1. Razeghi, M. and Rogalski, A., 1996. Semiconductor ultraviolet detectors. *Journal of Applied Physics*, *79*(10), pp.7433-7473.

2. Sze, S.M. and Ng, K.K., 2006. *Physics of semiconductor devices*. John wiley & sons.

3. Rajagopal, K., 2008. *Textbook Of Engineering Physics (Part I)*. PHI Learning Pvt. Ltd..

4. Campbell, J.C., Demiguel, S., Ma, F., Beck, A., Guo, X., Wang, S., Zheng, X., Li, X., Beck, J.D., Kinch, M.A. and Huntington, A., 2004. Recent advances in avalanche photodiodes. *IEEE Journal of selected topics in quantum electronics*, *10*(4), pp.777-787.

5. McIntyre, R.J., 1966. Multiplication noise in uniform avalanche diodes. *IEEE Transactions on Electron Devices*, (1), pp.164-168.

6. Johnson, J.B., 1928. Thermal agitation of electricity in conductors. *Physical review*, *32*(1), p.97.

7. Schottky, W., 1918. Über spontane Stromschwankungen in verschiedenen Elektrizitätsleitern. *Annalen der physik*, *362*(23), pp.541-567.

8. Voss, R.F. and Clarke, J., 1976. Flicker (1 f) noise: Equilibrium temperature and resistance fluctuations. *Physical Review B*, *13*(2), p.556.

9. Liu, Y.H., Yan, L., Zhang, A.C., Hall, D., Niaz, I.A., Zhou, Y., Sham, L.J. and Lo, Y.H., 2015. Cycling excitation process: An ultra efficient and quiet signal amplification mechanism in semiconductor. *Applied Physics Letters*, *107*(5), p.053505.

10. Yan, L., Yu, Y., Zhang, A.C., Hall, D., Niaz, I.A., Raihan Miah, M.A., Liu, Y.H. and Lo, Y.H., 2017. An amorphous silicon photodiode with 2 THz gain-bandwidth product based on cycling excitation process. *Applied Physics Letters*, *111*(10), p.101104.

11. Xu, Z., Yu, Y., Arya, S., Niaz, I.A., Chen, Y., Lei, Y., Miah, M.A.R., Zhou, J., Zhang, A.C., Yan, L. and Xu, S., 2020. Frequency-and Power-Dependent Photoresponse of a Perovskite Photodetector Down to the Single-Photon Level. *Nano Letters*, *20*(3), pp.2144-2151.

Chapter 2. Amorphous Silicon Photodetectors based on Cycling Excitation Process (CEP)

2.1 Discovery of Cycling Excitation Process (CEP)

Cycling excitation process (CEP), a novel carrier multiplication mechanism, was firstly discovered by our group in 2014 [1]. The device where CEP was observed has a structure with highly doped compensated silicon p/n junction. The dopants create abundant localized impurity states near the conduction and valence band edges, which also has strong electron-phonon interactions.

Device cross-sectional structure, top view and band diagram are shown in figure 2.1a, b and c respectively. And CEP process is illustrated in figure 2.2 from (a) to (d). After incident light falls on the device surface and being absorbed by device, the primary electron-hole pair is generated. The primary electron diffuses into the depletion region where the electric field is high and thus gains kinetic energy and becomes hot electron. On the other hand, the primary hole is collected by the cathode. The hot electron with sufficient kinetic energy has a probability to give up part of it to excite another electron from the localized acceptor states via Auger excitation. The excitation of secondary electron makes the localized acceptor state unoccupied. Followed by absorbing a phonon, an electron from the valence band gains energy and excite to the unoccupied state, which produces a hole carrier in the valence band. Similar to the primary electron, this hole is drifted across the depletion region and becomes hot hole, which triggers the excitation of a secondary hole from the localized donor states by losing kinetic energy through Auger excitation. It is equivalent to having an electron from valence band and filling in the localized donor state. The filled electron can be further excited to conduction band by phonon absorption, initiating the

second cycle. Obviously, the two main physical insights are the efficient Auger excitation from

localized states and the phonon absorption associated with shallow impurity states.
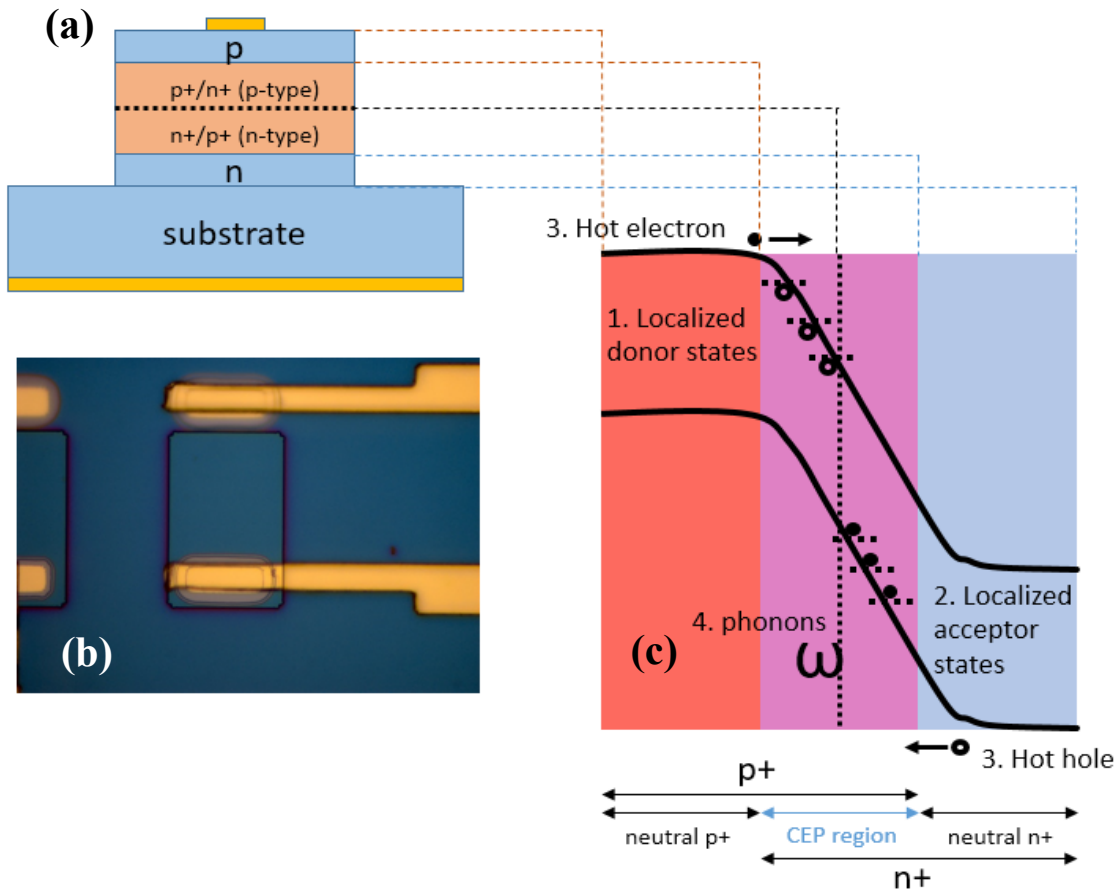
Figure 2.1 CEP device structure in heavily doped and compensated Si p/n junction photodiodes. (a) Cross-sectional structure; **(b)** Top view; **(c)** Band diagram.
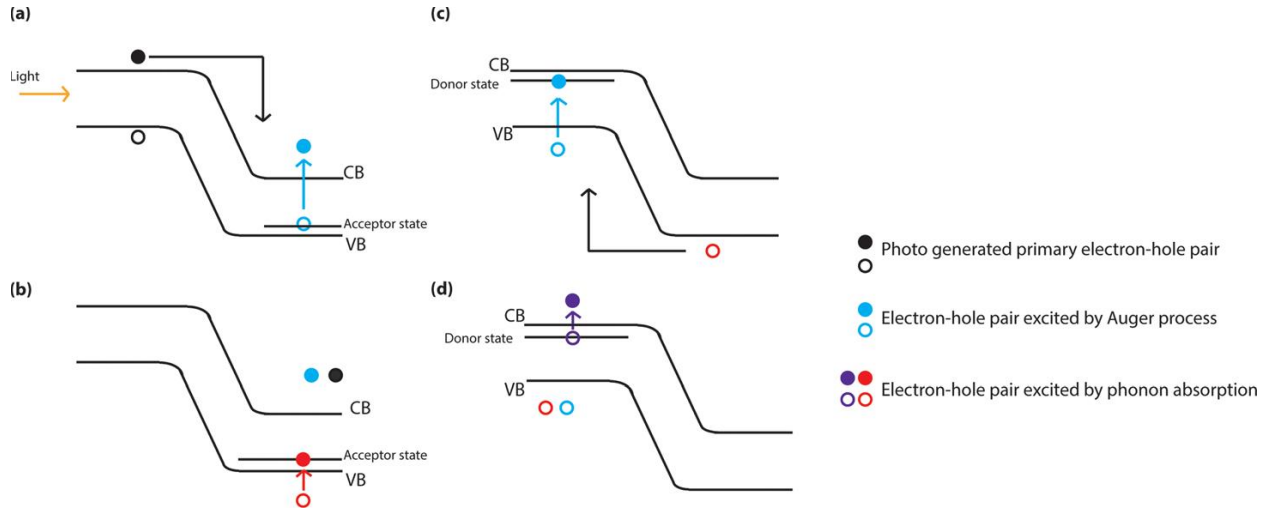
Figure 2.2 Illustration of the cycling excitation process. The processes from a to d take place in sequence: **(a)** Primary photo generated electron excites an electron from a compensating acceptor in the n-region to the conduction band, **(b)** followed by a phonon-absorption process to produce a hole carrier. **(c)** The Auger-cum-phonon created hole may similarly add an electron-hole pair from a compensating donor in the p-region. **(d)** The electron carrier is created by another phonon absorption.

2.2 Amorphous Silicon as CEP gain medium

On the premise that CEP effect utilizes Auger excitation involving localized states and strong electron-phonon interactions, heavily-doped compensated silicon p/n junction has the ability to support CEP effect, with the bias, input light intensity, and temperature dependence of gain measurement results shown in figure 2.3. Despite the high efficiency of signal amplification, the doping concentrations at orders of $10^{19}/cm^3$ raise significant challenges in dark current and process compatibility. We recognize that many disordered semiconductor materials have properties capable of supporting CEP effect. Disordered materials only possess short range order while the long range order is absent. The disordered bonds in those materials intrinsically lead to abundant localized states. In fact, one can treat the heavily-doped compensated p/n junction as a method to turn crystalline silicon into a quasi-disordered materials.
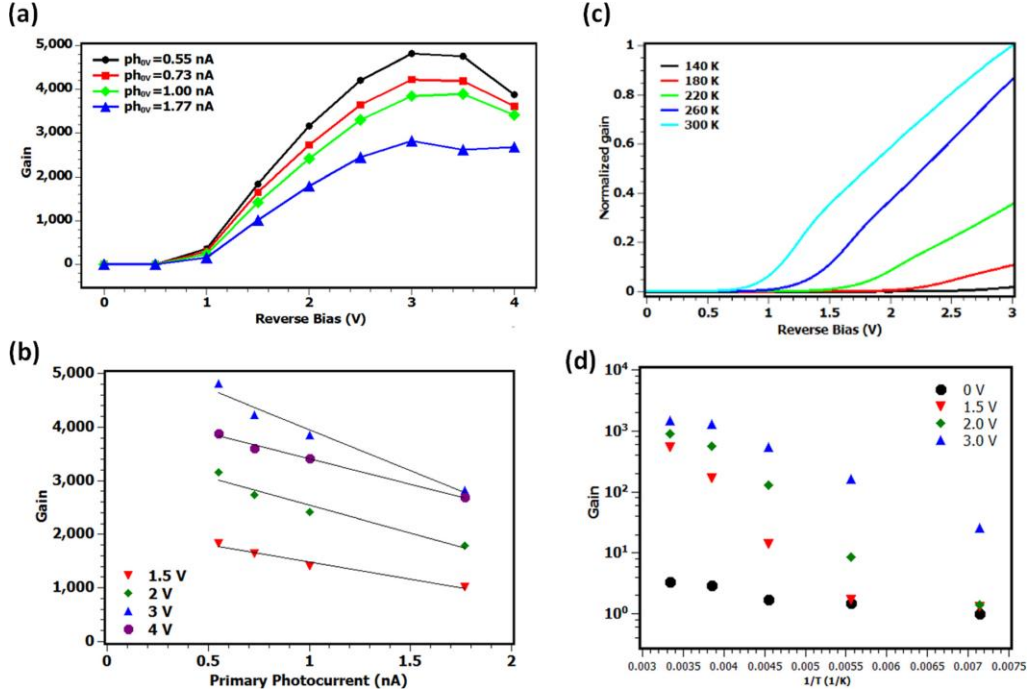
Figure 2.3 Bias, input light intensity, and temperature dependence of gain. **(a)** and **(b)** Bias and input light intensity dependence of gain. The illumination (635 nm) light power is represented by the primary photocurrent at zero volt. **(c)** and **(d)** Temperature dependence of gain under 635 nm illumination in linear and Arrhenius plots. The gain values are normalized to the 300K gain at 3V reverse bias in **(c)**.

Following this rationale, we proposed amorphous silicon (a-Si), as a disordered material, incorporated into the CEP device to present the effect [3]. As the disordered form of silicon, a-Si is disordered at the atomic scale, while the chemical bonding between Si atoms remains the same as in crystalline silicon. The silicon atoms are 4-fold coordinated in a tetrahedral bonding symmetry, but the bond lengths and bond angles vary significantly. In crystalline silicon (c-Si), well-ordered crystal lattice is formed by periodic tetrahedral structure over a large range. However, in amorphous silicon, there is no long range order. Instead, the structure of its atoms behaves like continuous random network model. Additionally, not all the atoms of amorphous silicon are fourfold coordinated [4].

The present of short range order results in a similar overall electronic structure of a-Si compared to c-Si. However, the abrupt band edges of c-Si are replaced by a broadened tail of states

extending into the forbidden band, which is derived from the bond length and angle arising from the long range structural disorder. The density of states of c-Si and a-Si are shown in figure 2.4a and b respectively, consisting of the bands, band tails and defect states in the gap [5].

Apart from the shallow states which locate close to the conduction and valence band edges, there are also deep states within the forbidden band, which are generated mainly by the structural defects and dangling bonds at the a-Si surface (Fig. 2.4c). Although those deep states are localized, they are too deep to excite secondary electron/hole by phonons to continue the cycling. On the other hand, they behave as Shockley-Read Hall recombination centers, which enhance the recombination of photogenerated carriers, unfavorable for quantum efficiency [6]. The most common way to reduce the level of deep states is hydrogen passivation. After passivation, the hydrogen atoms tend to bind those dangling bonds and form Si-H bonds at the surface, like the red atom in figure 2.4c [7-9]. In our experiment, we further introduce a small percentage of carbon (~5%) into the hydrogenated amorphous silicon (a-Si:H) to increase the level of disorder [10] and to tailor the phonon energy and strength of electron-phonon coupling [11].
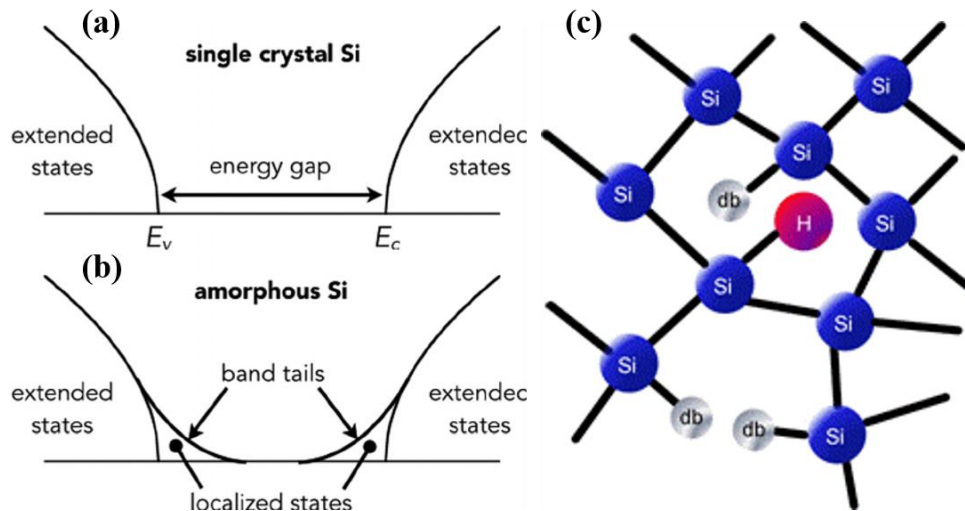
Figure 2.4 (a) Density of states in single crystal, **(b)** Density of states in amorphous silicon, **(c)** Disordered lattice with dangling bonds and hydrogen atom passivation.

2.3 Device Design and Fabrication

Device basic structure is designed as 35 nm hydrogenated a-Si (a-Si:H) CEP layer sandwiched by top electrode and n+-Si substrate. The detailed fabrication process flow is as follows (Fig. 2.5).

The 6-inch {100} n^+-Si wafer is diced into 12mm-by-12mm square samples for device substrate. The diced samples were solvent cleaned, RCA cleaned and immersed into HF (49%) solution for 30s to remove the native oxide (Fig. 2.5a). After substrate preparation, a 35 nm thick amorphous silicon was deposited onto the substrate by PECVD with chamber temperature of 270 ℃. The silane (SiH_4) gas flow rate is 450 sccm. In order to dope 5% carbon into a-Si layer, an additional methane (CH_4) gas was used and its flow rate was set to be 24 sccm. Moreover, during the a-Si growth, 100 sccm hydrogen gas (H_2) was also turned on for H_2 passivation. (Fig. 2.5b). Without taking the samples out of the chamber, a layer of 200 nm SiO_2 was grown right after a-Si deposition using PECVD at 270 ℃ (Fig. 2.5c). This layer was then patterned by photolithography and BOE wet etch, which works as dry etch mask for a-Si etch (Fig. 2.5d, e).

The 35 nm thick layer of a-Si was firstly dry etched by ICP-RIE system for 15 s. After dry etch, the samples were dipped in KOH solution for 5 s for further wet chemical etch, in order to reduce surface states and dangling bonds on the mesa sidewall (Fig. 2.5f).

After etching process, a 30 nm layer of Al_2O_3 was deposited by Plasma Enhanced Atomic Layer Deposition (PE-ALD) for further passivation of surface states and dangling bonds on the mesa sidewall. On top of Al_2O_3, a 150 nm layer of SiO_2 was grown by PECVD to isolate the substrate and top contact (Fig. 2.5g).

To open the window from the oxide layer, the 2nd photolithography was done for the oxide etch (Fig. 2.5h). The oxide layers were then etched chemically by BOE (Fig. 2.5i). The top

electrode of device was chosen to be indium tin oxide (ITO) which is transparent at visible light range and conductive. The 3rd photolithography aimed to pattern the ITO layer (Fig. 2.5j).

A 150 nm layer of ITO was sputtered in magnetron RF sputtering system, at room temperature, followed by a lift-off process in Acetone. The sputtered ITO was then annealed in rapid thermal annealing (RTA) chamber for 1 minute at 300 ℃. After annealing, the ITO layer was more crystallized and chemical resistant (Fig. 2.5k).

The last photolithography was done for the Ti/Au contact layer patterning (Fig. 2.5i). A 200 nm layer of Ti/Au was sputtered in DC sputtering system and worked as metal contact pad for probing during the measurement. Figure 2.6a shows the micrographs of fabricated devices and corresponding band diagram is shown in figure 2.6b.
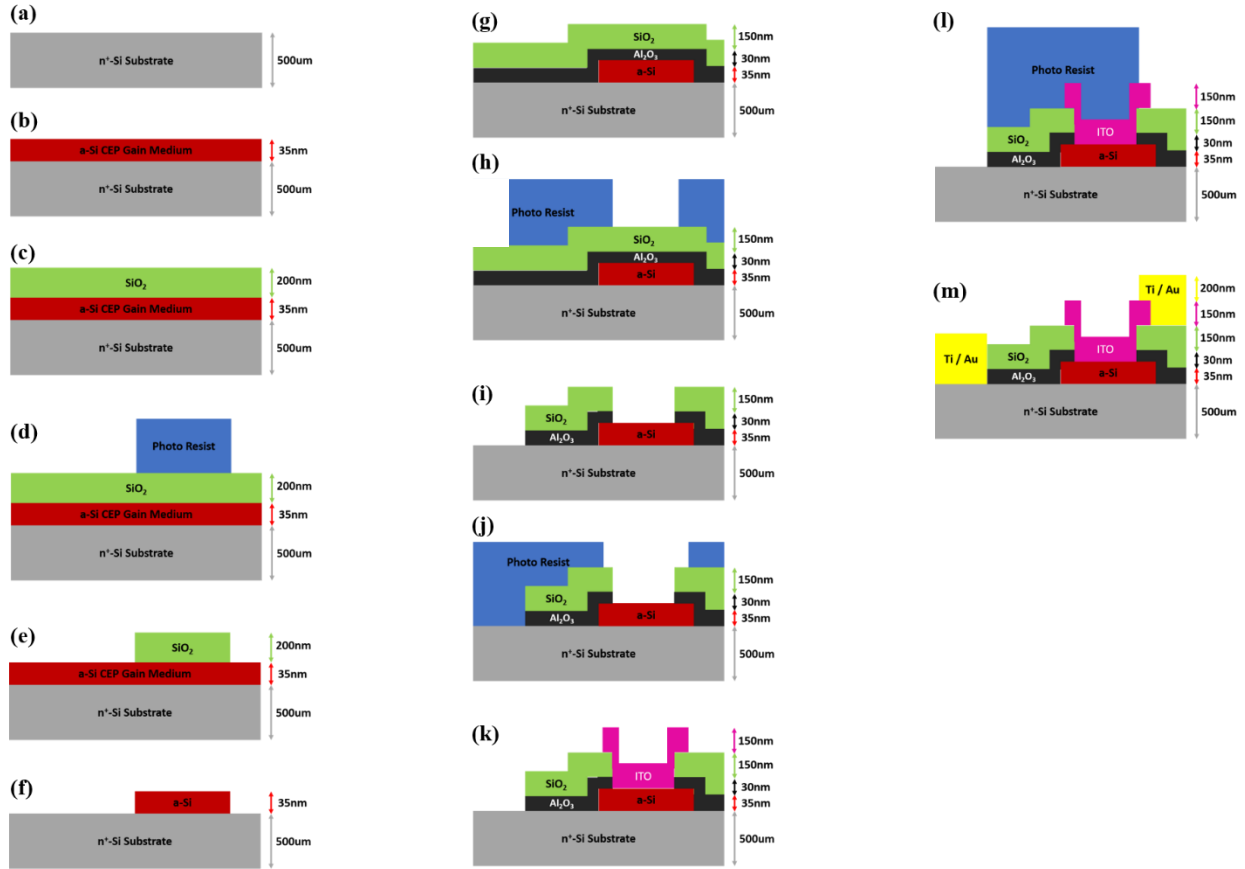
Figure 2.5 Device fabrication process flow. (a) Substrate clean, **(b)** a-Si deposition by PECVD, **(c)** SiO$_2$ deposition by PECVD, **(d)** 1st photolithography for SiO$_2$ chemical wet etch, **(e)** SiO$_2$ after wet etch, **(f)** After a-Si and mesa etch, **(g)** ALD Al$_2$O$_3$ and PECVD SiO$_2$ deposition, **(h)** 2nd photolithography to open windows from oxide layers, **(i)** Oxide layers after BOE wet etch, **(j)** 3rd photolithography for ITO patterning, **(k)** ITO sputtering and lift-off, **(l)** 4th photolithography for Ti/Au patterning, **(m)** Ti/Au deposition and lift-off.
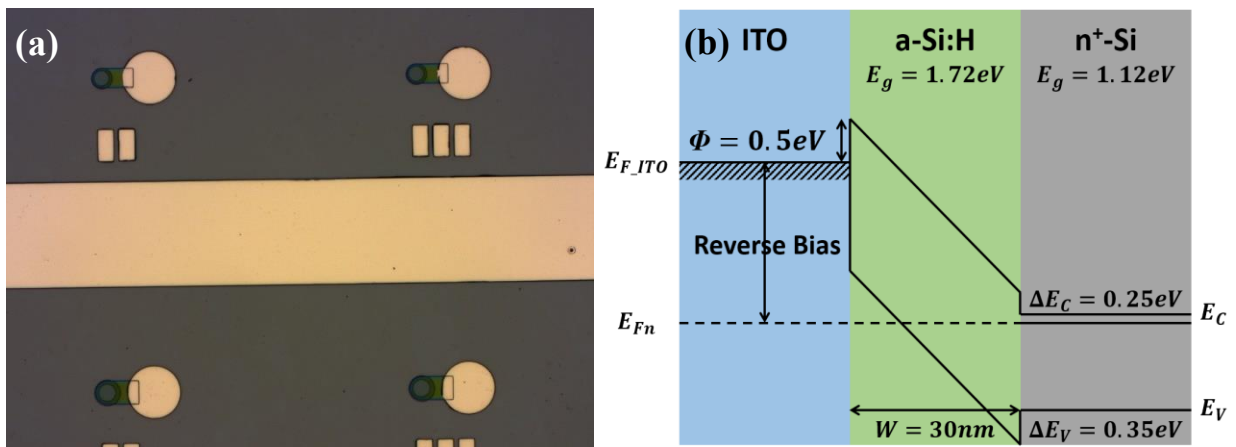
Figure 2.6 (a) Microscopic image of finished devices, **(b)** Band diagram of a-Si CEP device.

18

2.4 Experiment Method

2.4.1 Experiment Optics Setup

We apply the experiment setup as illustrated by the block diagram in Fig. 2.7, which consists of two beam splitters and can couple both the laser light and illumination light together onto the device under test (DUT). Therefore, we are able to visualize the device image as well as laser beam spot from the monitor connected to the CCD camera. Moreover, various lens in front of the first beam splitter can be used to adjust the shape and size of the laser beam spot, and the tunable neutral density filter allows us to attenuate laser input power in order to measure any power dependent characteristics. By adjusting the laser fiber position relative to the system, we can further tune the laser beam spot size.
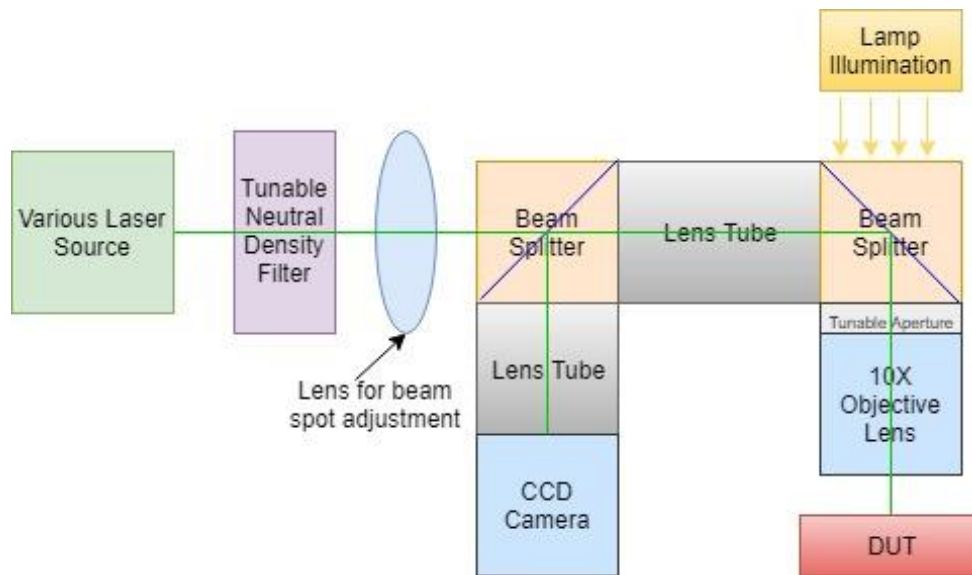
Figure 2.7 Block diagram of the experiment optics setup.

2.4.2 Responsivity and Gain Definition

Responsivity is defined as the ratio between the input power and output photocurrent with the unit of A/W. To better calibrate the input power into the device, we firstly adjusted the laser beam spot size the same as device size. However, due to the limited dynamic range of the CCD

camera, the laser beam spot can appear differently under different input power. The camera tends to be saturated if the input power is too high. But if the input power is too low, the power reading by commercial detector would be strongly fluctuated. Therefore, we have adjusted the power to an optimal range that the commercial detector can read stable power values and the camera is not saturated. For the carbon-doped a-Si device, the 0 V responsivity at 405 nm falls between 0.02 A/W to 0.05 A/W.

The CEP gain of carbon-doped a-Si device is defined as shown in figure 2.8. The input optical signal is represented by the yellow line which is the Continuous Wave (CW) or intensity modulated laser power into the device. At 0 V, the light is absorbed and transferred into photo-current, which we call primary photocurrent under the built-in electric field of 10^5 V/cm. When ramping up the reverse bias, the primary photocurrent is further amplified by CEP gain under higher electric field.
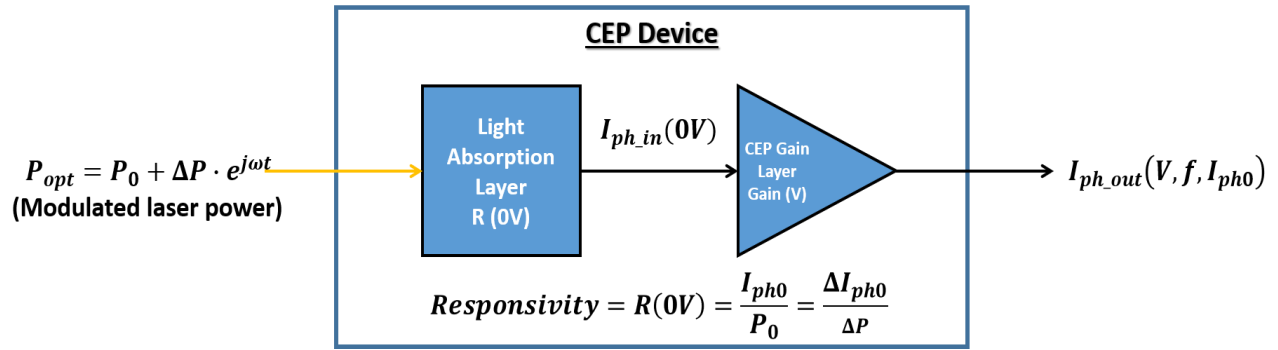
Figure 2.8 Schematic diagram of CEP gain and experiment setup. The yellow line indicates optical signal and black lines represent electrical signal.

The primary photocurrent consists of two parts: I_{p0} as DC photocurrent and ΔI_{p0} as AC part. Thus we have $I_{p0}(0V) = I_{ph0} + \Delta I_{ph0} \cdot e^{jwt}$.

After amplified by CEP gain, the output photocurrent with dependence of voltage and frequency can be defined as $I_{ph}(V,f) = I_{ph} + \Delta I_{ph} \cdot e^{jwt}$. And DC and AC gain of CEP are as follows,

$$G_{DC}(V) = \frac{I_{ph}(V)}{I_{pho}(V)} \tag{2.1}$$

$$g_{ac}(V, f) = \frac{\Delta I_{ph}(V)}{\Delta I_{pho}(V)} \tag{2.2}$$

2.5 Device DC Characteristics

Device DC characteristics was characterized by precision source meter, Agilent B2912A. Figure 2.9a and b show the device DC dark current and photocurrent gain correspondingly. Also, dark current comparison of devices with different design is also shown in figure 2.9a. The green curve represents the dark current of heavily-doped compensated p/n junction CEP device. As discussed in section 2.2, the heavily-doped compensated p/n junction CEP device raises a significant challenge in dark current reduction due to the high doping concentration. By doping 5% carbon into the a-Si:H, device dark current shows a prominent reduction caused by the band gap tailoring and disorder level enhancement.

The photo response measurement was done at 405 nm laser to probe the intrinsic properties of CEP effect in amorphous silicon layer, because the absorption of 405 nm is shallow and most photons are absorbed within the a-Si layer. The result in figure 2.9b indicates that by adding 5% carbon, not only the dark current is suppressed but also the photocurrent gain is enhanced.
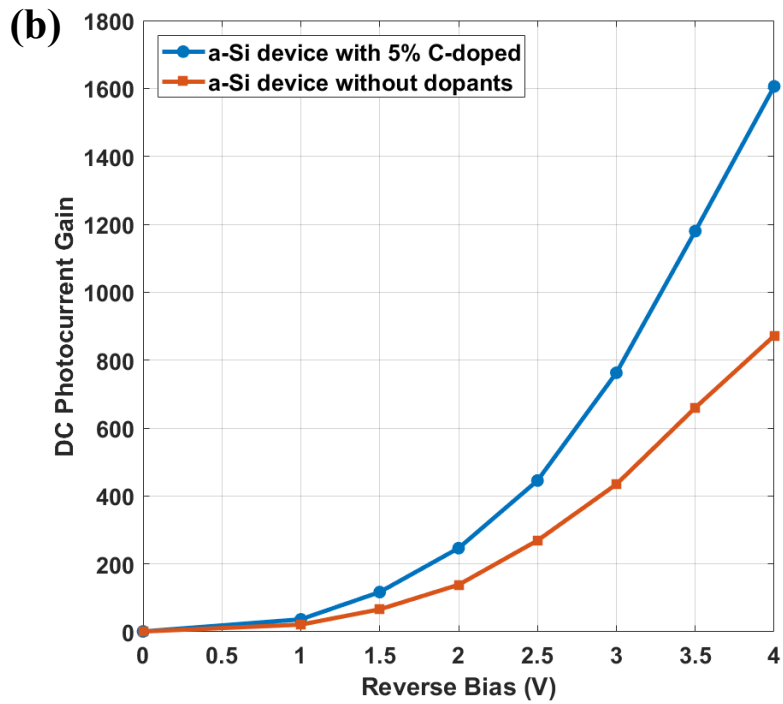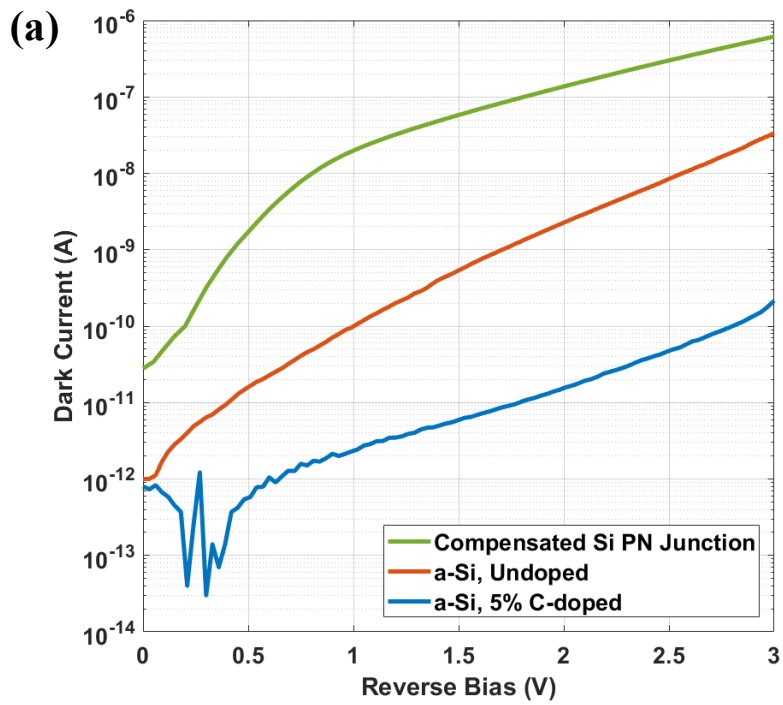
Figure 2.9 DC characteristics of CEP photodetector devices. (a) Dark current summary of different design of CEP devices, **(b)** Photocurrent gain of a-Si CEP devices.

22

2.6 Gain Bandwidth Product

2.6.1 High Speed Measurement Setup and Method
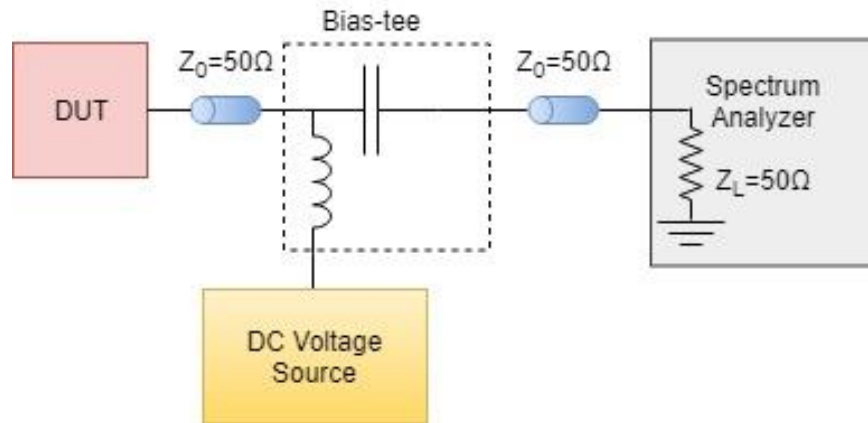
Figure 2.10 Schematic circuit diagram for the high-speed measurement.

The high-speed measurement setup is based on a transmission line model, of which the effects of signal attenuation, reflections and cable length and loss are considered (Fig. 2.10). To ensure the high-speed operation, a GSG probe (up to 40 GHz) was used to make device contacts. And all cables in the setup are high-frequency SMA cables. A bias-tee circuit is used to decouple the signal output from device into DC and AC components. The DC part is connected to the source meter for reverse bias supply, and the AC component passes the capacitor in bias-tee and collected by spectrum analyzer which has an internal current preamplifier with an input impedance of 50 Ω.

2.6.2 AC Measurement Results

The frequency dependence of photocurrent gain under different bias voltages is shown in figure 2.11. The 3-dB cutoff of photocurrent gain occurs at 1 GHz to 1.5 GHz under all bias voltages. Generally, the cutoff frequency is supposed to be almost voltage independent, so the cutoff shown in the frequency-gain plot is likely due to the RC roll off instead of intrinsic device bandwidth. Follow this assumption, one can make a conservative estimate of the gain-bandwidth product by taking 1.5 GHz as the device intrinsic bandwidth, multiplying the gain of 1500 under

reverse bias 4 V, which yields a gain-bandwidth product of 2.25 THz for carbon-doped a-Si:H device. This value exceeds the one of best performance APDs, which is around 300 GHz [12-14].
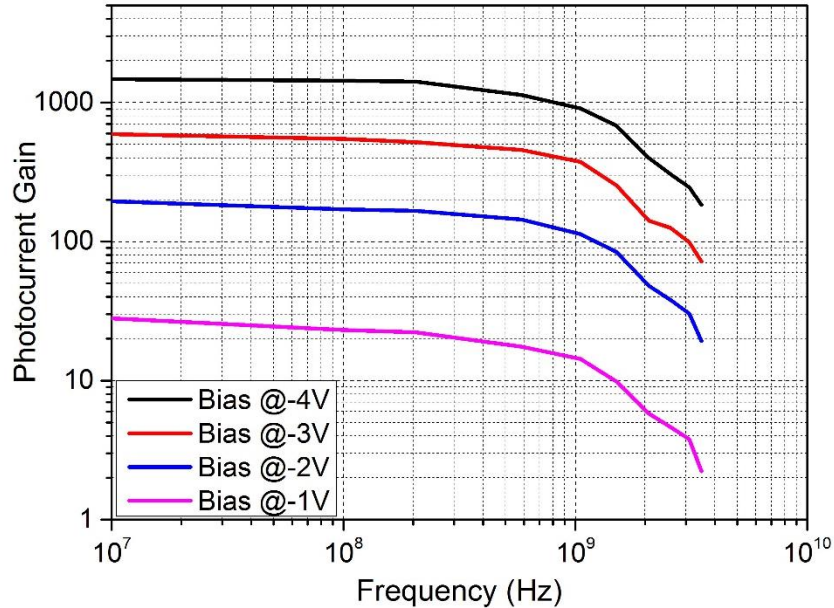
Figure 2.11 The AC photocurrent gain versus the laser modulation frequency is plotted under four different reverse bias voltages.

2.7 CEP Model in a-Si Photodiode

CEP effect in a-Si:H device is similar as in heavily-doped compensated p/n junction device. Figure 2.12 shows the cycling process in a-Si:H device. Amorphous silicon is commonly known as a material with very low carrier mobilities [15], which prevent the carriers from gaining sufficient kinetic energy and trigger Auger excitation. It is valid for the case that the electric field is low across a relatively thick a-Si layer while in our experiment, the device is designed to have a thin layer of a-Si (30 nm), which leads to a strong electric field (over 10^6 V/cm) under reverse bias. The carriers are more likely to undergo ballistic transport and gain sufficient kinetic energy as all inelastic scatterings cannot relax the energy fast enough. Though the layer is small, it is enough for an energetic carrier to trigger Auger excitation as it occurs within a distance of a few

nanometers, which is 10 to 100 times shorter than the required length for impact ionization. And

the high density of localized states in a-Si gives rise to the environment.
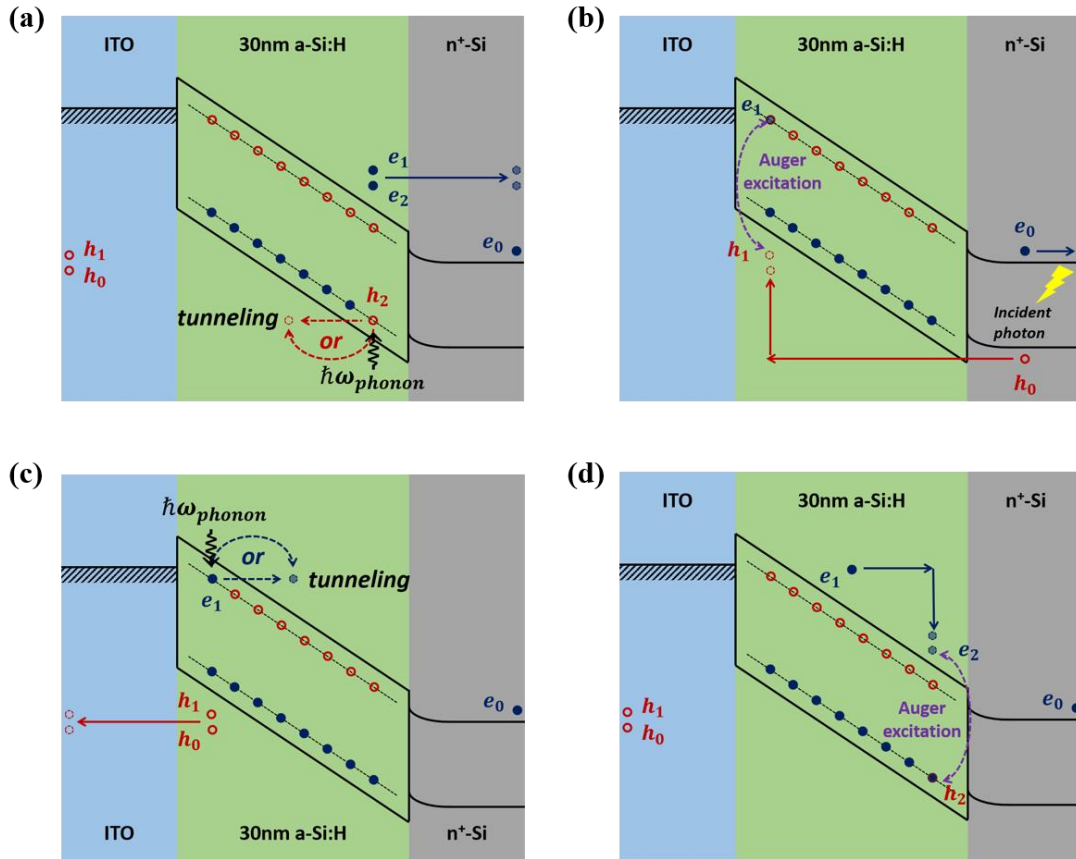
Figure 2.12 Cycling excitation process (CEP) model in a-Si. **(a)** Primary electron-hole pair is generated in the n+-Si substrate. While the primary electron is collected by the electrode, the primary hole enters the a-Si CEP region and accelerated by the electric field. The energetic hole initiates an Auger process to excite a localized hole from a conduction bandtail state to the valence band, leaving a localized electron at that state. **(b)** This electron filling the localized state can be transferred to the conduction band by phonon absorption or field-assisted tunneling. Meanwhile, the primary and excited holes are collected by the electrode. **(c)** The electron excited in (b) gains kinetic energy as it travels in the a-Si and initiates another Auger process to excite a localized electron from a valence bandtail state to the conduction band, leaving a localized hole at that state. **(d)** Similar to part b, by phonon absorption or field-assisted tunneling, the hole, left in the localized bandtail state, can transfer into the valence band and start the subsequent cycle. [3]

Portion of Chapter 2 has been published in the following publication: Yan, L., Yu, Y.,

Zhang, A.C., Hall, D., Niaz, I.A., Raihan Miah, M.A., Liu, Y.H. and Lo, Y.H., 2017. An

amorphous silicon photodiode with 2 THz gain-bandwidth product based on cycling excitation

process. Applied Physics Letters, 111(10), p.101104. The dissertation author is the primary

investigator/secondary author of the paper.

Reference

1. Liu, Y.H., Yan, L., Zhang, A.C., Hall, D., Niaz, I.A., Zhou, Y., Sham, L.J. and Lo, Y.H., 2015. Cycling excitation process: An ultra efficient and quiet signal amplification mechanism in semiconductor. *Applied Physics Letters*, *107*(5), p.053505.

2. Zhou, Y., Liu, Y.H., Rahman, S.N., Hall, D., Sham, L.J. and Lo, Y.H., 2015. Discovery of a photoresponse amplification mechanism in compensated PN junctions. *Applied Physics Letters*, *106*(3), p.031103.

3. Yan, L., Yu, Y., Zhang, A.C., Hall, D., Niaz, I.A., Raihan Miah, M.A., Liu, Y.H. and Lo, Y.H., 2017. An amorphous silicon photodiode with 2 THz gain-bandwidth product based on cycling excitation process. *Applied Physics Letters*, *111*(10), p.101104.

4. Street, R.A., 2005. *Hydrogenated amorphous silicon*. Cambridge university press..

5. Horowitz, G., 2015. Validity of the concept of band edge in organic semiconductors. *Journal of Applied Physics*, *118*(11), p.115502.

6. Guha, S. and Hack, M., 1985. Dominant recombination process in amorphous silicon alloys. *Journal of applied physics*, *58*(4), pp.1683-1685.

7. Galloni, R., Tsuo, Y.S. and Zignani, F., 1989. Ion implantation and hydrogen passivation in amorphous silicon films. *Nuclear Instruments and Methods in Physics Research Section B: Beam Interactions with Materials and Atoms*, *39*(1-4), pp.386-388.

8. Luft, W. and Tsuo, Y.S., 1993. *Hydrogenated amorphous silicon alloy deposition processes* (p. 128). New York: Marcel Dekker..

9. Descoeudres, A., Barraud, L., De Wolf, S., Strahm, B., Lachenal, D., Guérin, C., Holman, Z.C., Zicarelli, F., Demaurex, B., Seif, J. and Holovsky, J., 2011. Improved amorphous/crystalline silicon interface passivation by hydrogen plasma treatment. *Applied Physics Letters*, *99*(12), p.123506.

10. Chew, K., Rusli, Yoon, S.F., Ahn, J., Zhang, Q., Ligatchev, V., Teo, E.J., Osipowicz, T. and Watt, F., 2002. Gap state distribution in amorphous hydrogenated silicon carbide films deduced from photothermal deflection spectroscopy. *Journal of applied physics*, *91*(7), pp.4319-4325.

11. Bullot, J. and Schmidt, M.P., 1987. Physics of amorphous silicon–carbon alloys. *physica status solidi (b)*, *143*(2), pp.345-418.

12. Lenox, C., Nie, H., Yuan, P., Kinsey, G., Homles, A.L., Streetman, B.G. and Campbell, J.C., 1999. Resonant-cavity InGaAs-InAlAs avalanche photodiodes with gain-bandwidth product of 290 GHz. *IEEE Photonics Technology Letters*, *11*(9), pp.1162-1164.

13. Kang, Y., Liu, H.D., Morse, M., Paniccia, M.J., Zadka, M., Litski, S., Sarid, G., Pauchard, A., Kuo, Y.H., Chen, H.W. and Zaoui, W.S., 2009. Monolithic germanium/silicon avalanche photodiodes with 340 GHz gain–bandwidth product. *Nature photonics*, *3*(1), pp.59-63.

14. Kinsey, G.S., Campbell, J.C. and Dentai, A.G., 2001. Waveguide avalanche photodiode operating at 1.55 μm with a gain-bandwidth product of 320 GHz. *IEEE Photonics Technology Letters*, *13*(8), pp.842-844.

15. Moore, A.R., 1977. Electron and hole drift mobility in amorphous silicon. *Applied Physics Letters*, *31*(11), pp.762-764.

Chapter 3. Dark Current Reduction for a-Si based CEP device

3.1 Dark Current in Photodetector

Photodetectors apply photoelectric effect to convert the input optical signal into electric current signal. However, even in the absence of any light input, there is always some small amount of DC current, which people call the dark current. Thought the dark current is usually very low, it matters when a detector is designed to detect extremely small optical power, such as single photon detector [1-3]. The lower the dark current is, the weaker the shot noise it can produce.

Dark current of a photodetector can have different origins. In some photodiodes with p-n or p-i-n junction, thermal excitation of carriers produces dark current. The thermally generated carriers are not necessarily produced from valance band to conduction band, but more likely through defect states related to crystal defects and impurities since the thermal energy is relatively low compared to the band gap of most semiconductors. Thermal generation rate significantly depends on the device active area, temperature and band gap energy of the material. For visible light detectors such as silicon-based photodiodes, dark current from thermal excitation can be very small due to the large band gap. However, for materials with substantially smaller band gap, dark current from thermally generated carriers is a serious issue and may thus enforce the operation at reduced temperatures.

Besides the dark carriers generated in semiconductor materials internally, the carrier emission and injection from the electrodes are also sources of the dark current in photodetectors. Thermionic emission is one of the primary causes for a dark current. The thermionic emission theory assumes that electrons, with an energy larger than the top of the barrier, will cross the barrier provided they move towards the barrier [4]. The current density can be expressed by [5],

$$J_{t-e} = AT^2 \exp\left(-\frac{q\phi_B}{kT}\right)\left(\exp\left(\frac{qV}{kT}\right) - 1\right) \tag{3.1}$$

where A is Richardson coefficient and $A = \frac{4\pi q m^* k^2}{h^3}$, T is lattice temperature, $\emptyset_B$ is the barrier height, V is applied bias.

When photodiodes are operated at higher bias voltages, there can be a steeper rise of dark current induced by field emission. Under the high electric field, carriers from the electrodes can tunnel through the barriers and cause high dark current. The tunneling current can be derived from time independent Schrodinger equation by calculating the tunneling probability. And the tunneling current density can be expressed by Fowler-Nordheim model [6],

$$J_{FN} = \frac{q^2 E^2}{8\pi h \emptyset_B} \exp\left(-\frac{8\pi\sqrt{2qm^*}\emptyset_B^{3/2}}{3hE}\right) \tag{3.2}$$

where E is the electric field and V is the bias voltage.

The other origins of dark current are weak contribution coming from the leakage current due to non-perfect electrical isolation and some unwanted light generated by scintillation, e.g. when electrons hit the glass tube. At a usually very low level, there are weak flashes of light caused by cosmic rays and radioactive substances e.g. in the glass tube or the near surroundings.

3.2 Dark Current Mechanism in a-Si based CEP Device

3.2.1 Temperature dependent dark current characterization

For the carbon-doped a-Si:H CEP detector, the band diagram and possible paths for dark current is shown in figure 3.1. The blue solid dots represent the transport of electrons from ITO cathode, and the red empty dots show the transport of holes from n$^+$-Si substrate. Considering the electron transport, there are 3 main paths of dark current: thermionic emission (rightmost), indirect tunneling followed by Poole-Frenkel effect (middle) and direct tunneling (leftmost).
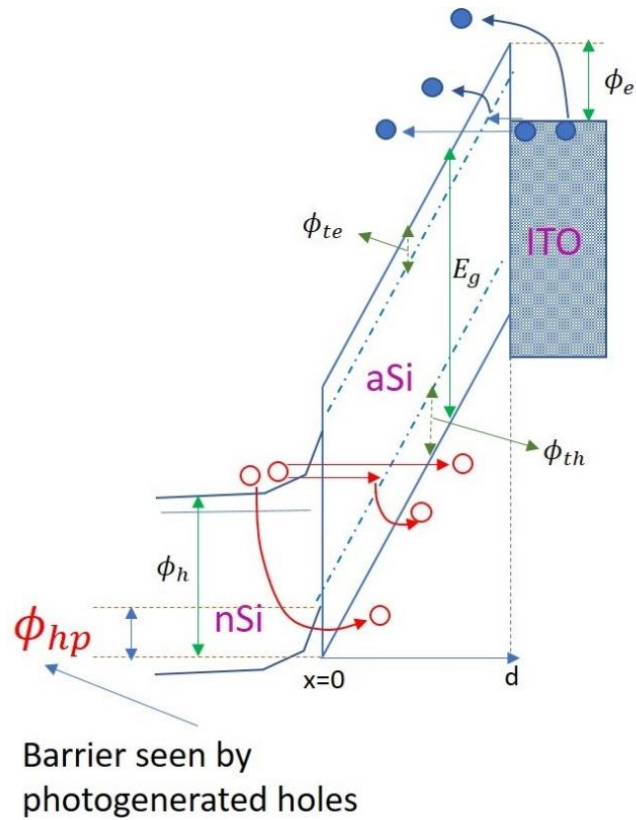
Figure 3.1 Device band diagram and possible paths for dark current. Blue solid dots represent paths for electron transport and the red empty dots represent paths for hole transport.

To better understand the main source of dark current in the a-Si CEP device, we conducted

temperature dependent dark current measurement. The temperature was controlled by LakeShore

CRX-4K probe station system. Figure 3.2a shows the results of temperature dependent dark current

from 250 K to 100 K. By extrapolating the data at reverse bias 4 V and 5 V, we plotted the dark

current versus 1000/T figure illustrated in figure 3.2b. The slope shown in the plot indicates the

activation energies of the carrier emission.

(a)

(b)
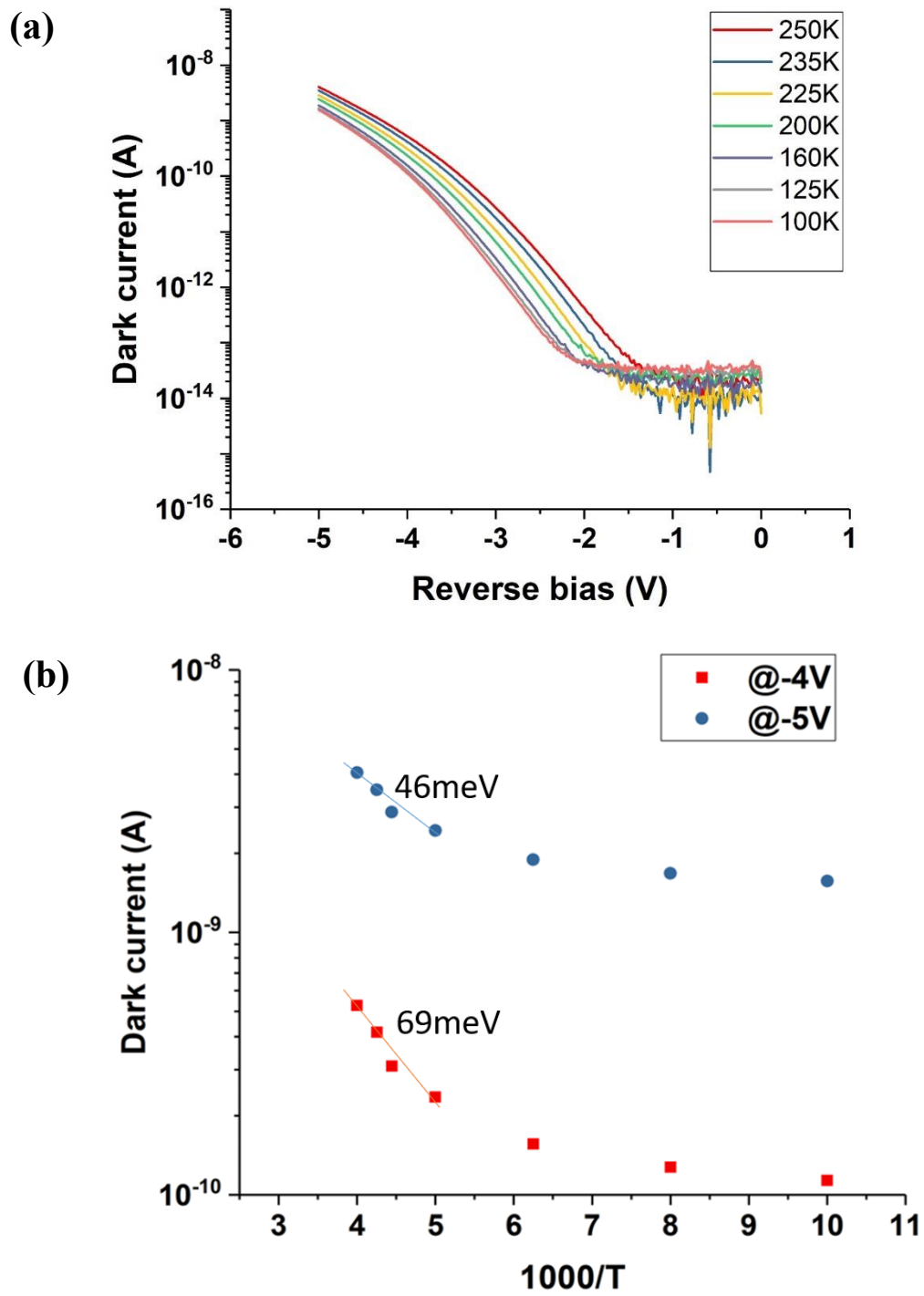
Figure 3.2 (a) Temperature dependent dark current characterization of a-Si CEP device, **(b)** Dark current versus 1000/T plot.

The activation energies are around 70 meV, which is one order of magnitude smaller than the Schottky barrier between ITO and a-Si (0.7 eV). Hence, the dark current contributed by thermionic emission is negligible. Moreover, the dark current is indeed temperature dependent, excluding the possibility of pure carrier tunneling. Therefore, the indirect tunneling followed by Poole-Frenkel effect could be the main source of device dark current.

3.2.2 The Poole-Frenkel effect (PFE)

The PFE is applicable if the trap center is neutral with the captured carrier (e⁻, h⁺), as only then an attractive (coulomb) interaction is working when the charged carrier escapes from the charged trap [10]. The general picture of PFE is sketched in figure 3.3: $\Delta\emptyset_{tn}$ is the barrier for electron to escape from its trapped state into the conduction band. Symmetrically, $\Delta\emptyset_{tp}$ is the barrier for hole to escape from its trapped state into the valence band, which is not presented in the diagram for simplicity. When there is no electric field present, the barriers are equal in both directions in this simplified linear model. It is changed after the electric field E is introduced. In forward direction (in this case, the direction of the drift of the electrons, right towards), the barrier is reduced by $\Delta\emptyset_{PF}$ compared to the field free state contributed by the applied and/or internal electric field E with appropriate sign. A field with the opposite sign enlarges the barrier in the same direction by about the same value. Generally, $\Delta\emptyset_{PF}$ is similar to the case where the thermionic emission is affected with an electric field for the Schottky effect (SE). And from the coulomb interaction between the leaving carrier and remaining charged trap,

$$\Delta\emptyset_{PF} = \sqrt{\frac{qE}{\pi\epsilon_r\epsilon_o}} \tag{3.3}$$

where q is the charge. ε_0 the vacuum permittivity, and ε_r the relative optical (high frequency) permittivity (relative optical dielectric constant) of the thin film material.
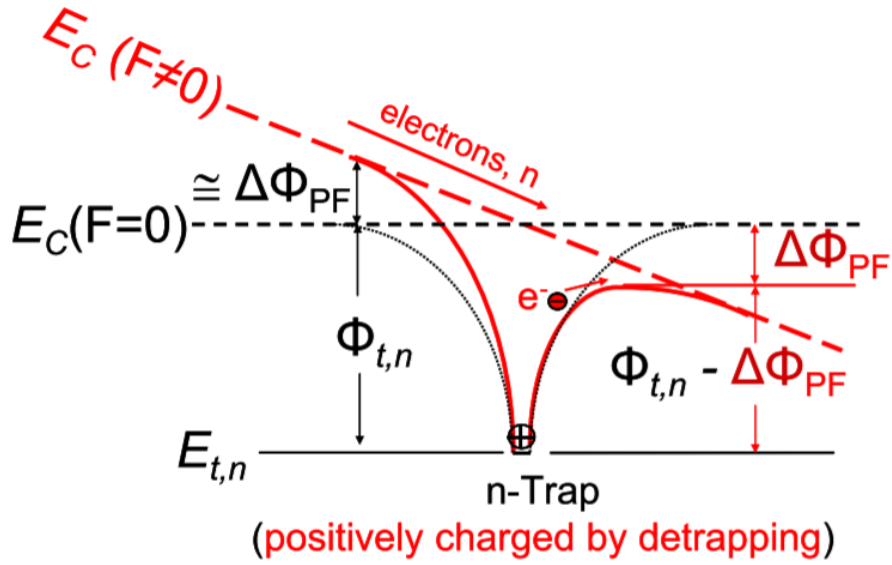
Figure 3.3 Schematic sketch of the Poole-Frenkel-effect without and with electric field, F. [11]

With the reduced barrier, the electron and hole escaping from the trap states happens more often, contributing to higher densities of free carriers, n_{PF} (electrons) or p_{PF} (holes), in the mobile bands than without the Poole-Frenkel effect. Hence the increased PF-conductivity induced by the carrier densities can be written as,

$$\sigma_{PF} = q\mu_n n_{PF} = q\mu_n n_0 \exp\left(\frac{q\Delta\emptyset_{PF}}{kT}\right)$$

(3.4)

replacing $\emptyset_{PF}$ by equation (3.3), we have,

$$\sigma_{PF} = q\mu_n n_0 \exp\left(\frac{q}{kT}\sqrt{\frac{qE}{\pi\epsilon_r\epsilon_o}}\right) \qquad (3.5)$$

From equation (3.5), we can find the PF current density,

$$J \propto E\,exp\left\{-\frac{q}{kT}\left(\emptyset_{te} - \sqrt{\frac{qV}{\pi\epsilon_r\epsilon_o d}}\right)\right\} \qquad (3.6)$$

where $\emptyset_{te}$ is the energy barrier between trap states to mobile band, shown in figure 3.1. V is the applied bias and d is thickness of the thin film.

From equation (3.6), we can find the activation energy of PFE,

$$E_a = \emptyset_{te} - \sqrt{\frac{qV}{\pi\epsilon_r\epsilon_o d}} \tag{3.7}$$

By fitting E_a vs. $\sqrt{V}$, we are able to find the slope and intercept so that find the fitting parameters $\emptyset_{te}$ and ϵ_r (Fig. 3.4). The fitting parameters are $\epsilon_r = 13.86$ and $\phi_{te} = 0.3\text{ eV}$. Considering the relative permittivity of amorphous Si is 14 [12], the data fitting supports our thought that the main source of dark current of carbon-doped a-Si CEP device is the indirect tunneling followed by Poole-Frenkel effect.
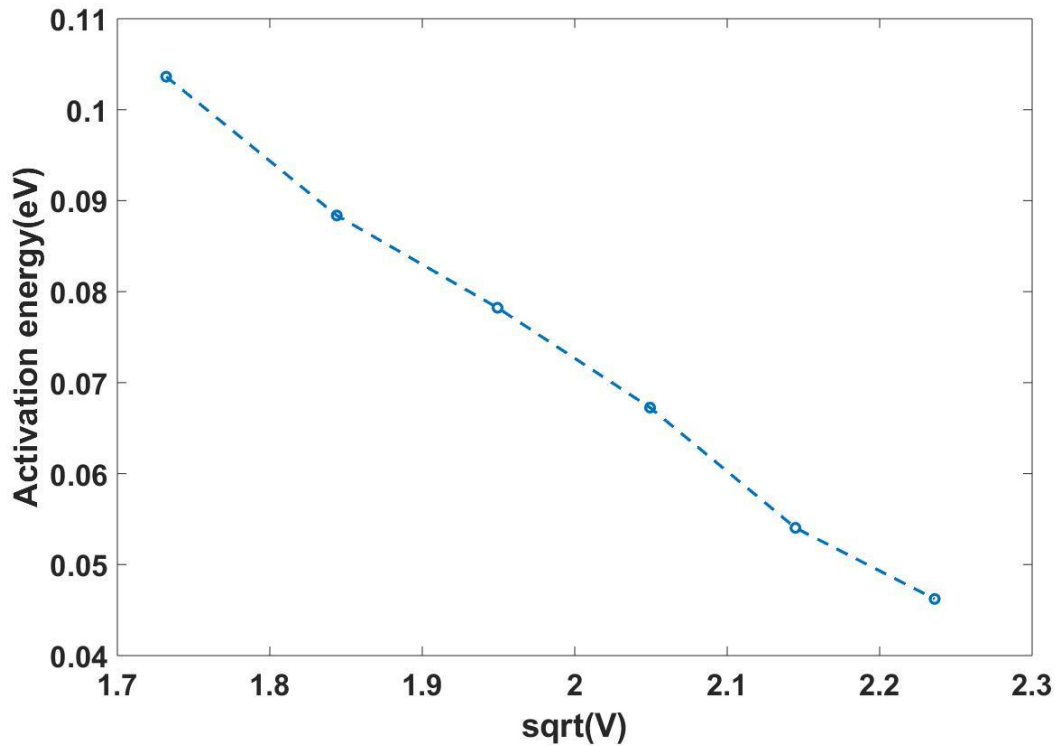
Figure 3.4 Activation energy with dependence of square root of reverse bias voltages from 3 V to 5V.

3.3 Experiment Design by Band-gap Engineering

3.3.1 Cupric oxide (Cu₂O) as electron blocking layer

Given that the primary source of dark current for a-Si CEP detectors is indirect tunneling followed by Poole-Frenkel emission, our focus is on the techniques that can suppress the pathway.

The general concept is to insert an intermediate layer of material of proper bandgap and electron affinity to raise the effective tunneling barrier. This should be done without adversely affecting other performance metrics such as quantum efficiency and gain. One possible material candidate is cupric oxide (Cu_2O).

Cu2O is intrinsically p-type semiconductor material with electron affinity of -3.2 eV and band gap of 2.1 eV [12]. For carbon-doped a-Si on n^+-Si substrate device, introducing Cu2O as electron tunneling barrier between a-Si and top electrode fulfills our requirement to reduce dark current while maintain the photo response level. The corresponding band diagram of the structure is shown in figure 3.5.
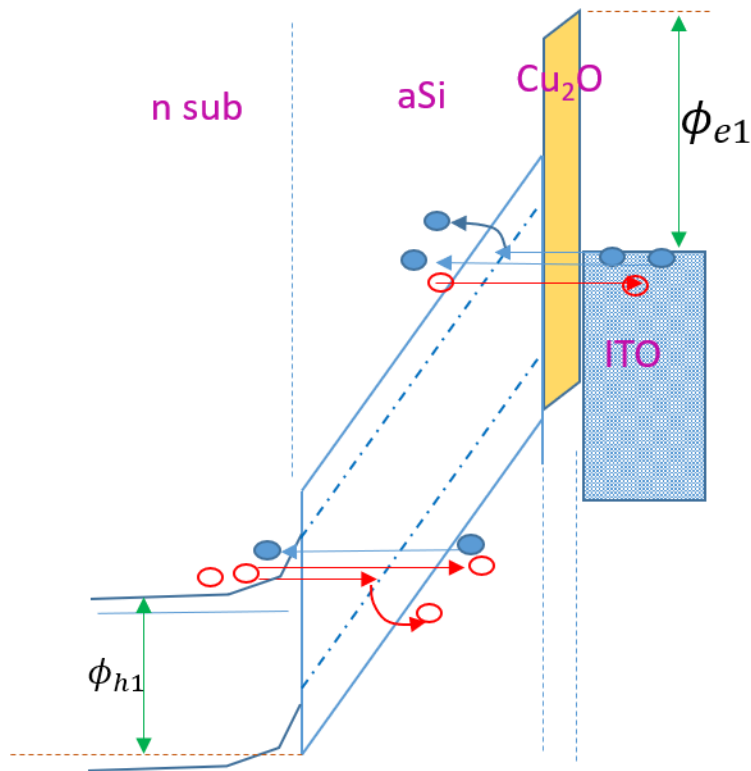
Figure 3.5 Band diagram of ITO/Cu2O/a-Si structure.

Cu_2O thin film can be deposited by sputtering and pulsed laser deposition (PLD) at room temperature followed by post-annealing at 200 °C for 10 hours. With nitrogen-doped, the doping concentration of the Cu_2O thin film would increase, so as the conductivity and mobility of the

material [13]. Figure 3.6a shows XRD patterns of reactive sputtered Cu2O thin films with different

N-doping. And figure 3.6b includes the data of Hall effect measurement of the same thin films,

which supports the statement that with higher N_2 doping, the thin film becomes more and more p-

type and conductive.
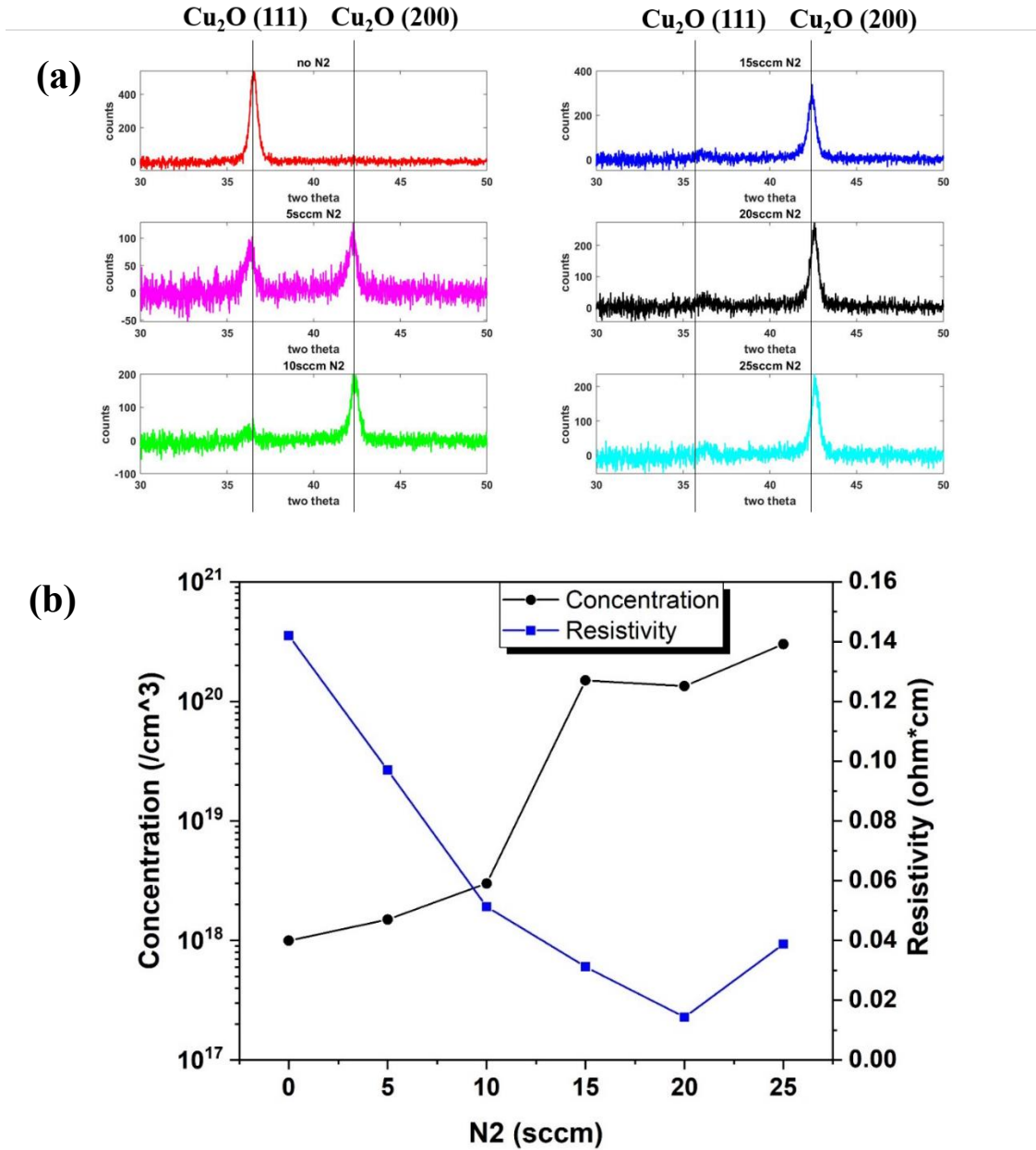
Figure 3.6 Material characterization of reactive sputtered Cu2O thin films. **(a)** XRD patterns, **(b)** Hall measurement results.

3.3.2 Device Structure and Fabrication

The structure of dark current reduction a-Si CEP detector is simply by adding a thin layer of Cu_2O between a-Si and ITO compared to typical a-Si CEP device (Fig. 3.7). And the process flow of device follows the same one of typical a-Si CEP device illustrated in figure 2.5. Before patterning the top ITO electrode, an additional photolithography was done to define the Cu_2O patterns. The Cu2O layer was grown by pulsed laser deposition (PLD) at room temperature, followed by acetone lift-off and post-annealing at 200 °C for 10 hours. After the Cu2O layer deposition and post-treatment, top ITO electrode and Ti/Au contact pads were deposited as shown in figure 2.5 step j to m.
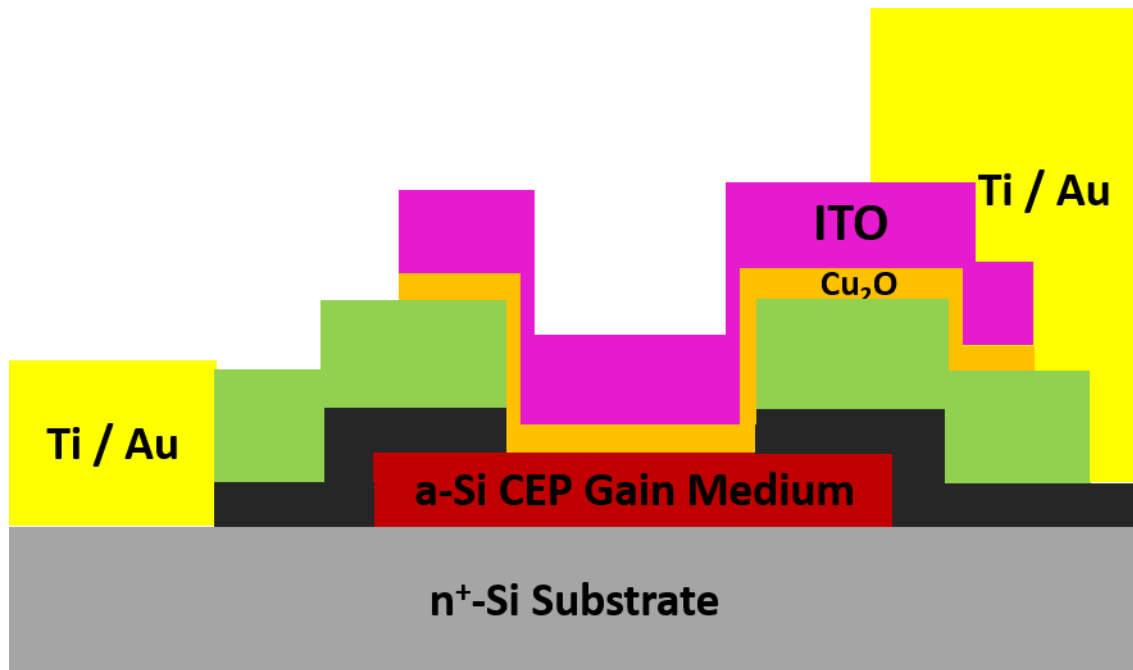
Figure 3.7 Cross-sectional structure of dark current reduction a-Si CEP device.

3.4 Measurement Results

The DC characteristics of dark and photo current are shown in figure 3.8a and b for devices with and without Cu2O respectively. The input optical power is around 10 nW at wavelength of 639 nm. The messages that the measurement results convey are that at reverse

bias 5 V, the dark current is reduced by two orders of magnitude from 100 nA to 1 nA. On the other hand, the photocurrent at all reverse bias voltages are kept at similar levels. Therefore, it supports that the dark current reduction structure design based on band gap engineering works well in terms of reducing dark current without affecting photo response.
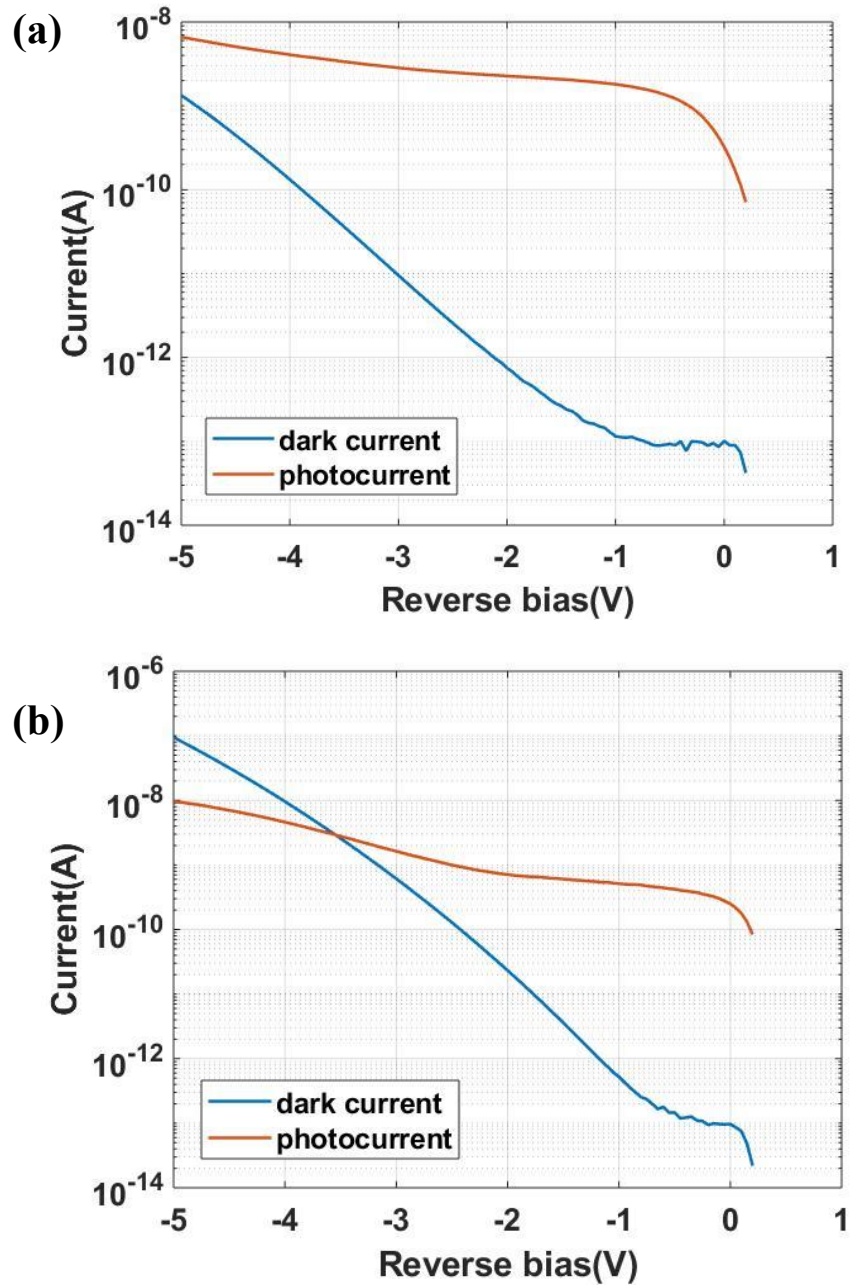
Figure 3.8 DC dark current and photo response characterization for devices (a) With Cu2O electron blocking layer, **(b)** Without Cu2O electron blocking layer.

3.5 Conclusion

We proposed a design to reduce the dark current of carbon-doped a-Si CEP detectors based on the band gap engineering. By characterizing the temperature dependent dark current and fitting the models, we have determined that the dominant source of dark current in the a-Si CEP detectors is the indirect tunneling followed by Poole-Frenkel effect. To block the electron tunneling by increasing the tunneling barrier, Cu_2O, a p-type oxide semiconductor material, was chosen to be deposited by pulsed laser deposition (PLD) between the a-Si layer and top ITO electrode. And the DC characteristics indicated that by adding a thin layer of Cu_2O as electron blocking layer, device dark current was suppressed by two orders of magnitude without influencing the photo response.

Portion of Chapter 3 is unpublished work focusing on dark current reduction methods for amorphous silicon CEP detectors, with the efforts provided by Yu, Y., Zhou, J., Raihan Miah, M.A., Chiu, S.Y., Nomura, K., and Lo, Y.H. The dissertation author is the primary investigator of the project.

Reference

1. Kang, Y., Lo, Y.H., Bitter, M., Kristjansson, S., Pan, Z. and Pauchard, A., 2004. InGaAs-on-Si single photon avalanche Photodetectors. *Applied physics letters*, *85*(10), pp.1668-1670.

2. Yang, B., Li, T., Heng, K., Collins, C., Wang, S., Carrano, J.C., Dupuis, R.D., Campbell, J.C., Schurman, M.J. and Ferguson, I.T., 2000. Low dark current GaN avalanche photodiodes. *IEEE journal of quantum electronics*, *36*(12), pp.1389-1391.

3. Kang, Y., Lu, H.X., Lo, Y.H., Bethune, D.S. and Risk, W.P., 2003. Dark count probability and quantum efficiency of avalanche photodiodes for single-photon detection. *Applied Physics Letters*, *83*(14), pp.2955-2957.

4. Herring, C. and Nichols, M.H., 1949. Thermionic emission. *Reviews of Modern Physics*, *21*(2), p.185.

5. Crowell, C.R., 1965. The Richardson constant for thermionic emission in Schottky barrier diodes. *Solid-State Electronics*, *8*(4), pp.395-399.

6. Fowler, R.H. and Nordheim, L., 1928. Electron emission in intense electric fields. *Proceedings of the Royal Society of London. Series A, Containing Papers of a Mathematical and Physical Character*, *119*(781), pp.173-181..

7. Sze, S.M. and Ng, K.K., 2006. *Physics of semiconductor devices*. John wiley & sons.

8. Frenkel, J., 1938. On pre-breakdown phenomena in insulators and electronic semi-conductors. *Physical Review*, *54*(8), p.647.

9. Rottländer, P., Hehn, M. and Schuhl, A., 2002. Determining the interfacial barrier height and its relation to tunnel magnetoresistance. *Physical Review B*, *65*(5), p.054422.

10. Yang, R.Y., Su, Y.K., Weng, M.H. and Ho, Y.S., 2006. Microstructure and electrical properties of (Zr, Sn) TiO4 thin film deposited on Si (1 0 0) using a sol–gel process. *Applied Surface Science*, *253*(4), pp.2203-2207.

11. Schroeder, H., 2015. Poole-Frenkel-effect as dominating current mechanism in thin oxide films—An illusion?!. *Journal of applied physics*, *117*(21), p.215103.

12. Brassard, D. and El Khakani, M.A., 2003. Dielectric properties of amorphous hydrogenated silicon carbide thin films grown by plasma-enhanced chemical vapor deposition. *Journal of applied physics*, *93*(7), pp.4066-4071.

13. Zhang, L., McMillon, L. and McNatt, J., 2013. Gas-dependent bandgap and electrical conductivity of Cu2O thin films. *Solar energy materials and solar cells*, *108*, pp.230-234.

14. Ishizuka, S., Kato, S., Maruyama, T. and Akimoto, K., 2001. Nitrogen doping into Cu2O thin films deposited by reactive radio-frequency magnetron sputtering. *Japanese Journal of Applied Physics*, *40*(4S), p.2765.

Chapter 4. Plasmonically enhanced photodetector based on a-Si CEP device

4.1 Introduction of Photodetectors on Non-semiconductor Platform and Our Approach

Photodetectors that apply photoelectric effect and convert optical signals to electrical currents play an essential role in the fields of imaging, sensing, and optical communications [1-4]. So far, photodetectors based on inorganic crystalline semiconductors are most prevailing. However, a compatible crystalline semiconductor substrate is required for each material system which is nearly lattice-matched to the active layers of the detectors. The required high quality semiconductor substrate and complicated epitaxial growth of active layers of photodetectors make them expensive to fabricate, costly to scale, and difficult to adapt to new platforms such as glass, ceramic or polymer substrates that become more and more important for the emerging fields of internet of things (IOT), wearable electronics, flexible imaging and display, high frame rate cameras, underwater and free-space optical communications, etc [5-7]. Therefore, fabricating photodetectors on non-semiconductor substrate is desirable.

Organic photodetectors, synthesized via low-cost and process compatible solution-based methods on a non-semiconductor substrate, have been widely studied in this field [8-9]. Although some organic photodetectors show promising results and even better performance than conventional inorganic semiconductor photodetectors [10-11], many organic materials are still suffering from poor stability, especially in the environments with high temperature, moisture, light and moisture [12-13]. Moreover, some organic materials are not compatible with typical photolithography process due to the solvability in solvents such as Acetone and Isopropanol Alcohol (IPA). This property prevents organic devices from being patterned into small feature, which is more favorable for photodetectors. To assure their reliability and performance in such

41

common environments, complicated protection and encapsulation processes are required for organic detectors.

To solve the stability issue, we proposed a structure by simply depositing a thin layer of a-Si on a non-semiconductor substrate to achieve high performance. Amorphous semiconductors such as amorphous silicon (a-Si) are stable with field- proven reliability for optoelectronic applications [14-15]. And from our previous study, a thin layer of a-Si can trigger carrier multiplication and CEP effect which internally amplify the signal. Nonetheless, a key problem for this structure would be the light absorption. Without a semiconductor substrate absorbing light, all the input optical signals can only be absorbed within the thin layer of a-Si and limited electron-hole pairs are generated, preventing the device from achieving decent primary quantum efficiency (QE). Moreover, high defect density in a-Si also leads to low QE due to Shockley-Read-Hall carrier recombination, and its low electron and hole mobility results in very low speed [16].

Our approach to overcome the problem of low external quantum efficiency due to the thin a-Si light absorption layer is to integrate localized surface plasmon resonance (LSPR) effect from Au nanoparticles (NPs) which enhances the light-matter interactions with the internal cycling excitation process (CEP) effect of a-Si. Following this rationale, the device satisfies the two factors, decent OE conversion and signal amplification, to be a high-performance photodetector.

In the following sessions, I will show the device fabrication process, DC characteristics, high-speed measurement results to experimentally demonstrate the device performance. To better understand and explain the effects, COMSOL electromagnetic (EM) field and DC field simulations were done to theoretically elucidate the results.

4.2 Device Design and Fabrication

The device is designed as a undoped thin layer of a-Si sandwiched by two ITO electrodes. A layer of randomly distributed Au NPs (40 nm in diameter) are embedded in the a-Si layer to enhance the EM field and thus facilitating the light absorption of the thin a-Si layer via the LSPR effect [17-18]. The size of Au NPs were chosen based on the localized surface plasmon resonance (LSPR) effect, fabrication process compatibility, and conditions in favor of CEP.

Figure 4.1a shows the cross-sectional structure. The coverage of Au NPs is around 25% measured from SEM image (Fig. 4.1b). The ITO on glass substrate was firstly solvent cleaned and soaked in KOH/isopropanol saturated solution for 2 hours to improve surface smoothness. After cleaning, the substrate was then rinsed with DI water and baked for 30 minutes, followed by spin-coating of a thin layer of HMDS adhesion promotor to improve the adhesion for Au NPs coating. 1 mg/ml aqueous solution of Au NPs with a core diameter of 40 nm and PVP 40 kDa coating (NanoComposix) was diluted to 0.75 mg/mL with IPA and homogenized with 30 s of sonication. Then the 0.75 mg/mL Au NPs mixed solution was deposited on the substrate by drop coating at 55 °C, followed by 2-hour hard baking at 120 °C. After Au NPs coating, a 60 nm thick a-Si with 5% carbon-doped was grown by PECVD, with the substrate temperature of 270 °C. The a-Si film was hydrogen-loaded with H2 plasma. A step of photolithography was done to pattern ITO, which was sputtered and lifted-off to define the top electrode. This ITO layer also worked as self-aligned etching mask for a-Si, which was etched by ICP-RIE system. The ground contact pad was formed with a 200-nm thick sputtered Ti/Au layer on the bottom ITO electrode.
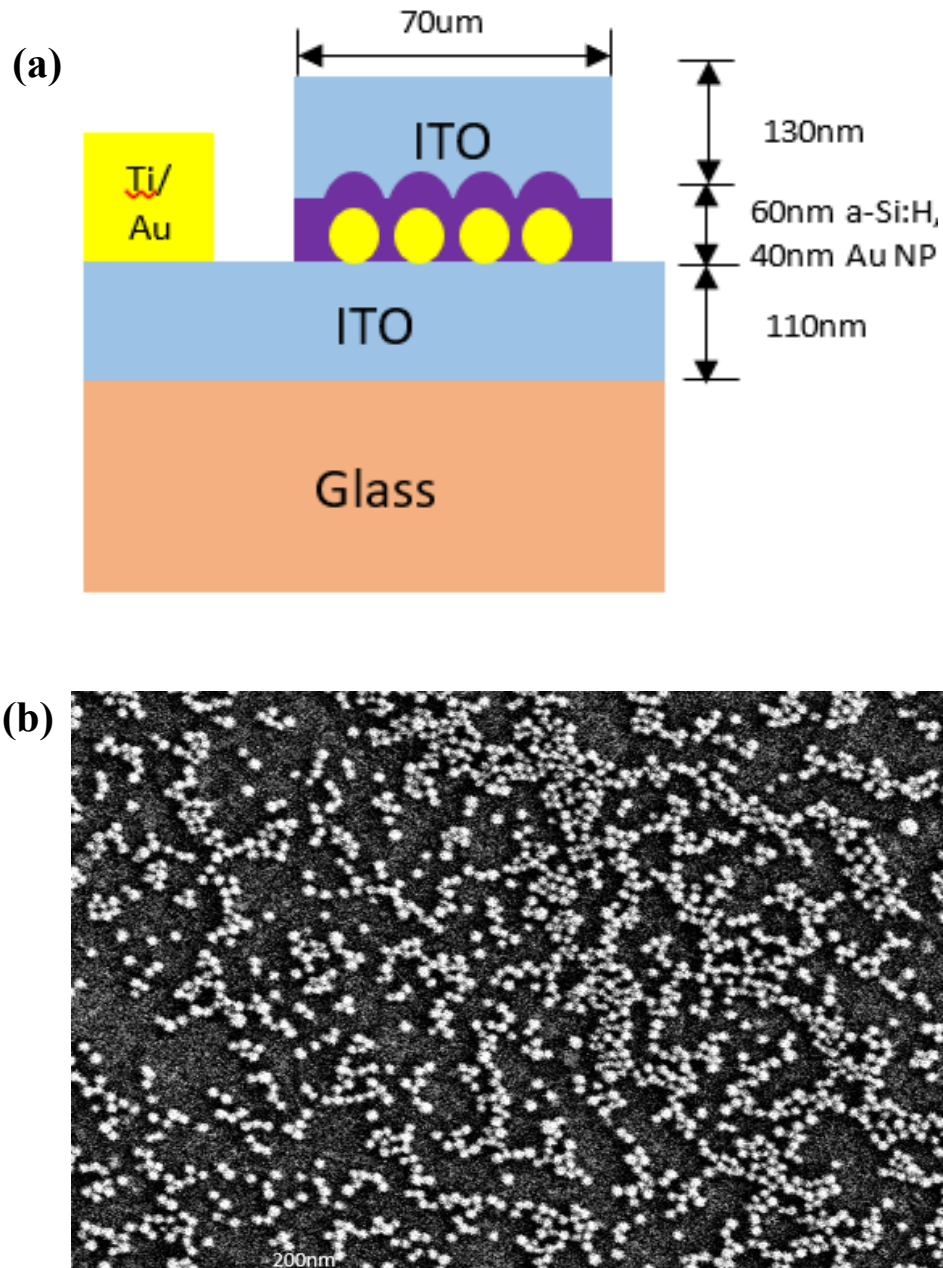
Figure 4.1 Device structure and SEM image. (a) Schematic diagram of device structure with material, function and thickness of each layer, **(b)** SEM image of Au NPs.

4.3 Device DC Characteristics and High-speed Measurement

4.3.1 Enhancement of External Quantum Efficiency (EQE)

The typical dark IV characteristics of a 70 μm diameter device with Au NPs is shown in

figure 4.2. It is nearly a symmetric IV curve because both top and bottom electrodes are ITO, while

the slight difference between forward and reverse bias current is mainly due to the different deposition condition of two ITO electrodes (commercial ITO on glass substrate and sputtered top ITO).

DC photo response was measured at three wavelengths: red (639 nm), green (518 nm) and blue (488 nm), with incident power of 350 pW, 80 pW and 70 pW respectively. Figure 4.3a, b and c summarize the bias dependent EQE for those three wavelengths. The EQE is determined by,

$$EQE = \frac{I_{ph}}{P_{in}} \times \frac{1240}{\lambda(nm)}$$ (4.1)

where I_{ph} is the measured photocurrent, P_{in} is the input power and λ is the measured wavelength.

From the photo response measurement results shown in figure 4.3, at all the three wavelengths, the EQE of devices with Au NPs is appreciably greater than that of the devices without Au NPs, manifesting enhanced light adsorption of a-Si layer due to the LSPR effect. Notably for both devices with and without Au NPs, there are two regimes of EQE increase with voltage bias. From 0 to 1 V, the EQE increases due to the photogenerated carrier drift by increasing electric field instead of being recombined in a-Si. Above 1 V, the electric field across a-Si layer becomes high enough for CEP to take place, and thus the EQE increases due to the CEP amplification mechanism.
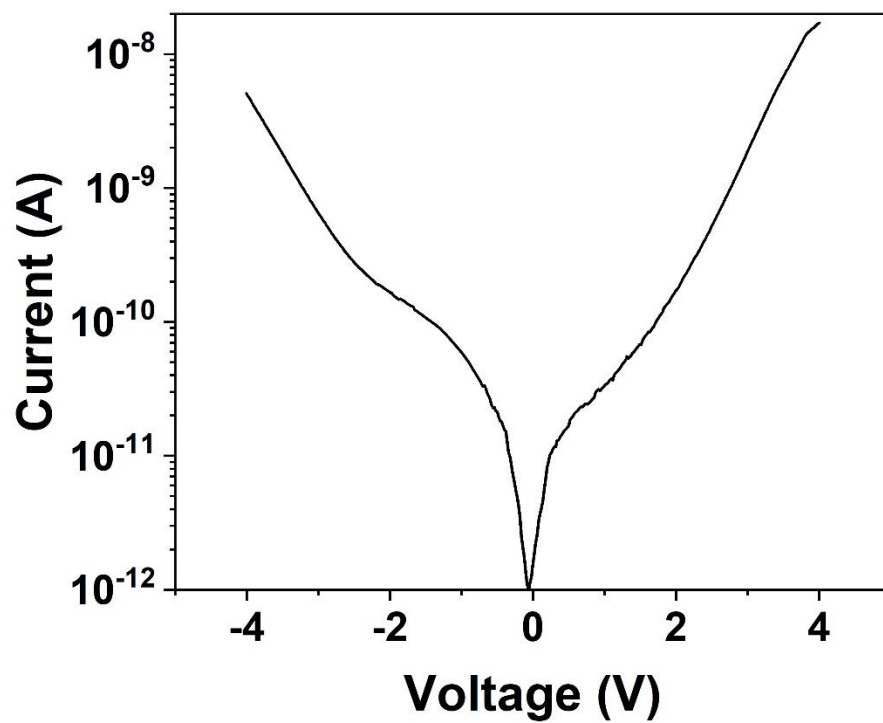
Figure 4.2 IV characteristics of device with Au NPs incorporated.
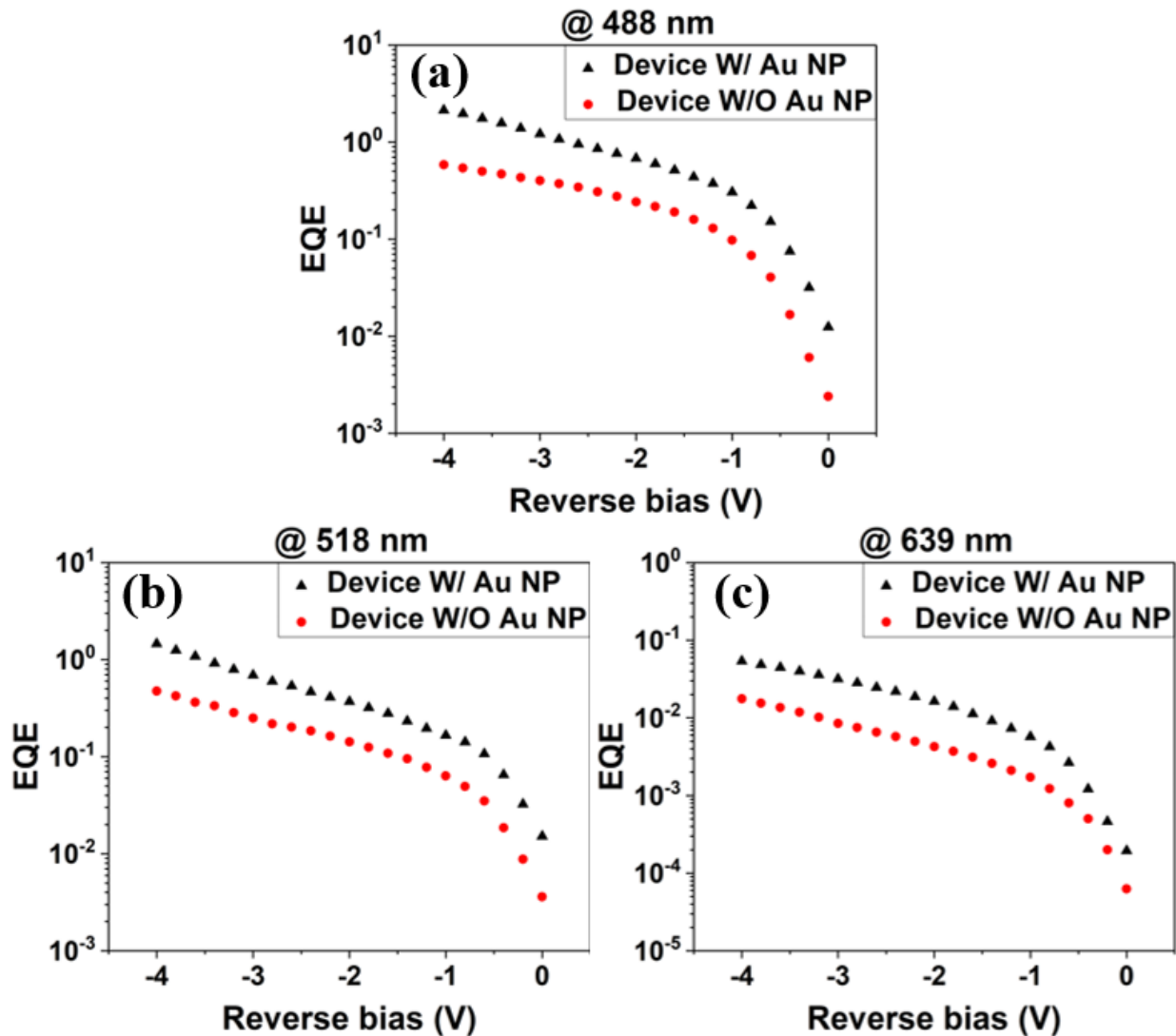
Figure 4.3 EQE under bias (from -4 V to 0 V) at **(a)** 488 nm, **(b)** 518 nm, and **(c)** 639 nm wavelengths. Triangles are for the device with Au NPs and circles are for the device without Au NPs.

4.3.2 High Frequency Characterization

One essential limit for organic or amorphous semiconductor detectors is the low speed performance owing to the very low carrier mobilities. The speed limit hinders these devices from being applied in the high frame rate imaging, which is a key component for the applications such as LIDAR for autonomous vehicle and optical communications.

The high frequency measurement setup is the same as illustrated in figure 2.10. And the input laser was modulated with a small sinusoidal signal at 518 nm, which is the desired

wavelength for underwater communication [19]. Additionally, the device impulse response was measured by using 375 nm and 639 nm wavelength picosecond pulsed lasers (PiLas) which produce 40 ps laser pulses at a 1 MHz repetition rate. The measurement circuit is the same as small-signal modulation AC test, except that the output signal was collected by an Agilent DSO80604B Infiniium High Performance Oscilloscope.

The normalized frequency dependent photo response is shown in figure 4.4a. To investigate the effect of Au NPs on device speed performance, by comparing with device without Au NPs, which has 3 dB cutoff frequency at around 300 MHz, the device with the LSPR effect achieves a much higher bandwidth. Basically, the upper limit of the plot is to 1 GHz, which is limited by the 518 nm diode laser driver, and the actual bandwidth of device with Au NPs can be even greater. If we make conservative assumption that the device bandwidth is 1 GHz, it is already more than 10 times faster than the best reported results of solution-processed organic semiconductor photodetectors [20].

To avoid the limitation of laser driver and focus on the device intrinsic bandwidth, the devices with and without Au NPs were characterized by their impulse responses. Figure 4.4b and c show the device impulse responses at 375 nm and 639 nm respectively. The results of device impulse response are consistent with the result from small signal characterization. And both methods show an obvious increase on the device speed induced by LSPR. At 375 nm wavelength, the rise time of device output signals reduces from 240 ps to 85 ps by adding Au NPs. Similarly, at 639 nm wavelength, the device rise time was reduced from 330 ps to 75 ps due to the incorporation of Au NPs. Considering the pulse width (full width at half maxium, FWHM), devices with with Au NPs achieve a FWHM of around 170 ps (FWHM) at both wavelengths, while the a-Si devices without Au NPs have a FWHM of 540 ps at 375 nm wavelength and 600 ps at 639 nm

wavelength. This is a record among all high-speed detectors made of amorphous or disordered materials [21-22].
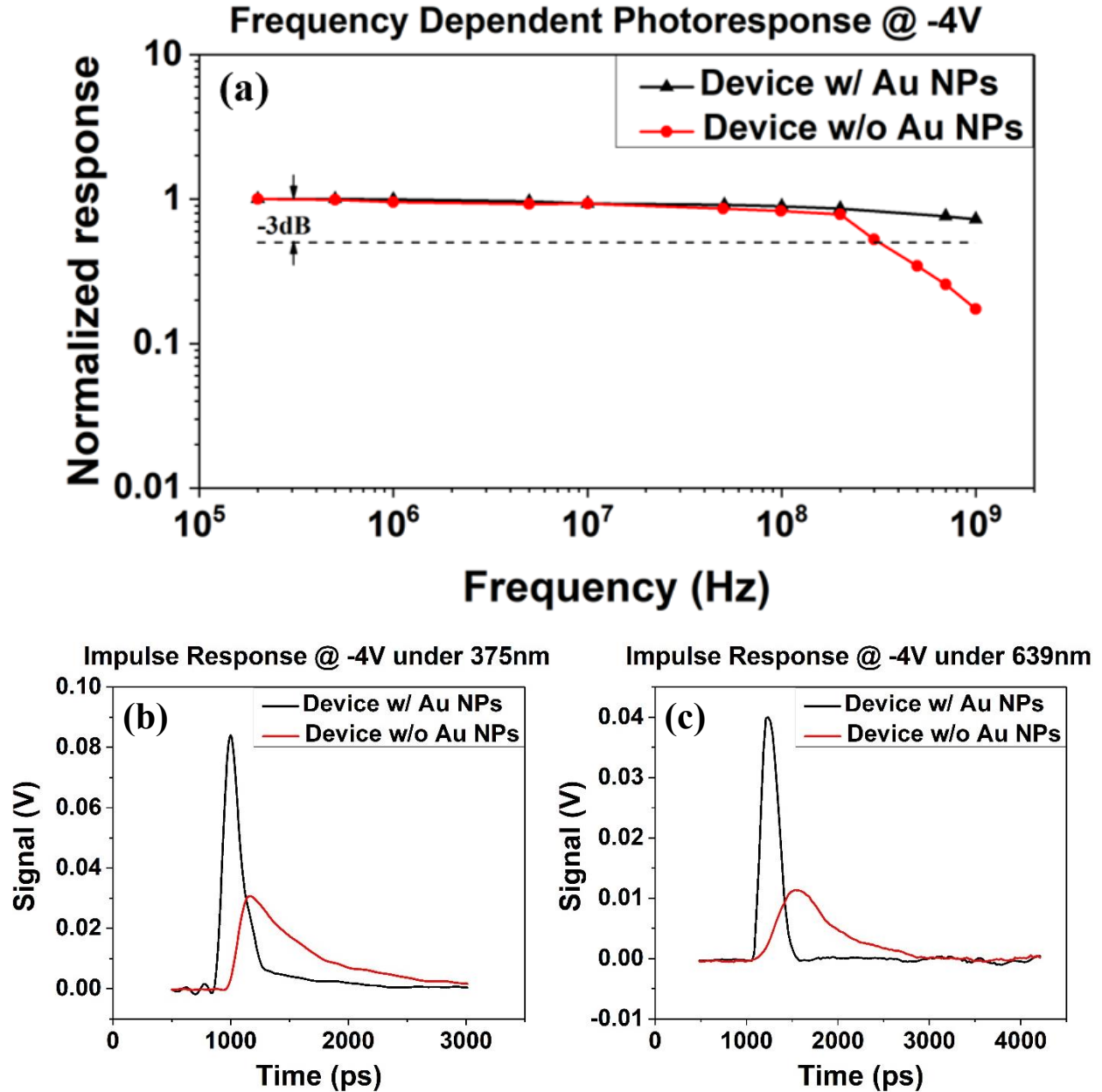
Figure 4.4 High speed measurement results. (a) Frequency response of 518 nm for devices with and without Au NPs under -4 V, from 200 kHz to 1 GHz, **(b)** Impulse response to 40 ps laser pulses at 375 nm wavelength and1 MHz repetition rate, **(c)** Impulse response to 40 ps laser pulses at 639 nm wavelength and1 MHz repetition rate.

4.4 COMSOL Simulation Results of Electromagnetic Field and DC Field

4.4.1 Electromagnetic Field Simulation Result

The real and imaginary parts of the refractive index, $n(\lambda)$ and $k(\lambda)$, for 5% carbon-doped a-Si was measured by Filmetrics. And the light absorption at different wavelengths was calculated based on the simulated electromagnetic field distribution by using COMSOL Multiphysics 4.3 for devices with and without Au NPs. The absorption coefficient, $\alpha(\lambda)$, can be calculated from the imaginary part of the wave vector, $k(\lambda)$, $\alpha(\lambda) = \frac{4\pi k(\lambda)}{\lambda}$ under the assumption that the layer thickness is much smaller than the wavelength and the amount of light absorption is linearly proportional to the input intensity. By integrating over the a-Si layer, we have,

$$\int_V dI(\vec{r}) = \int_V \alpha I(x,y,z)dxdydz \tag{4.2}$$

where x and y directions define the plane normal to the incident light. The quantum efficiency, η, is calculated by the adsorbed light power $\int_V dI(\vec{r})$ divided by the input power P_o as below,

$$\eta(\lambda) = \int_V dI(\vec{r})/P_o = \frac{n(\lambda)\alpha(\lambda)}{AE_o^2} \int_V |E(\vec{r})|^2 dxdydz \tag{4.3}$$

where A is the area of the detector, λ is the wavelength in vacuum, E_0 and E are the incident and total electric field correspondingly.

To make sure the consistency between the simulation and experiment, in these EM simulations, the periodicity of a single calculation cell is 70 nm along both the x and y directions, and the thickness of each layer is consistent with the actual device geometry shown in figure 4.1a. There is one Au NP with a diameter of 40 nm inside the calculation cell, so that the resultant fill factor (~25%) agrees with that of the measured result taken from SEM images, shown in figure 4.1b. The 3-D schematic of the a-Si active layer in the EM simulation is illustrated in figure 4.5a.

The simulated EM fields at wavelengths of 488 nm, 518 nm and 639 nm are shown in figure 4.5b, c and d respectively. The EM fields in the a-Si active layer is mostly concentrated at the surface of Au NP, resulting from LSPR. Therefore, the absorption efficiency inside the a-Si layer is enhanced.
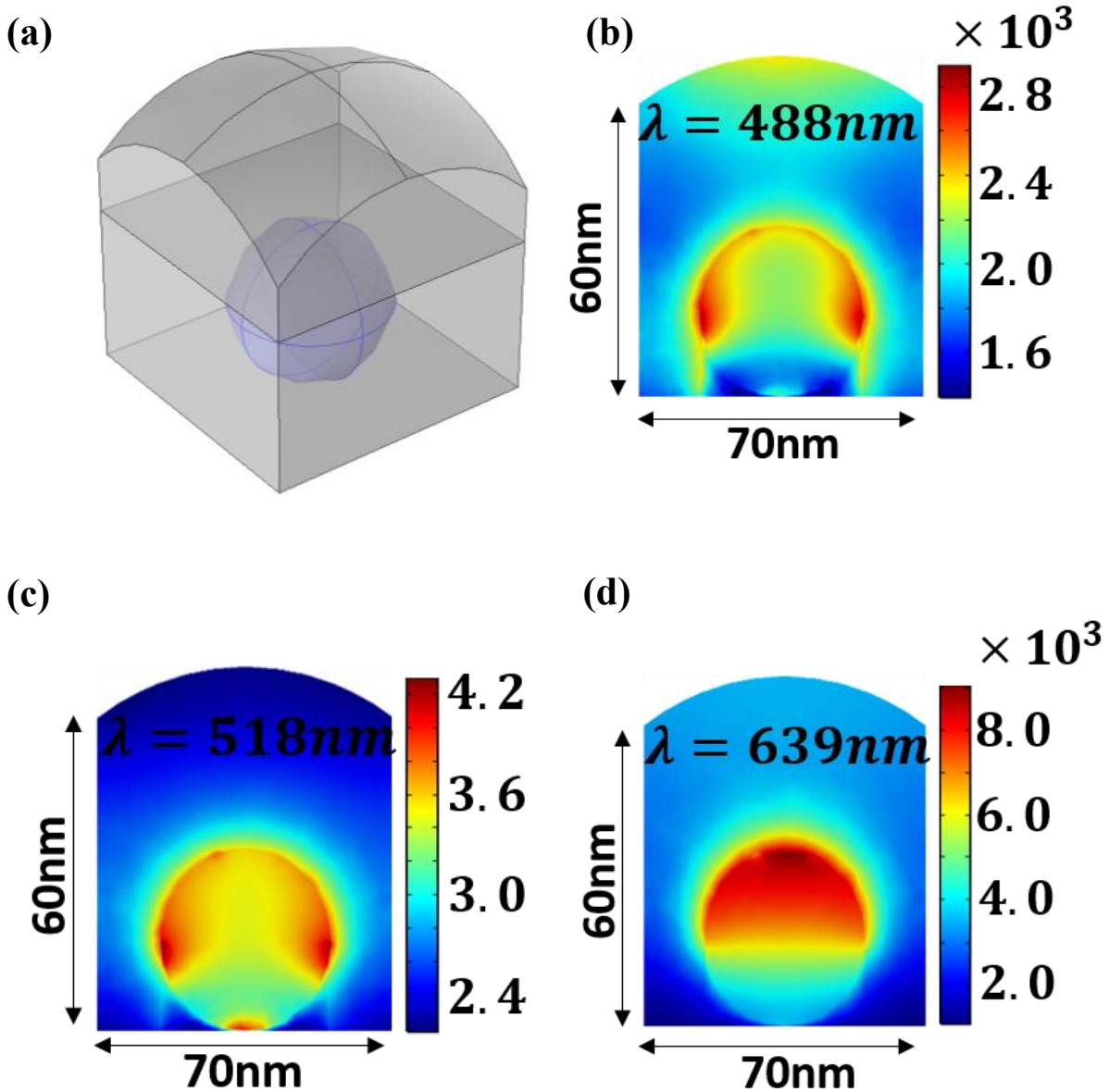
Figure 4.5 3D EM simulation results of electric field in the a-Si active layer. (a) 3d structure of the a-Si layer with an Au NP, (b) simulated electric field under 488 nm, (c) 518 nm, (d) 639 nm.

To quantify the increasing absorption efficiency, we can use equation 4.3 to calculate the quantum efficiency from light absorption at different wavelengths. The results are shown in figure 4.6a. By taking the QE ratio of devices with and without Au NPs, we are able to obtain the QE enhancement factor by LSPR effect at different wavelengths, shown in figure 4.6b. The improved absorption efficiency factor by LSPR effect ranges from 1.6 to 3.8 at wavelengths from 450 nm to 700 nm. Consistent with the experimental data in figure 4.3, where the device with Au NPs under -2 V bias exhibits an improved EQE by factors of 2.62 at 488 nm, 2.51 at 518 nm, and 4.72 at 639 nm, respectively, the simulated results are strong support for device EQE enhancement due to LSPR.
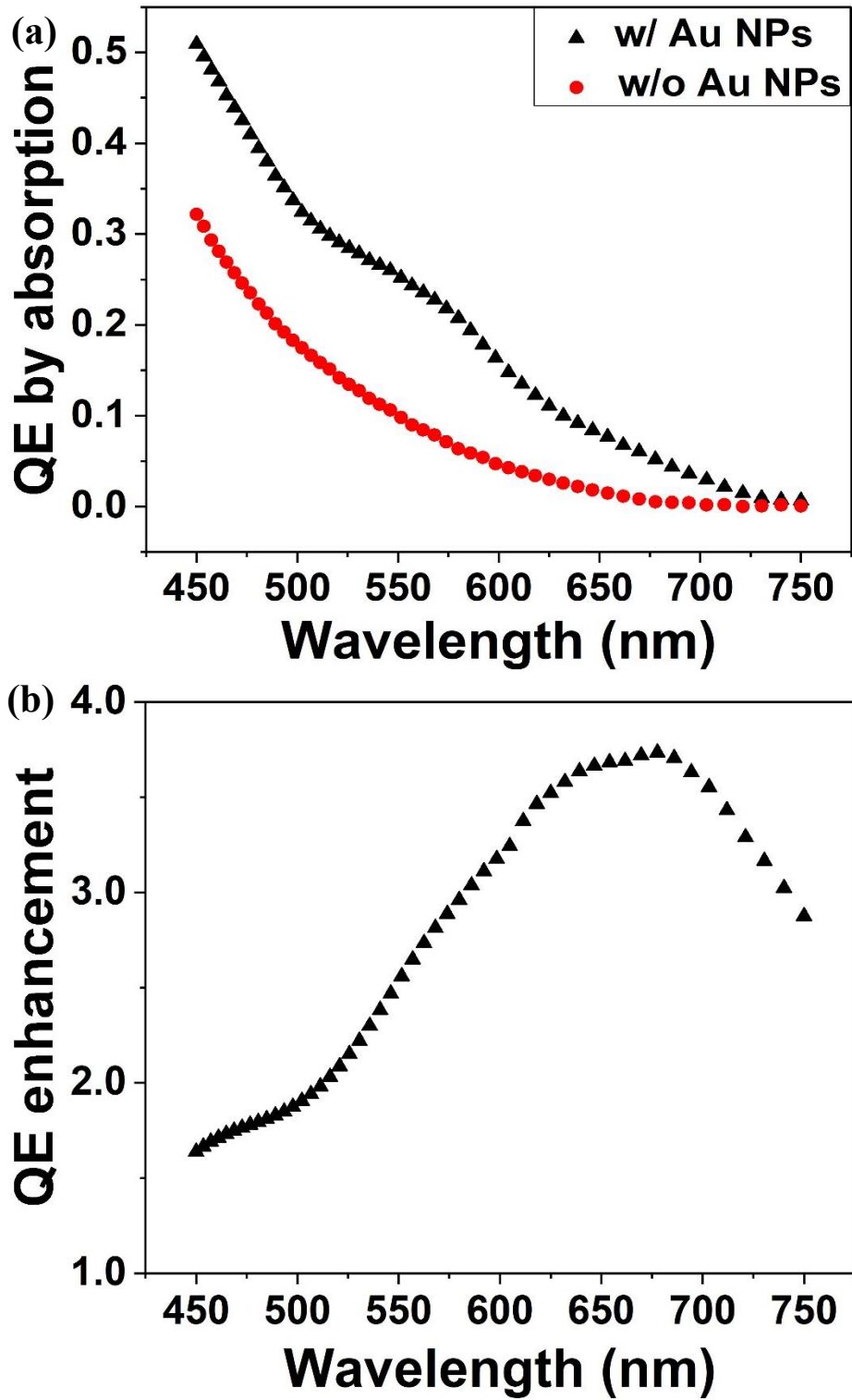
Figure 4.6 Quantum efficiency enhancement by LSPR effect. (**a**) wavelength dependent absorption with and without Au NP, (**b**) QE enhancement factor induced by Au NP.

4.4.2 DC Field Simulation Result

Besides the EM fields near the surfaces of Au NPs are enhanced due to LSPR, the DC electric field under voltage bias is also expected to increase in regions near the Au NPs, leading to a good match between the region where light absorption efficiency increases due to high EM field and the region with high DC electric field which drive the photogenerated carriers faster and thus reduce the carrier transit time. To illustrate the effect, the distribution of DC electric field was simulated and shown in figure 4.7. For device without Au NP, the DC E-field in the a-Si active layer is uniformly distributed, while when there is Au NP embedded, the electric field near the upper half of the particle is much greater. Even in areas near the upper contact and farthest from the Au NP, the E-field exhibits a comparable value to the device without Au NPs. The DC electric field simulation serves as a strong support for the device speed improvement by adding Au NPs, which was demonstrated experimentally in section 4.3.2.
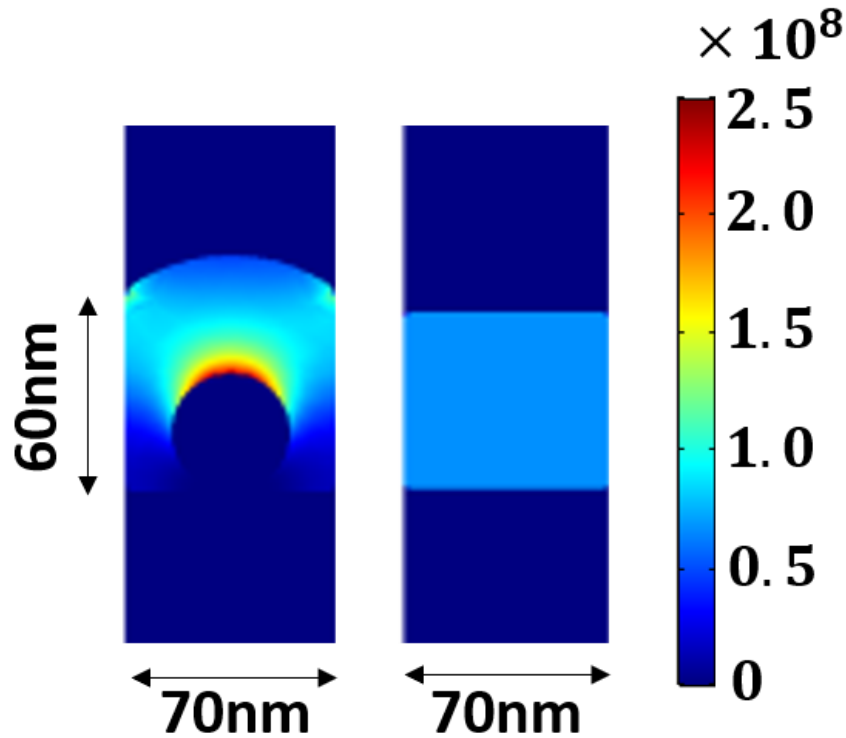
Figure 4.7 DC electric field simulation in the a-Si active layer for device with Au NPs and device without Au NPs.

4.5 Conclusion

We proposed a structure with simply a thin layer of a-Si sandwiched by ITO electrodes. To achieve a decent light absorption within the thin a-Si active layer and thus high performance, we integrated LSPR effect with CEP internal amplification mechanism by embedding Au NPs into the a-Si layer. Experimentally and theoretically, we successfully demonstrated that significant enhancement of the external quantum efficiency, detectivity, and frequency response of photodetectors has been achieved in the plasmonically enhanced a-Si based device. Our device shows superior performance in terms of photo responsivity and speed under low optical power and have low dark current, suitable for communications and imaging applications. Unlike semiconductor detectors that require high quality, single crystal, rigid substrates and expensive epitaxial growth, amorphous Si thin film detectors can be deposited on various substrates and fabricated in a simple, low cost, and highly scalable process to support emerging applications such as IoT, wearable electronics, flexible displays, autonomous vehicles, and more.

Portion of Chapter 4 has been published in the following publication: Yu, Y., Xu, Z., Li, S., Zhang, A.C., Yan, L., Liu, Z. and Lo, Y.H., 2019. Plasmonically Enhanced Amorphous Silicon Photodetector with Internal Gain. IEEE Photonics Technology Letters, 31(12), pp.959-962. The dissertation author is the primary investigator/first author of the paper.

Reference

1. Donati, S., 2001. Photodetectors: devices, circuits, and applications.

2. Yotter, R.A. and Wilson, D.M., 2003. A review of photodetectors for sensing light-emitting reporters in biological systems. *IEEE Sensors Journal*, *3*(3), pp.288-303.

3. Potter, R.F. and Eisenman, W.L., 1962. Infrared photodetectors: a review of operational detectors. *Applied Optics*, *1*(5), pp.567-574.

4. Rogalski, A. and Razeghi, M., 1996. Semiconductor ultraviolet photodetectors. *Opto-Electronics Review*, *1996*(1-2), pp.13-30.

5. Ashton, K., 2009. That 'internet of things' thing. *RFID journal*, *22*(7), pp.97-114.

6. Stoppa, M. and Chiolerio, A., 2014. Wearable electronics and smart textiles: a critical review. *sensors*, *14*(7), pp.11957-11992.

7. Hanson, F. and Radic, S., 2008. High bandwidth underwater optical communication. *Applied optics*, *47*(2), pp.277-283.

8. Gong, X., Tong, M., Xia, Y., Cai, W., Moon, J.S., Cao, Y., Yu, G., Shieh, C.L., Nilsson, B. and Heeger, A.J., 2009. High-detectivity polymer photodetectors with spectral response from 300 nm to 1450 nm. *Science*, *325*(5948), pp.1665-1667.

9. Yao, Y., Liang, Y., Shrotriya, V., Xiao, S., Yu, L. and Yang, Y., 2007. Plastic near-infrared photodetectors utilizing low band gap polymer. *Advanced Materials*, *19*(22), pp.3979-3983.

10. Ahmadi, M., Wu, T. and Hu, B., 2017. A review on organic–inorganic halide perovskite photodetectors: device engineering and fundamental physics. *Advanced Materials*, *29*(41), p.1605242.

11. Tian, W., Zhou, H. and Li, L., 2017. Hybrid organic–inorganic perovskite photodetectors. *Small*, *13*(41), p.1702107.

12. Asghar, M.I., Zhang, J., Wang, H. and Lund, P.D., 2017. Device stability of perovskite solar cells–A review. *Renewable and Sustainable Energy Reviews*, *77*, pp.131-146.

13. Thomas, S., Ly, J., Zhang, L., Briseno, A.L. and Bredas, J.L., 2016. Improving the stability of organic semiconductors: Distortion energy versus aromaticity in substituted bistetracene. *Chemistry of Materials*, *28*(23), pp.8504-8512.

14. Carlson, D.E. and Wronski, C.R., 1976. Amorphous silicon solar cell. *Applied Physics Letters*, *28*(11), pp.671-673.

15. Cocorullo, G., Della Corte, F.G., De Rosa, R., Rendina, I., Rubino, A. and Terzini, E., 1998. Amorphous silicon-based guided-wave passive and active devices for silicon integrated optoelectronics. *IEEE Journal of selected topics in quantum electronics*, *4*(6), pp.997-1002.

16. Sakata, I. and Hayashi, Y., 1985. Theoretical analysis of trapping and recombination of photogenerated carriers in amorphous silicon solar cells. *Applied Physics A*, *37*(3), pp.153-164.

17. Link, S. and El-Sayed, M.A., 2003. Optical properties and ultrafast dynamics of metallic nanocrystals. *Annual review of physical chemistry*, *54*(1), pp.331-366.

18. Mulvaney, P., 1996. Surface plasmon spectroscopy of nanosized metal particles. *Langmuir*, *12*(3), pp.788-800.

19. Schill, F., Zimmer, U.R. and Trumpf, J., 2004, December. Visible spectrum optical communication and distance sensing for underwater applications. In *Proceedings of ACRA* (Vol. 2004, pp. 1-8).

20. Shen, L., Fang, Y., Wang, D., Bai, Y., Deng, Y., Wang, M., Lu, Y. and Huang, J., 2016. A Self-Powered, Sub-nanosecond-Response Solution-Processed Hybrid Perovskite Photodetector for Time-Resolved Photoluminescence-Lifetime Detection. *Advanced Materials*, *28*(48), pp.10794-10800.

21. Auston, D.H., Lavallard, P., Sol, N. and Kaplan, D., 1980. An amorphous silicon photodetector for picosecond pulses. *Applied Physics Letters*, *36*(1), pp.66-68.

22. Salamin, Y., Ma, P., Baeuerle, B., Emboras, A., Fedoryshyn, Y., Heni, W., Cheng, B., Josten, A. and Leuthold, J., 2018. 100 GHz plasmonic photodetector. *ACS photonics*, *5*(8), pp.3291-3297.

Chapter 5. Light detection in organometallic perovskite based photodetector

5.1 Introduction of Organometallic Perovskite

Perovskite structures, with the general formula, ABO3, become one of the most important and commercially exploited family of solids. A subset of them is the hybrid perovskites, containing both organic and inorganic components, where A site is composed of an organic cation within a post transition metal halide framework. It started to emerge from 2009 as simple, low cost solar cell materials, competitive with silicon in terms of power conversion efficiencies [1-7]. And halide perovskites have been showing great promise in device applications owing to their remarkable electronic and optoelectronic properties [8-10]. The ABX_3 perovskite-type structure, illustrated in figure 5.1, is comprised of an extended framework of corner-sharing PbI_6 octahedra with the methylammonium cation ($CH_3NH_3^+$) occupying the central A site and surrounded by 12 nearest-neighbor iodide ions. Techniques to process perovskites can be varied. Spray coating, a nozzle is used to disperse tiny liquid droplets onto substrates, and the perovskite layer can also be deposited by ultrasonic spraying [11]. Dip coating, a nonconventional method to create the meniscus edge, is pulling a substrate out of a precursor ink and sheering a cover plate over the deposition substrate [12]. Two-step deposition, separates the formation of perovskite by depositing a thin film of halide lead first, which will react with organic halide salts to form perovskite [12-13]. Chemical vapor deposition (CVD) has been used to deposit FAPbI3 thin film [14].
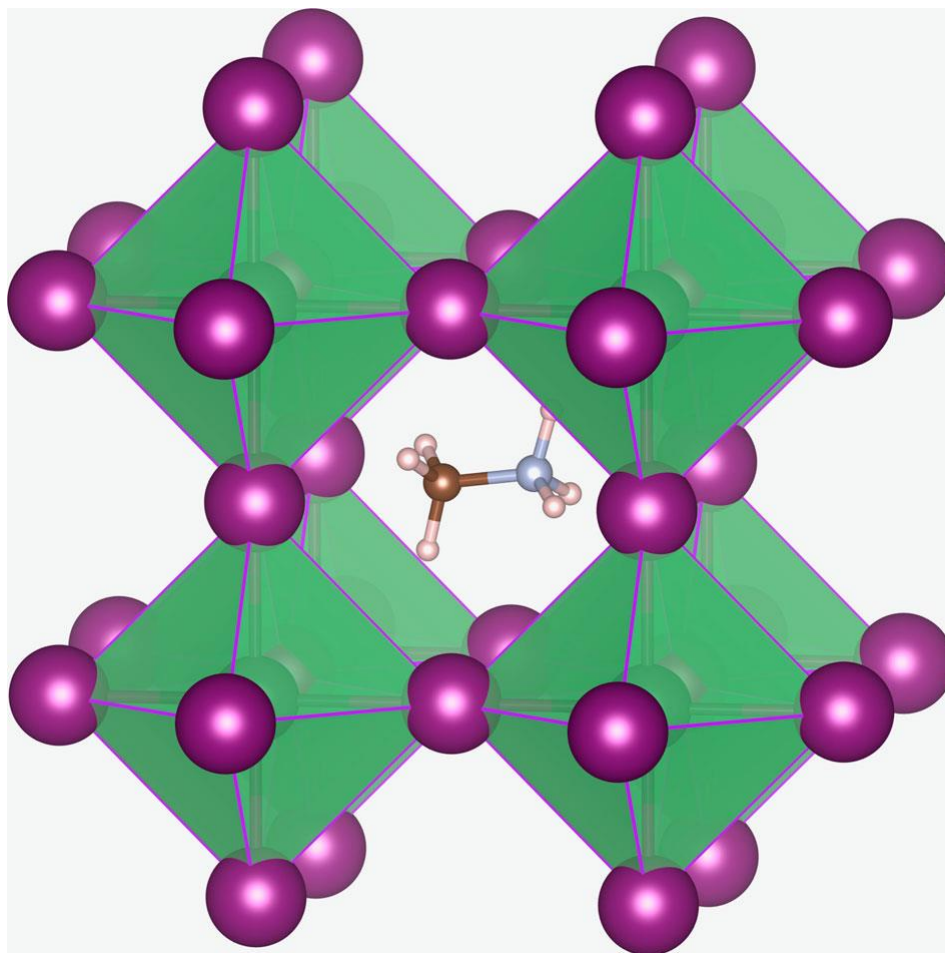
Figure 5.1 Perovskite structure of CH3NH3PbI3. Methylammonium cation ($CH_3NH_3^+$) occupies the central A site surrounded by 12 nearest-neighbor iodide ions in corner-sharing PbI_6 octahedra. [15]

One general observation raised by people is that for all perovskite detectors, its photo responsivity is very sensitive to the input light intensity. And the responsivity decreases monotonically with increasing light intensity. By searching the literatures, we found that there have been no systematic studies on power and frequency dependent photo response for perovskite based detectors. Most studies show an extremely high responsivity under DC measurements, without pointing out how it would change with frequency [16-17]. While some other groups reported high frequency response without specifying the power level and corresponding responsivity at high frequency [18-20]. Therefore, we strongly believe that a comprehensive study

on how photo responsivity of perovskite photodetectors behaves under different frequency and input optical power level is essential to understand the true physics of photoelectric process in organometallic halide perovskite.

5.2 Device Design and Fabrication

It is more favorable for photodetector device to have small feature size. However, organometallic perovskite is not compatible with typical photolithography process because it becomes degraded immediately when rinsed with solvents and DI water. Therefore, patterning became a great challenge in device fabrication. Our solution to solve this issue was to use Poly-TPD, an organic material mostly serves as hole transport layer, to work as photoresist and pattern perovskite [21]. Poly-TPD is a kind of organic material that is stable in solvents while it can be dissolved in chlorobenzene (CB). In the contrast, organometallic perovskite is stable in CB. Following this rationale, we can pattern Poly-TPD at first and pattern perovskite on top of Poly-TPD afterwards.

Figure 5.2 shows the process flow of device fabrication. For the solution preparation, we dissolved poly-TPD (40 mg) in 2mL Chlorobenzene (CB) in N_2 glovebox to get the 20 mg/mL solution. $CH_3NH_3PbI_3$ was prepared by mixing CH_3NH_3I (795 mg) and PbI_2 (2.3 g, 1:1 molar ratio) into DMF (2648 µl) and DMSO (323 µL) mixed solvents. All the solutions were magnetically stirred at 60 ℃ and 1200 rpm for more than 12 hours.

We chose typical ITO on glass substrate for bottom electrode, which was solvent cleaned and soaking in KOH/isopropanol saturated solution, followed by a baking at 120 ℃ for 30 minutes as mentioned in section 4.2 (Fig. 5.2a). To isolate the device active region, the ITO substrate was wet etched by 50%-HCl with negative photoresist (NR9-1500) as etching mask (Fig. 5.2b, c). The 20 mg/mL Poly-TPD solution was spin-coated with 600 rpm for 45 seconds, followed by 150 ℃

post bake for 30 minutes (Fig. 5.2d). Because Poly-TPD is compatible with typical

photolithography, we patterned the coated Poly-TPD layer with NR9-1500 photoresist and used

O2 plasma to dry etch the layer (Fig. 5.2e, f). The photoresist was then removed by acetone. The

perovskite solution was spin-coated onto the patterned substrate with 3500 rpm for 40 second. At

the 10th second during spin-coating, 1 mL Ether was sprayed on the substrate, facilitating the

formation of $CH_3NH_3PbI_3$ crystal. Then the sample was baked at 70 ºC for 15 minutes. As a result,

a layer of 400 nm thick perovskite layer was formed on top of patterned Poly-TPD (Fig. 5.2g). The

top ITO electrode with the thickness of 150 nm was sputtered in DC sputtering system (Fig. 5.2h).

Due to the solubility difference between Poly-TPD and $CH_3NH_3PbI_3$ in CB, we can lift off the

device in CB and eventually obtained small-featured perovskite photodetector devices with

diameter down to 7 µm (Fig. 5.2i).
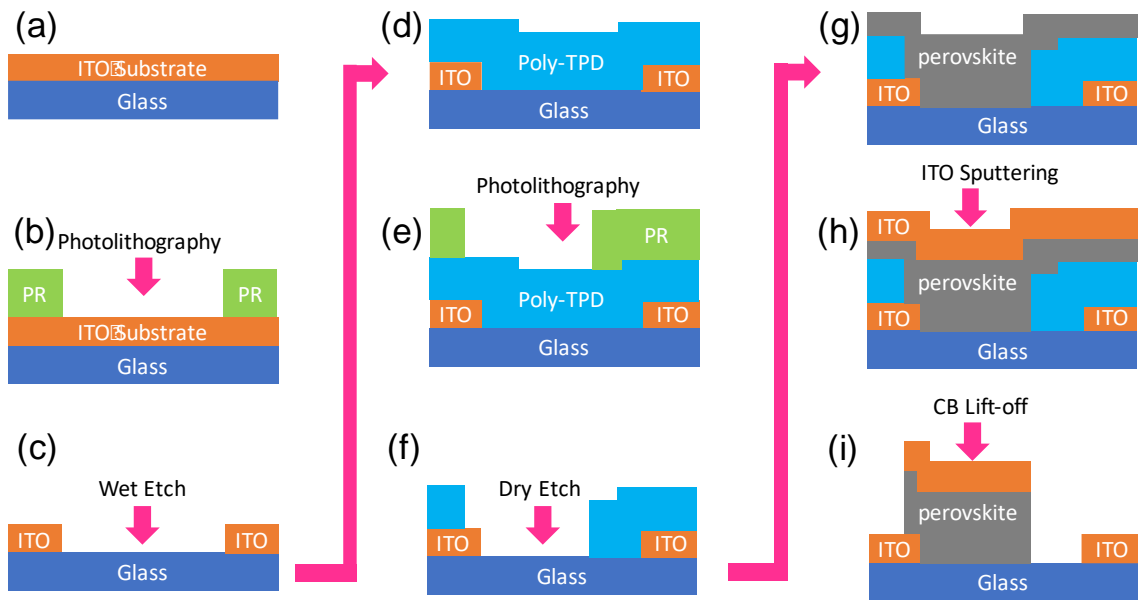
Figure 5.2 Fabrication process. (a) Cleaned ITO glass substrate with Cr/Au alignment markers. Cr/Au alignment markers are in the center and 4 corners of a substrate, not shown in the device region. **(b)** Photolithography for wet etch mask. **(c)** Wet-etching of ITO. **(d)** Spin-coating of poly-TPD. **(e)** Photolithography for dry etch mask. **(f)** Dry-etching of poly-TPD. **(g)** Spin-coating of perovskite and post bake. **(h)** ITO sputtering. **(i)** Lift-off in CB.

The device 3-D and top-view schematic structure are shown in figure 5.3a. Figure 5.3b illustrates the device IV characteristics, which is asymmetric mostly due to the different growth conditions of top and bottom ITO electrodes. The real device top-view microscopic image is shown in the inset figure of figure 5.3b, contacted with a ground-signal-ground (GSG) probe.
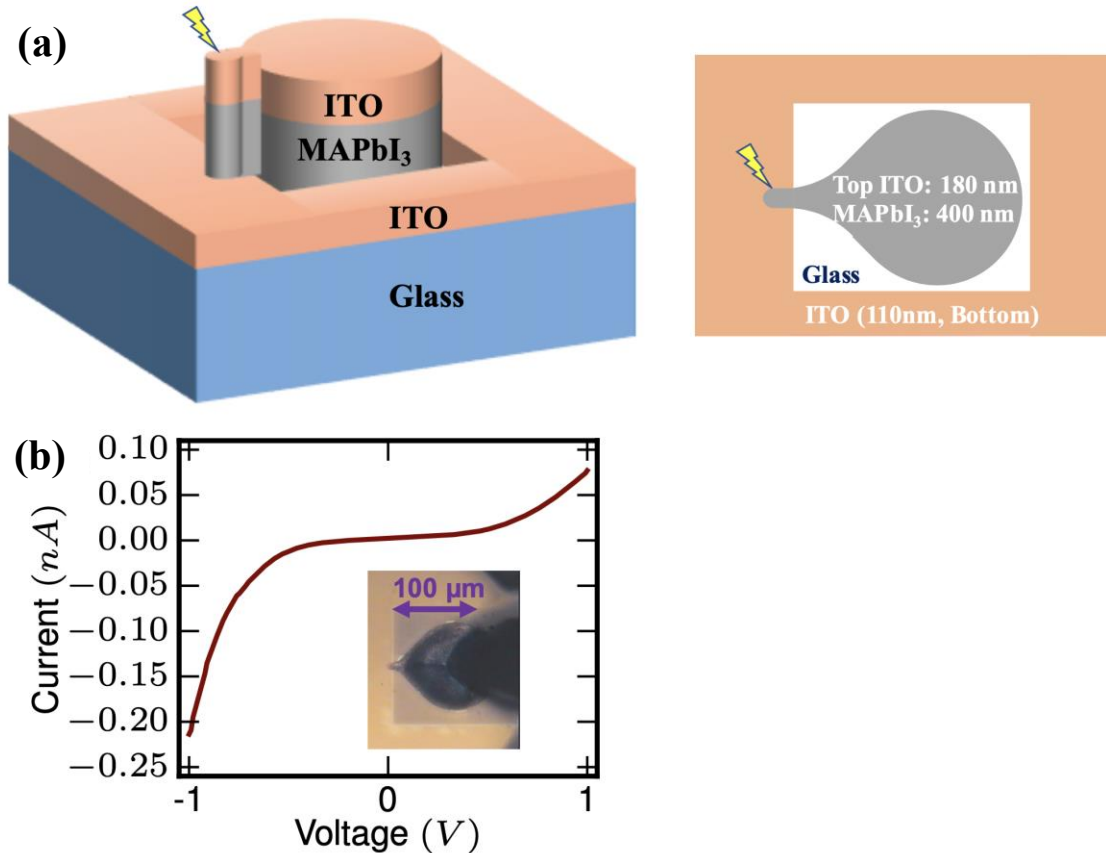
Figure 5.3 Device layout and dark IV (a) Schematic diagram of device structure with material and thickness of each layer (3D and top view), **(b)** Dark IV Characteristics and the micrograph of a probed device.

5.3 High-speed Photo Response Characterization

The frequency dependent measurement setup is similar as what discussed in section 2.6 and section 4.3.2. The device was reverse biased at 1V and contacted with a high speed GSG probe. The measured frequency range was from 5 Hz to 800 MHz. Because there is no single equipment

in our lab can cover the whole spectrum of this 10 decades range of frequency, we have measured the response using two instruments: a lock-in amplifier from 5 Hz ~ 10 kHz with a transimpedance amplifier SR570 and a spectrum analyzer with low-noise amplifier from 500 kHz to 800 MHz range.

Figure 5.4a shows the device frequency response from 5 Hz to 800 MHz at 4.5 µW sinusoidally modulated optical input absorbed (639 nm wavelength). The discontinuity between 10^4 to 10^6 is due to the change of instruments. Apparently, the photoresponsivity was nearly independent of frequency within the measurement errors and gave rise to the value of around 10^{-3} A/W under 4.5 µW. Under different power, the perovskite detector devices tend to behave differently in terms of photo responsivity. To further investigate the device power dependent photo response, we measured the device responsivity from 18 pW to 5 µW under different frequencies of 10 Hz, 0.5 MHz, 5 MHz and 51 MHz. Figure 5.4b shows the log-log plot of responsivity, of which all the curves show slopes around -0.4. From literatures, we have found some similar relation was reported with power dependent responsivity slopes between -0.4 to -0.5, which is related to the defect states density in perovskite [22-23].
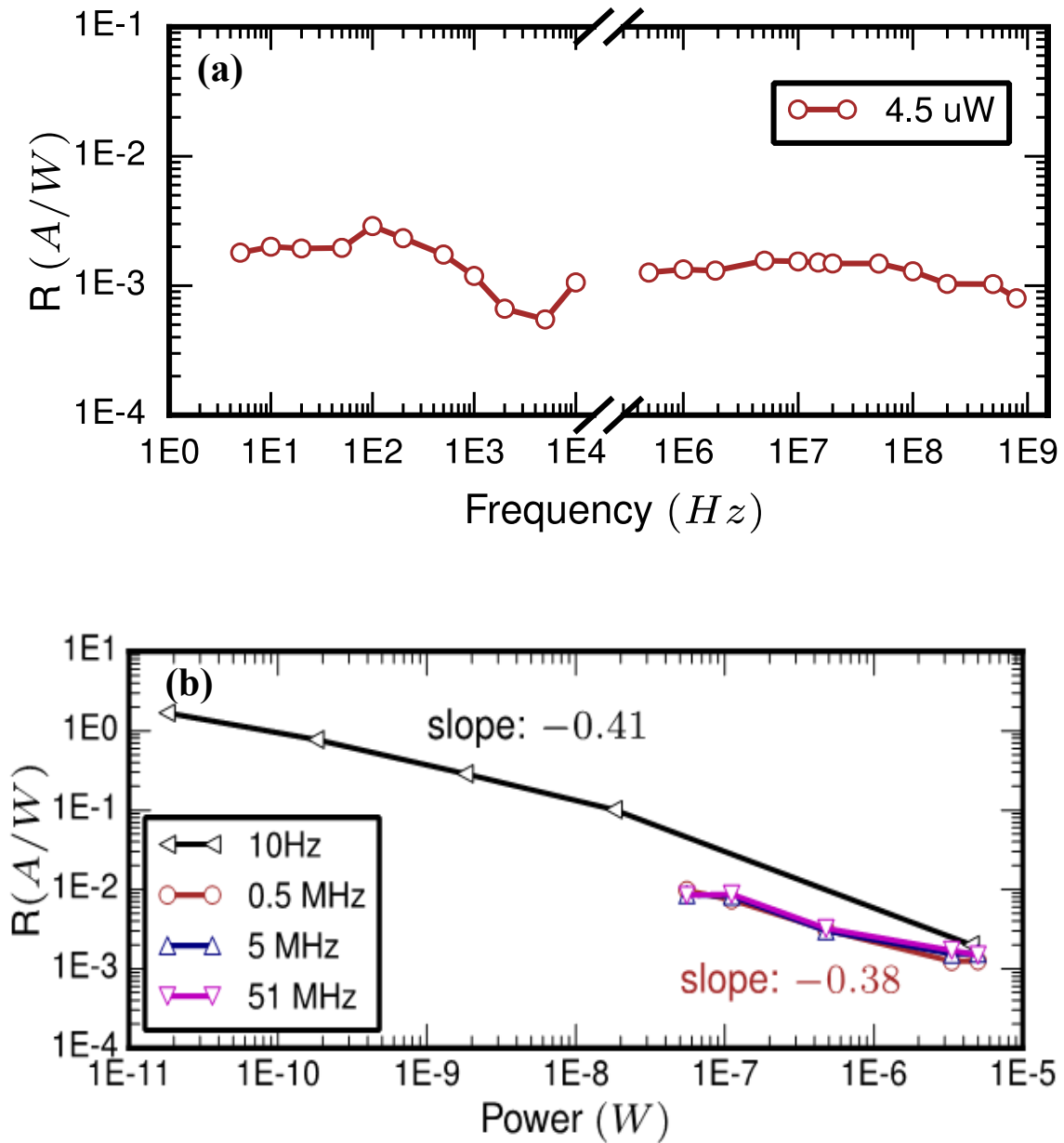
Figure 5.4 Frequency and power dependent photo response. (a) Frequency response from 5 Hz to 800 MHz with 4.5 µW 639 nm input, **(b)** Power dependent response (639 nm) under 10Hz, 0.5MHz, 5MHz and 51 MHz.

5.4 Quasi-persistent Photo Response Characterization

To better understand the perovskite device behavior, we characterized the device slow response by recording how device performed during a time period of tens of seconds. In the slow response characterization, the laser was modulated by an Agilent 33600A series waveform

generator to generate a rectangular pulse with pulse width of 200 ms. To record the device response to a single 200 ms optical pulse at a given power level, we programmed a LabVIEW file to simultaneously control the bias on device and the generation of optical pulse. Initially, the device bias was ramped from 0 V to reverse bias 1 V at a rate of 0.2 V/s. After the bias reached to 1 V, the waveform generator generated a single rectangular pulse with pulse width of 200 ms at the 10th second and the data collection started to record the time dependent current change of device. Surprisingly, we found the device current rose after 10-20 s of laser hitting the device, until the current reached to a constant level. The output current remained at the level in a manner of persistent photocurrent triggered by the 200 ms optical pulse (Fig. 5.5). The good stability of the dark current allows us to precisely measure the persistent photocurrent as small as 30 pA, which is well above the sensitivity limit (10 fA) of the instrument. After the measurement, the LabVIEW program reset the device by reducing the bias voltage to 0 V. As a result, the device current level dropped to zero in less than 140 s.

Figure 5.5 Slow (quasi-persistent) photo response of the device triggered by a single 200 ms rectangular optical pulse containing different number of photons.
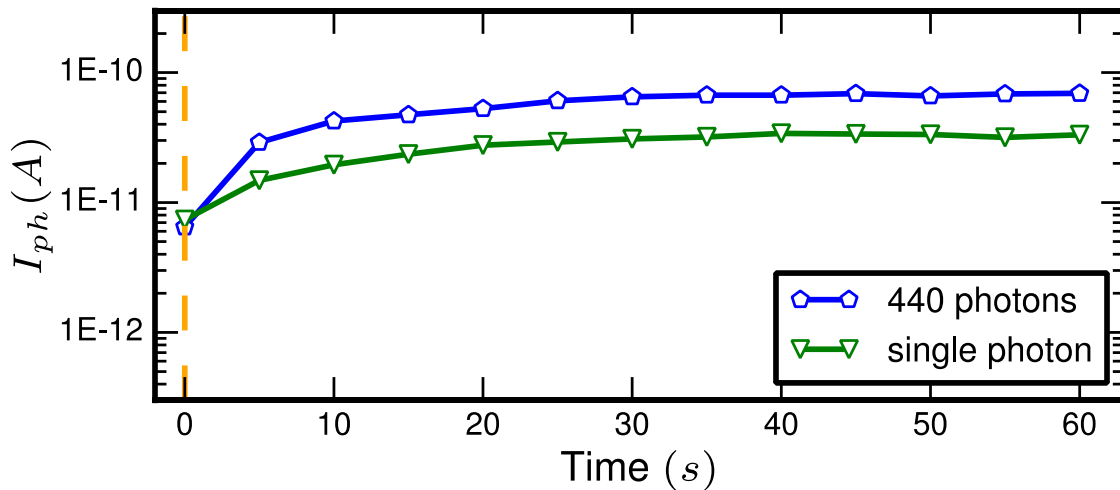
5.4.1 Absorbed Optical Power Calibration

We prepared 4 different structures, ITO/ glass (substrate), ITO/ ITO/ glass, perovskite/ ITO/ glass, and ITO/ perovskite/ ITO/ glass, to calibrate the power and the amount of light absorbed only by perovskite layer. Reflectivity was measured by Filmetrics profilometer. The percentage of transmitted light at different wavelengths was measured using commercial detector. The fraction of light absorbed by the perovskite layer in the ITO/ perovskite/ ITO /glass structure was measured and calculated to be 0.75 at 518 nm wavelength and 0.68 at 639 nm wavelength.

By input a rectangular pulse, the number of photons, $N_{ph,PV}$, absorbed by perovskite layer can be simply calculated from the optical power by,

$$P_{ph,PV} = \gamma \frac{P_{in}}{E_\lambda} \qquad\qquad (5.1-a)$$

$$N_{ph,PV} = \gamma \frac{P_{in}T}{E_\lambda} \qquad\qquad (5.1-b)$$

where T is the laser pulse width (200 ms in our case), P_{in} is the input optical power, and E_λ is the energy of a single photon of wavelength λ.

5.4.2 Power Dependent Responsivity Measurement

As discussed above, the slow response photocurrent is obtained by subtracting the device saturated current level after illumination of 200 ms optical pulse by the initial dark current. The photo responsivity is then obtained by taking the ratio of the photocurrent and the absorbed optical power by perovskite layer, which is also called effective responsivity (A/W) as the reflection and transmission are calibrated. The log-log plot of power versus effective responsivity under 639 nm is shown in figure 5.6, with the absorbed power ranging from 14 aW to 6.9 fW. The slope of the curve (-0.89) is quite different from ones in figure 5.4b (-0.4), indicating a different photodetection mechanism for slow response, which will be discussed in the following sections. Moreover, a slope

close to -1 represents that with the increasing power, the change of device photocurrent is hardly anything.
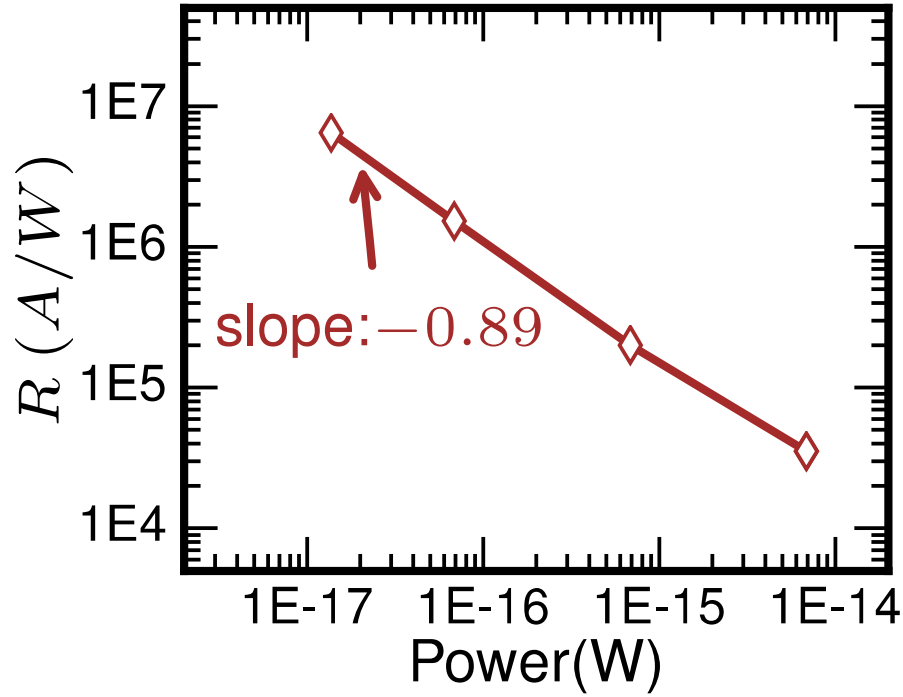
Figure 5.6 Power dependent quasi-persistent photo response at 639 nm.

5.4.3 Single Photon Measurement

The slow (quasi-persistent) photo response of perovskite photodetector devices can respond to an input power down to single photon level. From the previous discussion, we can control the number of photons absorbed by the perovskite layer by adjusting the input power levels. Tests of the single photon response were performed at wavelengths of 518 nm. Considering $\lambda = 518\ nm$, a single photon carrying energy of 2.39 eV (0.38 aJoule) corresponds to a peak power level of 1.9 aW for a 200 ms rectangular optical pulse. Figure 5.7a shows the plot of device effective responsivity versus different absorbed photon numbers. There are two regimes indicated in the plot. From 1 to 10 photons, correspondingly from 2 aW to 20 aW, the effective responsivity remains a constant level, which means that the output photocurrent of the perovskite detector is

linearly proportional to the number of photons absorbed by the perovskite layer. The second regime, where the number of photons absorbed is higher than 10, shows a similar trend as figure 5.6, indicating that the number of photons absorbed by perovskite layer is saturated and the output photocurrent hardly increases with more photons absorbed.

To better illustrate the single photon detection ability of perovskite detector, we performed 40 trials of single photon response measurement for one device to see the statistics. After each measurement, we set the device without any external bias voltage nor input light for 140 s, and the current recovered to the original level. Hence, the next trial can be performed. Figure 5.7b shows the results of those 40 trials of single photon measurements with an average of 0.98 photon absorbed by the layer. It shows that by absorbing a single photon, the device current is increased by 20-30 pA on average.
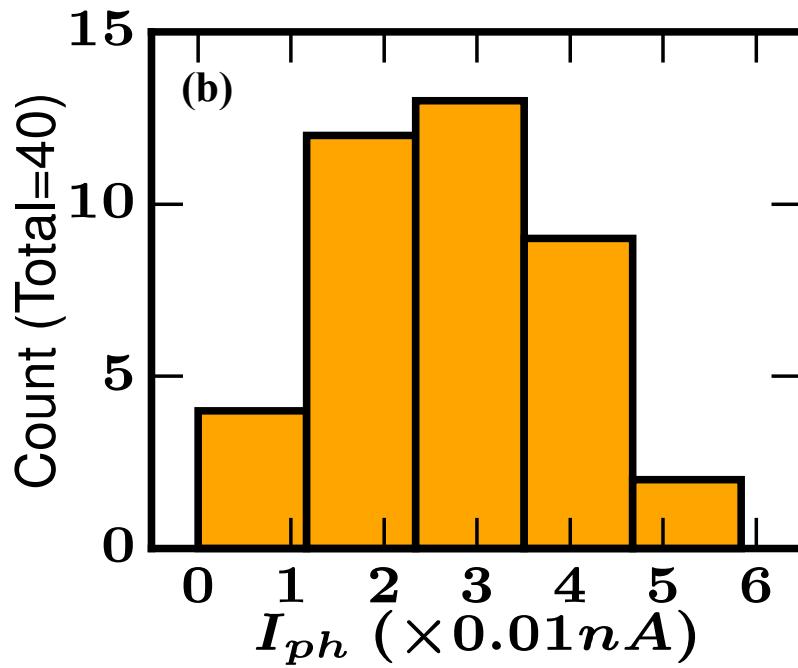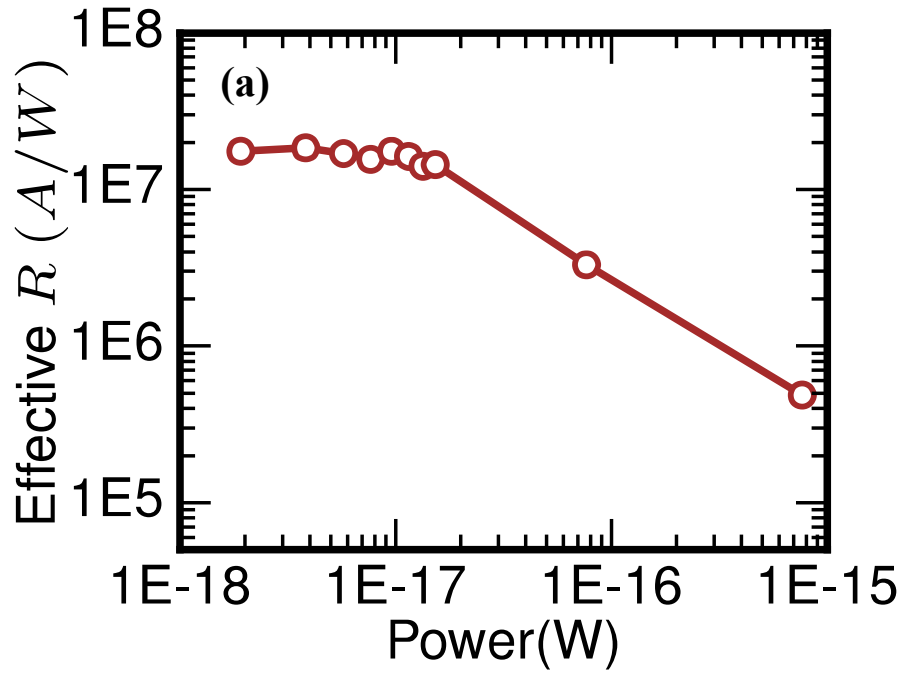
Figure 5.7 (a) Average power-dependent quasi-persistent photoresponse (518 nm), **(b)** Statistical distribution of photocurrent with absorption of a single 518 nm wavelength photon. (Average Photon number: 0.98).

5.5 Proposed Mechanism to Explain the Quasi-persistent Photo Response

From the quasi-persistent photo response results discussed in section 5.4, we learnt that there must be an internal amplification mechanism to achieve the single photon detection in the perovskite photodetector. We proposed that the device conductivity changes result from the accumulation of charged ions and vacancies which lead to band bending, due to single photon absorption under bias, as shown in Figure 5.8a. More specifically, the mechanism, ionic impact ionization (I3), elucidates observations of macroscopic property changes by absorption of a single photon, as shown in Figure 5.8b. This process triggered by an absorbed photon can be represented by a series of equations (5.2.), where the process in equation (5.2.c) (i.e. I3 process) is cascaded and the rate grows exponentially,

$$V_I^+/I_i^- \xrightarrow{h\nu} V_I^+/I_i^- + e^-/h^+ \rightarrow V_I^+/I_i^- + m\hbar\Omega \tag{5.2.a}$$

$$V_I^+/I_i^- + m\hbar\Omega \rightarrow V_I^+ + I_i^- \tag{5.2.b}$$

$$I_i^- + V_I^+/I_i^- \xrightarrow{E-field} V_I^+ + 2\,I_i^- \tag{5.2.c}$$

Upon a photon with energy of $h\nu$ is absorbed in perovskite layer, an electron-hole pair is generated across the band gap or a mid-gap state. Before drifting to the electrodes, the e^-/h^+ pair recombines non-radiatively and transfers energy to lattices, resulting in phonon generations with energy of $m\hbar\Omega$ (eq. 5.2.a). Those phonons carry sufficient vibrational energy to ionize the V^+/I^- Frenkel pair and produce mobile V^+ and I^- (eq. 5.2.b) [24-26]. Then the mobile V^+ and I^- are split by the applied electric field. The proposed I3 process is described in equation (5.1.c). The Coulomb interaction between the travelling I- and the V_I^+/I_i^- Frenkel pair can break the Frenkel pair into mobile V_I^+ and I_i^-. As a result, the number of mobile I_i^- increases exponentially in an avalanche-like process as the I_i^-s move towards the anode.
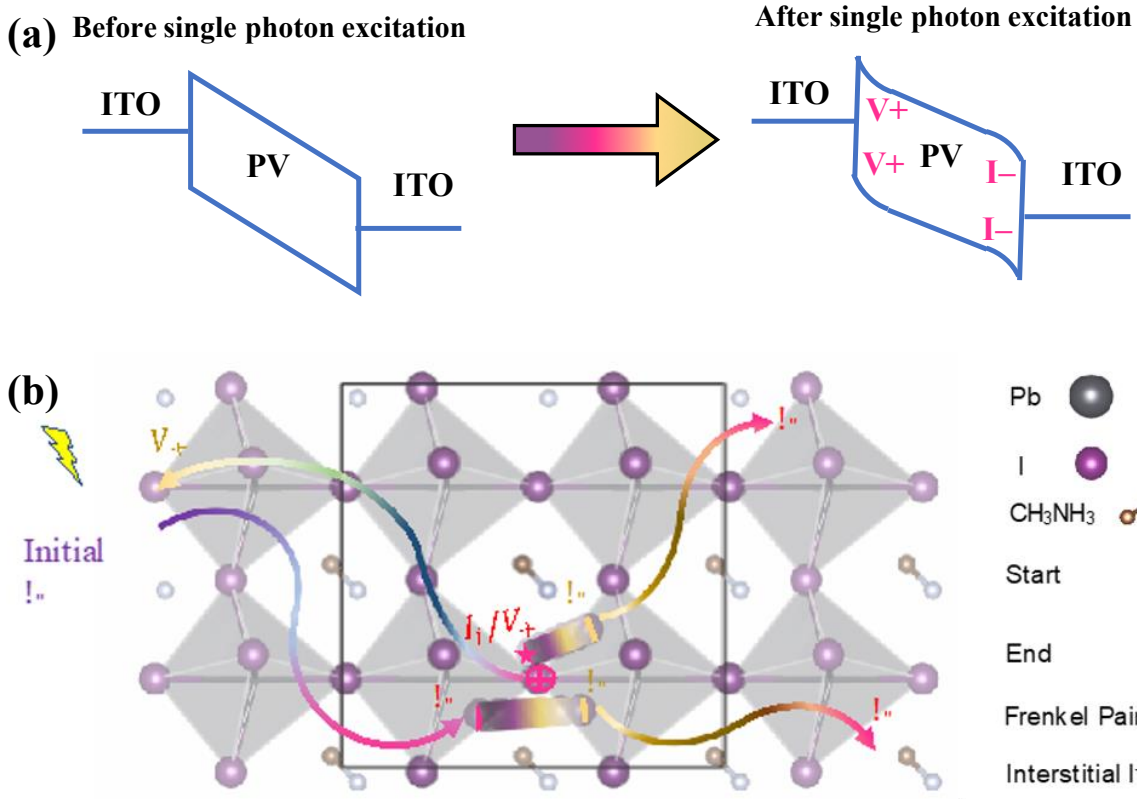
Figure 5.8 Proposed mechanism to explain the quasi-persistent photo response. (a) Band-bending under bias due to accumulation of changed ions after photons absorption, **(b)** Schematic of ionic impact ionization (I3) process.

After the ions and vacancies accumulating at the interface of ITO/perovskite, the electrical conductivity change can be modeled by Poisson's equation and thermionic emission model in equation (5.3)

$$J_T = AT^2 \exp\left(-\frac{q\varphi_B}{kT}\right)\left(\exp\left(\frac{qV}{kT}\right) - 1\right) \tag{5.3}$$

where A = Richardson coefficient, T = 300 K, φ_B = Schottky barrier height, V = applied bias, q = electron charge, and k = Boltzmann Constant. Taking the ratio between the current before and after illumination, we can obtain the Schottky barrier height change $\Delta\varphi_B$ in equation (5.4),

$$\frac{I_{ph}+I_d}{I_d} = \exp\left[-\frac{q}{kT}\Delta\varphi_B\right] \tag{5.4}$$

Using the relation: $\Delta\varphi_B = \varphi_B - \varphi_{Bo} = -\sqrt{qE/4\pi\varepsilon_0\varepsilon_r}$ \hfill (5.5)

where E = electric field, ε_0 = permittivity of free space, ε_r= dielectric constant of perovskite), it is straightforward for us to derive the relation between the electric field at the perovskite/ITO interface and the measured currents, as shown in equation (5.6),

$$E = 4\pi\varepsilon_0\varepsilon_r[\ln{(\frac{I_{ph}+I_d}{I_d})}\frac{kT}{q^{3/2}}]^2$$

(5.6)

Eventually, the number of ions accumulated can be modeled by applying Gauss's Law: $\varepsilon_0\varepsilon_r(E - E_o) = qN_I$ where N_I is the surface density (#/m^2) of accumulated iodides and V$^+$'s near the ITO/perovskite interfaces and E_o is the field in the charge neutral region. Therefore, for each absorbed photon number, we can calculate the number of ions and vacancies triggered by I3 and accumulated from the photocurrent level.

5.6 Reversibility Study for Quasi-persistent Photo Response

A functional detector requires the ability to operate repeatedly. If we couldn't reset the device to original state, the device has no access to any applications even if it can detect single photon level. A study of reversibility of the quasi-persistent photo response was done. Changing the device conductivity due to the accumulation of ions and vacancies, the I3 process is reversible in the sense that the accumulated iodides near the anode can return to the original distribution. We have studied two reset conditions: setting the bias to 0 V and reversing the bias from -1V to 1V. The first condition relies on iodide diffusion in dark due to the concentration difference and the second condition uses an opposite field to accelerate the motion of iodide. As shown in Figure 5.9, under zero bias, the device needs 140 seconds to have its dark current return to its original value, while under the second condition, the device dark current is reset in 70 seconds.
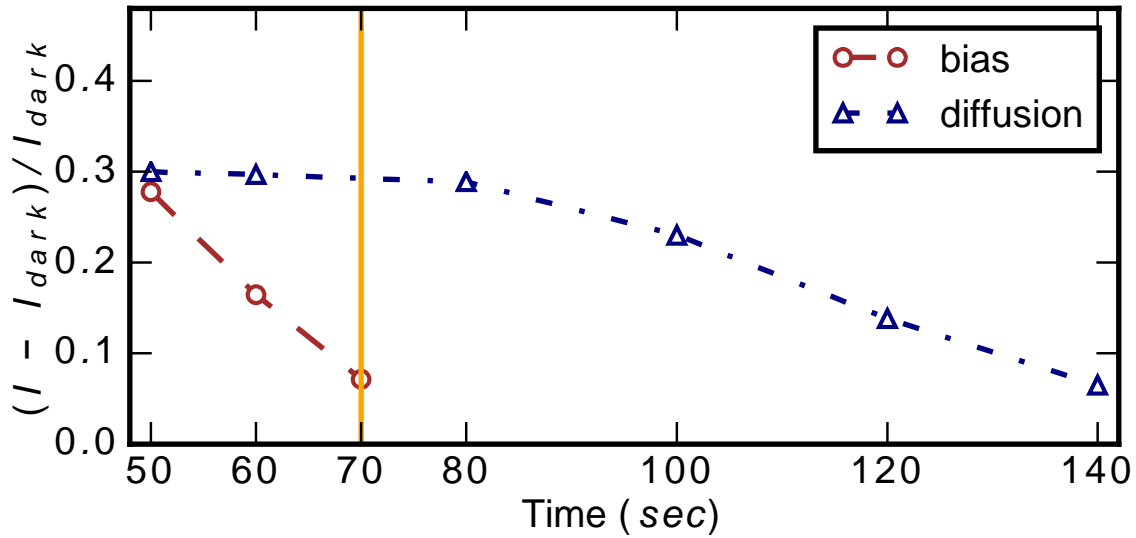
Figure 5.9 Reversibility of perovskite detector with drift under electric field or with diffusion only in the dark.

Another way to support the reversibility is to measure the reflectivity spectrum of the device. Device macroscopic property change under optical excitation and external bias can be measured by optical spectrum analyzer as the ion accumulation change the composition distribution at the device surface and affects the reflectivity before and after optical illumination under bias and after resetting the bias to 0 V [27-28]. Figure 5.10 clearly shows that the reflective spectrum changes due to the ion migration. Initially the reflective spectrum has a peak wavelength at around 647 nm, which shifted to 630 nm after the illumination and external bias. After setting the device at 0 V without any light for 2 minutes, the peak shifted back to 645 nm, indicating that the perovskite layer recovered to the original state by ion diffusion.
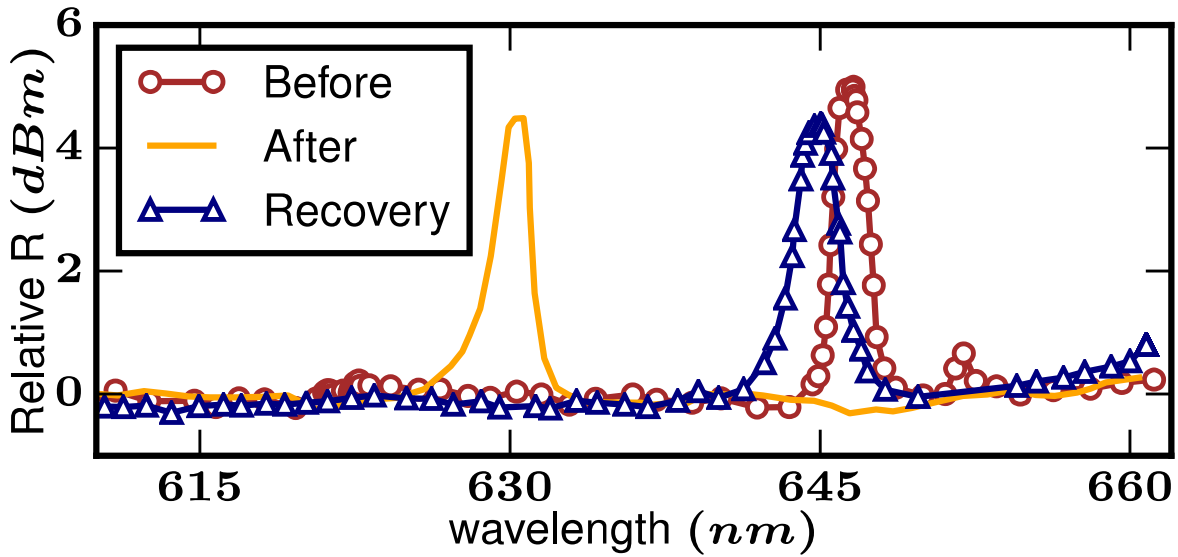
Figure 5.10 Relative reflective spectrum of perovskite detector. Brown circle line is reflectivity upon the device area before illumination; Orange star line is reflectivity after illumination with applied bias; Navy triangle line is reflectivity two minutes after bias was turned off.

5.7 Conclusion

We demonstrated a novel fabrication method to pattern small-featured perovskite photodetector device. It involves the spin-coating of another organic material, Poly-TPD, which is compatible with the typical photolithography process while is dissolvable in chlorobenzene (CB). Following this rationale, we fabricated perovskite device with diameter of 7 µm.

In a 7 µm perovskite device, we characterized the frequency and optical power dependent photo response. The results show that there are two different photo response mechanisms that contribute to the two different power dependent responsivities: the first one is the same mechanism as conventional photodetectors which involves the absorption of photons and electron-hole pairs generations; the other one is quasi-persistent and sensitive to very low input optical power down to single photon level.

The first type of photo response was measured from 5 Hz to 800 MHz under 4.5 µW at 639 nm, with a responsivity of 10^{-3} A/W along all the frequencies. And the log-log power dependent plot shows a decreasing trend of responsivity with increasing power, of which the slope is ~ -0.4. By carefully measuring the photo response of perovskite device down to the single photon level, we observed that $MAPbI_3$ perovskite can change its macroscopic electric properties by absorbing the energy of a single photon (about 0.2 aJoule), which cannot be elucidated without an internal amplification mechanism that can cause collective motion of a massive number of iodides by absorption of only a few photons.

The main contribution of this chapter is to report the first observation that by absorbing a few or even single photon, the macroscopic electric and optoelectronic properties of perovskite thin film can be altered or programmed. The detailed physical mechanism that gives the device its extremely high sensitivity and persistent response requires further experimental and theoretical investigations. One promising application utilizing this internal amplification process is analog memory device for neuromorphic computing [29-30]. The low-energy operation triggered by even single-photon irradiation provides large benefits in the computing system. Although there are several technological challenges including stability issues of this material group, novel cascadic ion migration behavior as well as the other high-speed operation regime gives us ample opportunities to create new device applications based on hybrid perovskites. We anticipate this part of work will create new avenues for research and application of perovskite device and material.

Portion of Chapter 5 has been published in the following publication: Xu, Z. †, Yu, Y. †, Arya, S., Niaz, I.A., Chen, Y., Lei, Y., Miah, M.A.R., Zhou, J., Zhang, A.C., Yan, L., Xu, S., and Lo, Y.H. 2020. Frequency-and Power-Dependent Photoresponse of a Perovskite Photodetector

Down to the Single-Photon Level. Nano Letters, 20(3), pp.2144-2151 († These authors contributed

equally). The dissertation author is the primary investigator/co-first author of the paper.

Reference

1. Kojima, A., Teshima, K., Shirai, Y. and Miyasaka, T., 2009. Organometal halide perovskites as visible-light sensitizers for photovoltaic cells. *Journal of the American Chemical Society*, *131*(17), pp.6050-6051.

2. Im, J.H., Lee, C.R., Lee, J.W., Park, S.W. and Park, N.G., 2011. 6.5% efficient perovskite quantum-dot-sensitized solar cell. *Nanoscale*, *3*(10), pp.4088-4093.

3. Lee, M.M., Teuscher, J., Miyasaka, T., Murakami, T.N. and Snaith, H.J., 2012. Efficient hybrid solar cells based on meso-superstructured organometal halide perovskites. *Science*, *338*(6107), pp.643-647.

4. Kim, H.S., Lee, C.R., Im, J.H., Lee, K.B., Moehl, T., Marchioro, A., Moon, S.J., Humphry-Baker, R., Yum, J.H., Moser, J.E. and Grätzel, M., 2012. Lead iodide perovskite sensitized all-solid-state submicron thin film mesoscopic solar cell with efficiency exceeding 9%. *Scientific reports*, *2*(1), pp.1-7.

5. Liu, M., Johnston, M.B. and Snaith, H.J., 2013. Efficient planar heterojunction perovskite solar cells by vapour deposition. *Nature*, *501*(7467), pp.395-398.

6. Burschka, J., Pellet, N., Moon, S.J., Humphry-Baker, R., Gao, P., Nazeeruddin, M.K. and Grätzel, M., 2013. Sequential deposition as a route to high-performance perovskite-sensitized solar cells. *Nature*, *499*(7458), pp.316-319.

7. Jeon, N.J., Noh, J.H., Yang, W.S., Kim, Y.C., Ryu, S., Seo, J. and Seok, S.I., 2015. Compositional engineering of perovskite materials for high-performance solar cells. *Nature*, *517*(7535), pp.476-480.

8. Yang, W.S., Park, B.W., Jung, E.H., Jeon, N.J., Kim, Y.C., Lee, D.U., Shin, S.S., Seo, J., Kim, E.K., Noh, J.H. and Seok, S.I., 2017. Iodide management in formamidinium-lead-halide–based perovskite layers for efficient solar cells. *Science*, *356*(6345), pp.1376-1379.

9. Lin, K., Xing, J., Quan, L.N., de Arquer, F.P.G., Gong, X., Lu, J., Xie, L., Zhao, W., Zhang, D., Yan, C. and Li, W., 2018. Perovskite light-emitting diodes with external quantum efficiency exceeding 20 per cent. *Nature*, *562*(7726), pp.245-248.

10. Feng, J., Gong, C., Gao, H., Wen, W., Gong, Y., Jiang, X., Zhang, B., Wu, Y., Wu, Y., Fu, H. and Jiang, L., 2018. Single-crystalline layered metal-halide perovskite nanowires for ultrasensitive photodetectors. *Nature Electronics*, *1*(7), pp.404-410.

11. Chou, Y.S., Chou, L.H., Guo, A.Z., Wang, X.F., Osaka, I., Wu, C.G. and Liu, C.L., 2019. Ultrasonic spray-coated mixed cation perovskite films and solar cells. *ACS Sustainable Chemistry & Engineering*, *7*(16), pp.14217-14224.

12. Burschka, J., Pellet, N., Moon, S.J., Humphry-Baker, R., Gao, P., Nazeeruddin, M.K. and Grätzel, M., 2013. Sequential deposition as a route to high-performance perovskite-sensitized solar cells. *Nature*, *499*(7458), pp.316-319.

13. Xiao, Z., Bi, C., Shao, Y., Dong, Q., Wang, Q., Yuan, Y., Wang, C., Gao, Y. and Huang, J., 2014. Efficient, high yield perovskite photovoltaic devices grown by interdiffusion of solution-processed precursor stacking layers. *Energy & Environmental Science*, *7*(8), pp.2619-2623.

14. Luo, P., Liu, Z., Xia, W., Yuan, C., Cheng, J. and Lu, Y., 2015. A simple in situ tubular chemical vapor deposition processing of large-scale efficient perovskite solar cells and the research on their novel roll-over phenomenon in J–V curves. *Journal of Materials Chemistry A*, *3*(23), pp.12443-12451.

15. Eames, C., Frost, J.M., Barnes, P.R., O'regan, B.C., Walsh, A. and Islam, M.S., 2015. Ionic transport in hybrid lead iodide perovskite solar cells. *Nature communications*, *6*(1), pp.1-8.

16. Ji, C., Wang, P., Wu, Z., Sun, Z., Li, L., Zhang, J., Hu, W., Hong, M. and Luo, J., 2018. Inch-Size Single Crystal of a Lead-Free Organic–Inorganic Hybrid Perovskite for High-Performance Photodetector. *Advanced Functional Materials*, *28*(14), p.1705467.

17. Guo, Y., Liu, C., Tanaka, H. and Nakamura, E., 2015. Air-stable and solution-processable perovskite photodetectors for solar-blind UV and visible light. *The journal of physical chemistry letters*, *6*(3), pp.535-539.

18. Dou, L., Yang, Y.M., You, J., Hong, Z., Chang, W.H., Li, G. and Yang, Y., 2014. Solution-processed hybrid perovskite photodetectors with high detectivity. *Nature communications*, *5*(1), pp.1-6.

19. Shen, L., Fang, Y., Wang, D., Bai, Y., Deng, Y., Wang, M., Lu, Y. and Huang, J., 2016. A Self-Powered, Sub-nanosecond-Response Solution-Processed Hybrid Perovskite Photodetector for Time-Resolved Photoluminescence-Lifetime Detection. *Advanced Materials*, *28*(48), pp.10794-10800.

20. Bao, C., Chen, Z., Fang, Y., Wei, H., Deng, Y., Xiao, X., Li, L. and Huang, J., 2017. Low-noise and large-linear-dynamic-range photodetectors based on hybrid-perovskite thin-single-crystals. *Advanced Materials*, *29*(39), p.1703209.

21. Wu, J., Chen, J., Zhang, Y., Xu, Z., Zhao, L., Liu, T., Luo, D., Yang, W., Chen, K., Hu, Q. and Ye, F., 2017. Pinhole-free hybrid perovskite film with arbitrarily-shaped micro-patterns for functional optoelectronic devices. *Nano letters*, *17*(6), pp.3563-3569.

22. Lian, Z., Yan, Q., Lv, Q., Wang, Y., Liu, L., Zhang, L., Pan, S., Li, Q., Wang, L. and Sun, J.L., 2015. High-performance planar-type photodetector on (100) facet of MAPbI 3 single crystal. *Scientific reports*, *5*, p.16563.

23. Chen, S., Teng, C., Zhang, M., Li, Y., Xie, D. and Shi, G., 2016. A flexible UV–Vis–NIR photodetector based on a perovskite/conjugated-polymer composite. *Advanced Materials*, *28*(28), pp.5969-5974.

24. Mosconi, E., Meggiolaro, D., Snaith, H.J., Stranks, S.D. and De Angelis, F., 2016. Light-induced annihilation of Frenkel defects in organo-lead halide perovskites. *Energy & Environmental Science*, *9*(10), pp.3180-3187.

25. Li, C., Tscheuschner, S., Paulus, F., Hopkinson, P.E., Kießling, J., Köhler, A., Vaynzof, Y. and Huettner, S., 2016. Iodine migration and its effect on hysteresis in perovskite solar cells. *Advanced Materials*, *28*(12), pp.2446-2454.

26. Pérez-Osorio, M.A., Milot, R.L., Filip, M.R., Patel, J.B., Herz, L.M., Johnston, M.B. and Giustino, F., 2015. Vibrational properties of the organic–inorganic halide perovskite CH3NH3PbI3 from theory and experiment: factor group analysis, first-principles calculations, and low-temperature infrared spectra. *The Journal of Physical Chemistry C*, *119*(46), pp.25703-25718.

27. Jeangros, Q., Duchamp, M., Werner, J., Kruth, M., Dunin-Borkowski, R.E., Niesen, B., Ballif, C. and Hessler-Wyser, A., 2016. In situ TEM analysis of organic–inorganic metal-halide perovskite solar cells under electrical bias. *Nano letters*, *16*(11), pp.7013-7018.

28. Price, M.B., Butkus, J., Jellicoe, T.C., Sadhanala, A., Briane, A., Halpert, J.E., Broch, K., Hodgkiss, J.M., Friend, R.H. and Deschler, F., 2015. Hot-carrier cooling and photoinduced refractive index changes in organic–inorganic lead halide perovskites. *Nature communications*, *6*(1), pp.1-8.

29. Zou, C., Zheng, J., Chang, C., Majumdar, A. and Lin, L.Y., 2019. Nonvolatile Rewritable Photomemory Arrays Based on Reversible Phase-Change Perovskite for Optical Information Storage. *Advanced Optical Materials*, *7*(18), p.1900558.

30. Wang, Y., Lv, Z., Chen, J., Wang, Z., Zhou, Y., Zhou, L., Chen, X. and Han, S.T., 2018. Photonic synapses based on inorganic perovskite quantum dots for neuromorphic computing. *Advanced materials*, *30*(38), p.1802883.

Chapter 6. Conclusion and Outlook

6.1 Conclusion

This dissertation presented two novel internal signal amplification mechanisms of light detection.

Cycling excitation process (CEP), a novel carrier multiplication mechanism, has high carrier multiplication efficiency due to the presence of high density of localized states and strong electron-phonon interactions. It was firstly discovered in a heavily-doped compensated silicon p/n junction photodiode, which showed signal amplification with unprecedented efficiency and noise characteristics operated at low reverse bias voltages. Based on these two physical insights of localized states and phonon absorption, CEP effect can also be achieved in disordered materials such as amorphous silicon (a-Si), which intrinsically has high density of localized states due to the disordered structure.

With this thought in mind, a carbon-doped, hydrogenated amorphous silicon photodiode was demonstrated with some desirable properties such as a record high gain-bandwidth product and an excellent excess noise performance. The device structure is simple, with only a thin layer of a-Si (35 nm) sandwiched by n-$^+$ Si substrate and top ITO electrode. To better understand the device physics and improve device behavior, we conducted temperature dependent dark current measurement to discuss the dark current mechanism of the carbon-doped a-Si device. It was shown that the primary source of dark current for the a-Si CEP detectors is the indirect tunneling followed by Poole-Frenkel emission. A structure based on band gap engineering was designed by inserting an intermediate layer of material of proper band gap and electron affinity to raise the effective tunneling barrier. The chosen material is cupric oxide (Cu_2O) with band gap of 2.1 eV and electron affinity of -3.2 eV. By characterizing the dark current and photo response of a-Si and a-Si/Cu_2O

devices, we found that by inserting a thin layer of Cu_2O (40 nm), the dark current is significantly suppressed by over one order of magnitude while the photo response remains similar.

Based on the high performance of carbon-doped a-Si CEP device, we proposed a structure with a thin layer of a-Si deposited on non-semiconductor substrate. Due to its low absorption efficiency, gold nanoparticles (Au NPs) were incorporated in a-Si layer to enhance the absorption efficiency by utilizing localized surface plasmon resonance (LSPR) effect. With the help of Au NP, the dark current was suppressed while the photo responsivity was enhanced. Moreover, the device frequency response is improved with a higher bandwidth over 1 GHz. The photo responsivity enhancement was supported by the 3D electromagnetic (EM) field simulation by COMSOL. The EM field was greatly enhanced near the surface of Au NP, leading to the increasing in light absorption. The device speed increasing can be elucidated by the DC electric field simulation, which was also increased near the particle surface. The good match between EM field and DC field areas contributes to the shorter transit time of photogenerated carriers and thus better speed response.

Besides solid-state semiconductor detectors such as silicon and amorphous silicon, we also demonstrated photodetection in spin-coated organometallic perovskite detector. The detailed study on the power and frequency dependent photo response in perovskite photodetector tells us interesting information: there are two types of light detection mechanisms, with the first one to be the conventional light detection by absorbing photons and generating electron-hole pairs, which has high frequency response but no gain, and the second one to be a quasi-persistent photo response, which has single photon detection ability. From the results of careful characterization of the power dependent responsivity, single photon statistics and reflective spectrum of device, we proposed an internal signal amplification mechanism, ionic impact ionization, involving a cascade process of

ion migrations and accumulations triggered by a few or even single photon. The accumulated ions and vacancies contribute to the conductivity change of the device, hence change the current level which we considered as "photocurrent".

6.2 Outlook

For the carbon-doped a-Si CEP detectors, we have already successfully demonstrated the characteristics under visible light range. It is desired to extend the working wavelength of CEP photodetectors to infrared range. In order to have infrared photo response, a proper absorption layer is required. There are several candidates which can be incorporated with a-Si CEP device. The first one is amorphous germanium (a-Ge). Even thought its band gap is slightly large (~0.97 eV), the presence of abundant impurity states can improve the infrared absorption. Besides, graphene is a perfect material with 2% absorption at all wavelengths. Graphene based a-Si CEP detector was briefly introduced in section 2.8, and further works such as broadband photo response and high-speed performance can be done.

Apart from the CEP devices, there are a lot of topics that can be studied on perovskite detectors. First, to support the ionic impact ionization mechanism that we proposed, many theoretical simulations and calculations such as DFT calculation are required. Also, more experiments on investigating ionic impact ionization in other type of organometallic perovskites as well as grain boundaries influences need to be further conducted. Moreover, as we know a single photon carrying 0.2 aJoule can trigger the I3 process, the single electron injection induced ionic impact ionization is worth trying in the future.